9-2004

Quantifying Initial Condition and Parametric Uncertainties in a Nonlinear Aeroelastic System with an Efficient Stochastic Algorithm

Daniel R. Millman

QUANTIFYING INITIAL CONDITION AND PARAMETRIC UNCERTAINTIES IN A NONLINEAR AEROELASTIC SYSTEM WITH AN EFFICIENT STOCHASTIC ALGORITHM

DISSERTATION

Daniel Raul Millman
Major, USAF

AFIT/DS/ENY/04-03

DEPARTMENT OF THE AIR FORCE
AIR UNIVERSITY

AIR FORCE INSTITUTE OF TECHNOLOGY

Wright-Patterson Air Force Base, Ohio

The views expressed in this dissertation are those of the author and do not reflect the official policy or position of the United States Air Force, Department of Defense, or the United States Government.

AFIT/DS/ENY/04-03

QUANTIFYING INITIAL CONDITION AND PARAMETRIC UNCERTAINTIES IN A NONLINEAR AEROELASTIC SYSTEM WITH AN EFFICIENT STOCHASTIC ALGORITHM

DISSERTATION

Presented to the Faculty

Graduate School of Engineering and Management

Air Force Institute of Technology

Air University

Air Education and Training Command

in Partial Fulfillment of the Requirements for the

Degree of Doctor of Philosophy

Daniel Raul Millman, B.S.M.E., M.S.

Major, USAF

September 2004

AFIT/DS/ENY/04-03

QUANTIFYING INITIAL CONDITION AND PARAMETRIC UNCERTAINTIES IN A NONLINEAR AEROELASTIC SYSTEM WITH AN EFFICIENT STOCHASTIC ALGORITHM

Daniel Raul Millman, B.S.M.E., M.S.

Major, USAF

Approved:

Paul I. King Dissertation Advisor	Date
Philip S. Beran Committee Member	Date
Lawrence K. Chilton Committee Member	Date
Lt Col Raymond C. Maple Committee Member	Date
Yung Kee Yeo Dean's Representaive	Date

Robert A. Calico, Jr
Dean

Acknowledgments

Only one name appears as author, but the aid, insights, and encouragement of many made this work possible. Foremost among those, and to whom I owe a great debt of gratitude, is my dissertation advisor, Dr. Paul King. I would also like to thank Lt Col Ray Maple for constantly challenging my ideas and Dr. Larry Chilton for reminding me that the analysis actually comes before the numerical. Of course, many thanks also goes to my research advisor and sponsor, Dr. Phil Beran, who always kept me focused on the research effort whenever I would get lost in the weeds. Thanks to Dr. Chris Pettit for sitting down with me and explaining the theory of polynomial chaos expansions, and Dr. Bill Baker for the many insightful mathematical discussions. I would also like to thank Dr. Don Thompson. Without his support I would not have had the opportunity to pursue this degree.

The many hours sitting at my desk and running simulations were made bearable by my fellow PhD students that sat in the Behind AFIT Relocatable Facility with me. Their leadership, humor, and camaraderie added color to an otherwise mundane workday. There are too many names to list, so I'll just have to thank them all.

Finally, I want to thank my wife for taking care of me these last three years. Her love, devotion, and encouragement were a constant source of strength for me. Our daughters also kept reminding me what is truly important in life, and it is to them and to my wife that I dedicate this work.

Table of Contents

List of Figures

List of Tables

Nomenclature

Symbol	*Description*
a_h	nondimensional distance from the airfoil mid-chord to the elastic axis
A_x, A_y	area vectors normal to the finite volume cell faces
b	airfoil mid-chord
$B_{i,k_{\xi_1},\boldsymbol{x}_{\xi_1}}$	the i-th B-spline of order k_{ξ_1} for the knot sequence $\boldsymbol{x}_{\xi_1}$
$B_{j,k_{\xi_2},\boldsymbol{x}_{\xi_2}}$	the j-th B-spline of order k_{ξ_2} for the knot sequence $\boldsymbol{x}_{\xi_2}$
c	airfoil chord
C_l	lift coefficient
C_m	moment coefficient about the elastic axis
C_p	coefficient of pressure
d	dimension of $\boldsymbol{\xi}$
D_h	plunge viscous damping constant
D_α	pitch viscous damping constant
E_t	total energy
$\mathbf{E}$, $\mathbf{F}$	flux vectors
h	dimensional plunging displacement
I, J	defines the nodes on the ξ_1 and ξ_2 axes, respectively
I_α	second moment of inertia
k_{ξ_1}, k_{ξ_2}	order of the B-splines on the ξ_1 and ξ_2 axes, respectively
K_h	plunge spring constant
K_α	pitch spring constant
L	lift
m	airfoil mass
M_{ea}	moment about the elastic axis
n_x, n_y	unit vectors normal to the finite volume cell faces
N	number of realizations in a Monte Carlo simulation

p	pressure
P	upper limit of a chaos expansion
$\mathbf{Q}$	vector of conserved variables
r_α	nondimensional radius of gyration about the elastic axis
$\boldsymbol{\mathcal{R}}$	residual
S_α	first moment of inertia
t	time
u	x-component of velocity
U	contravarient velocity
v	y-component of velocity
V	velocity, contravariant velocity
V_r	reduced velocity
$w(\boldsymbol{\xi})$	Gaussian distribution
x	horizontal coordinate of the grid
x_{cg}	nondimensional distance from the airfoil leading edge to the center of gravity of the airfoil
x_α	nondimensional distance from the elastic axis to the center of mass of the airfoil
$\boldsymbol{x}_{\xi_1}$, $\boldsymbol{x}_{\xi_2}$	vectors containing the knots on the ξ_1 and ξ_2 axes, respectively
y	nondimensional plunge displacement of the elastic axis, vertical coordinate of the grid

α	pitch angle
β_α	cubic pitch spring constant
γ_α	quintic pitch spring constant
μ_s	airfoil/air mass ratio
ζ_y	plunge damping coefficient
ζ_α	pitch damping coefficient

$\varepsilon_1, \varepsilon_2$	constants in the Wagner function
μ	mean
ξ_t, η_t	temporal metrics of transformation
ξ_x, ξ_y, η_x, η_y	spatial metrics of transformation
$\boldsymbol{\xi}$	vector containing the zero mean, unit variance Gaussian random variables $(\xi_1, \xi_2, \ldots, \xi_d)$
ρ	density
σ	standard deviation
τ	nondimensional time
ϕ	Wagner function
ψ_1, ψ_2	constants in the Wagner function
Ψ_i	the i-th chaos basis function
ω_y	plunge natural frequency
ω_α	pitch natural frequency
ω_r	frequency ratio
ζ_h, ζ_α	coefficients of viscous damping for plunge and pitch, respectively

Superscripts

$\bar{}$	mean values
$\tilde{}$	standard deviation values
$\hat{}$	coefficients of the chaos expansions

Subscripts

∞	free stream values

Abbreviations

Abbreviation	*Definition*
CFD	computational fluid dynamics
FCE	Fourier chaos expansion
LCO	limit cycle oscillation
MCS	Monte Carlo simulation
PCE	polynomial chaos expansion
PDF	probability density function
ROM	reduced-order modeling
RSM	response surface methodologies

Abstract

Computational fluid dynamics (CFD) methods have been coupled with structural solvers to provide accurate predictions of limit cycle oscillations (LCO). There is, however, a growing interest in understanding how uncertainties in flight conditions and structural parameters affect the character of an LCO response, leading to failure of an aeroelastic system. Uncertainty quantification of a stochastic system (parametric uncertainty) with stochastic inputs (initial condition uncertainty) has traditionally been analyzed with Monte Carlo simulations (MCS). Probability density functions (PDF) of the LCO response are obtained from the MCS to estimate the probability of failure. A CFD solution, however, can take days to weeks to obtain a single response, making the MCS method intractable for large problems. A candidate approach to efficiently estimate the PDF of an LCO response is the stochastic projection method. The classical stochastic projection method is a polynomial chaos expansion (PCE). The PCE approximates the response in the stochastic domain through a Fourier type expansion of the Wiener-Hermite polynomials. An LCO response can be characterized as a subcritical or supercritical bifurcation, and bifurcations are shown to be discontinuities in the stochastic domain. The PCE method, then, would be too inefficient for estimating the LCO response surface. The objective of this research is to extend the stochastic projection method to include the construction of B-spline surfaces in the stochastic domain. The multivariate B-spline problem is solved to estimate the LCO response surface. An MCS is performed on this response surface to estimate the PDF of the LCO response. The probability of failure is then computed from the PDF. The stochastic projection method via B-splines is applied to the problem of estimating the PDF of a subcritical LCO response of a nonlinear airfoil in inviscid transonic flow. The stochastic algorithm provides a conservative estimate of the probability of failure of this aeroelastic system two orders of magnitude more efficiently than performing an MCS on the governing equations.

QUANTIFYING INITIAL CONDITION AND PARAMETRIC UNCERTAINTIES IN A NONLINEAR AEROELASTIC SYSTEM WITH AN EFFICIENT STOCHASTIC ALGORITHM

I. Introduction

Fluid-structure interaction can result in the loss of dynamic stability to a time periodic instability that grows unbounded, i.e., flutter [1]. When nonlinear aerodynamics (e.g., transient shocks or boundary layer separation) or nonlinear structural parameters are present to counter the growth of the unstable mode, the dynamic response may stabilize to a limit cycle oscillation (LCO) [2]. The study of LCO in aeroelastic systems is an active area of research [3, 4, 5, 6]. Flight data from fighter aircraft with external stores indicate that the LCO response is characterized by antisymmetric motion of the wing and a lateral motion of the fuselage and, consequently, the aircrew. LCO can lead to fatigue failure of the wing structure. The lateral motion LCO induces can degrade mission effectiveness by not allowing the aircrew to track a target or lead the aircrew to believe that the aircraft has begun to flutter, causing a mission abort. In severe cases, LCO represents a hazard to flight safety [2].

Computational fluid dynamics (CFD) methods have been coupled with structural solvers to provide accurate predictions of LCOs [7]. There is, however, a growing interest in understanding how uncertainties in flight conditions and structural parameters affect the character of an LCO response, leading to failure of an aeroelastic system [8]. Uncertainty quantification of a stochastic system (parametric uncertainty) with stochastic inputs (initial condition uncertainty) has traditionally been analyzed with Monte Carlo simulations (MCS) [9]. In an MCS, N random realizations of the uncertainty parameters are input into the system of equations to obtain N realizations of the response. The

probability density function (PDF) of the response is then approximated from the N realizations. The MCS method only requires that the distribution of the input parameters be known. A CFD solution, however, can take days to weeks to obtain a single response, making the MCS method intractable for large problems.

Other techniques that have been used to solve stochastic systems with stochastic inputs are based upon Galerkin's method [9]. These include reduced order modeling (ROM) [10, 11, 12] and polynomial chaos expansions (PCE) [13, 14, 15, 9, 16, 17, 18, 19, 20, 21]. The reduced order model represents a full order solution with an optimal basis, in the mean square sense, through a Karhunen-Loeve expansion. Monte Carlo simulations can efficiently be run on the ROM, but only for small variations in the inputs. Thus, ROM is useful for examining responses near the mean value but cannot predict responses with large variations in the input [10]. The PCE method, on the other hand, allows large variations in the input parameters and has been shown, for certain classes of problems, to be far more efficient than an MCS [15]. The classical PCE method, also known as the Wiener-Hermite expansion [22], falls into a general category of stochastic projection methods. Of the two methods, ROM or stochastic projection, the stochastic projection method was chosen, due to its greater efficiency and robustness in handling large variations, to quantify the effects of uncertainty and estimate the probability of failure for a nonlinear aeroelastic system.

1.1 Overview of Stochastic Projection Methods

Stochastic projection methods, unlike the Karhunen-Loeve expansions employed by ROM, provide a way to estimate the expansion of a response without a priori knowledge of the form of the response in the stochastic domain. A random basis, denoted $\Psi_i(\boldsymbol{\xi})$, orthogonal with respect to the distribution of the input uncertainty, is typically selected. The deterministic coefficients of the expansion, $\hat{\alpha}_i(t)$, are either computed as part of the time integration (intrusive approach) or estimated from a limited MCS (non-intrusive

approach). The expansion of some response $\alpha(t, \boldsymbol{\xi})$ then takes the form [14, 15]

$$\alpha(t, \boldsymbol{\xi}) = \sum_{i=0}^{P} \hat{\alpha}_i(t) \Psi_i(\boldsymbol{\xi}) \tag{1.1}$$

where the upper limit P is based on the order of the expansion and the number of input uncertainties, i.e. the dimension, d, of $\boldsymbol{\xi}$. The vector $\boldsymbol{\xi}$ contains the random variables that characterize the uncertainty distribution of the input parameters. For a Gaussian distribution, the uncertainty of some input parameter, β_α, is characterized by its mean value, $\bar{\beta}_\alpha$, and its standard deviation, $\tilde{\beta}_\alpha$, as

$$\beta_\alpha = \bar{\beta}_\alpha + \xi_1 \tilde{\beta}_\alpha \tag{1.2}$$

where ξ_1 is a zero mean, unit variance Gaussian random variable.

With the intrusive approach, the expansion in Eq. (1.1) is substituted directly into the governing equations of motion. For example, if an equation of motion took the form

$$\mathcal{L}[\alpha(t)] + \beta_\alpha \alpha^3 = 0 \tag{1.3}$$

where $\mathcal{L}$ is a linear differential operator, then the stochastic projection method would, with a Galerkin approach (see, for example, Le Maître et al. [18]), produce the following system of equations to be solved

$$\mathcal{L}[\hat{\alpha}_n(t)] + \bar{\beta}_\alpha \sum_{i=0}^{P}\sum_{j=0}^{P}\sum_{k=0}^{P} \hat{\alpha}_i \hat{\alpha}_j \hat{\alpha}_k \frac{\langle \Psi_i \Psi_j \Psi_k, \Psi_n \rangle}{\langle \Psi_n, \Psi_n \rangle} + \tilde{\beta}_\alpha \sum_{i=0}^{P}\sum_{j=0}^{P}\sum_{k=0}^{P} \hat{\alpha}_i \hat{\alpha}_j \hat{\alpha}_k \frac{\langle \xi_1 \Psi_i \Psi_j \Psi_k, \Psi_n \rangle}{\langle \Psi_n, \Psi_n \rangle} = 0 \tag{1.4}$$

where the free index, n, is in the range $0 \leq n \leq P$. The expected value operator, $\langle\ \rangle$, is defined as

$$\langle f(\boldsymbol{\xi}), \Psi_n(\boldsymbol{\xi}) \rangle = \int_{-\infty}^{\infty} \int_{-\infty}^{\infty} \cdots \int_{-\infty}^{\infty} f(\boldsymbol{\xi}) \Psi_n(\boldsymbol{\xi}) w(\boldsymbol{\xi})\, \mathrm{d}\xi_1\, \mathrm{d}\xi_2 \cdots \mathrm{d}\xi_d \tag{1.5}$$

where $f(\boldsymbol{\xi})$ is any function of $\boldsymbol{\xi}$ and $w(\boldsymbol{\xi})$ is the Guassian PDF

$$w(\boldsymbol{\xi}) = \left(\frac{1}{\sqrt{2\pi}}\right)^d e^{-\frac{1}{2}\boldsymbol{\xi}^T\boldsymbol{\xi}} \,. \tag{1.6}$$

The condition of orthogonality with respect to the Guassian PDF substantially reduces the number of non-zero expected values for a linear problem. As nonlinearity increases, the number of non-zero terms grows rapidly due to the coupling evident in Eq. (1.4). Computational efficiency is rapidly lost when high order expansions of highly nonlinear equations are required [22, 23, 24, 25, 26].

To gain back some computational efficiency, researchers have employed the non-intrusive approach. This is a sampling approach and considered non-intrusive since parametric uncertainty is not included analytically in the equations of motion. A limited MCS is performed and the responses obtained are used to estimate the coefficients of the expansion. Due to the random selection of samples, the expected value operator is again employed. The coefficients are estimated from [8]

$$\hat{\alpha}_i = \frac{\langle \alpha, \Psi_i \rangle}{\langle \Psi_n, \Psi_n \rangle} \,. \tag{1.7}$$

This non-intrusive approach substantially reduces the number of expected values that need to be pre-computed and stored and is considered more appropriate for highly non-linear problems.

Thus far the discussion has centered around the mathematics of the stochastic projection method. The stochastic projection also has a physical interpretation, i.e. it can be viewed as approximating the response surface across the entire stochastic domain [9, 15, 25]. The stochastic projection method, though, differs from traditional response surface methodologies (RSM) [27] in that the expansion is global whereas RSM is concerned with local expansions about some point of interest. Thus, the stochastic projection method is an interpolation algorithm. This viewpoint explains many of the issues that, in particular, caused the PCE approach to be mostly abandoned by the 1970's [15]. The

original PCE method assumed a Gaussian uncertainty in the parameters and the orthogonal basis functions chosen for the expansion were the Hermite polynomials [13, 14, 15]. Chorin [22] discussed the lack of sufficient frequency content in the Hermite polynomials to approximate discontinuities to stochastic solutions of the inviscid Burger's equation. Crow and Canavan [23] demonstrated that, while only low order Hermite expansions are computationally practical, high order Hermite polynomials are required to allow an energy cascade for approximating a turbulent flow.

Despite these findings, recent literature on the generalized PCE through an Askey scheme [19], which matches distribution functions to the appropriate orthogonal polynomials, still cites the optimality of polynomial expansions without regard to the issue of frequency content. Millman et al. [24, 25], however, showed that by changing to a Fourier basis, termed a Fourier chaos expansion (FCE), stochastic projections with discontinuities could be better approximated. A comparison of the stochastic projections from the PCE and FCE approaches is shown in Figure 1.1, where for this example the random variable ξ_2 represents the uncertainty in the initial pitch angle of a nonlinear airfoil in the presence of modeled aerodynamics [25]. The ability of the FCE to better approximate the discontinuity than the PCE method leads to a better approximation of the PDF of the LCO response, as shown in Figure 1.2. These results were based on the intrusive method and, while a substantial improvement over the PCE method, the FCE method was still too computationally inefficient to be useful in a design environment due to multiple summations such as the ones in Eq. (1.4).

Numerical techniques have been advanced to overcome the computational expense of computing the multiple summations. For example, Mathelin and Hussaini [28] employ a stochastic collocation scheme in the solution of the Reimann problem that reduces the computational effort from order P^3, $\mathcal{O}(P^3)$, to $\mathcal{O}(P)$. However, they note that the upper limit P has to be large ($P = 200$) to accurately account for the moving discontinuity [28].

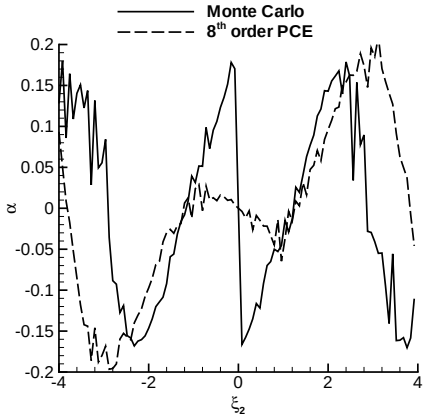

(a) **MCS vs. 8^{th} order PCE**

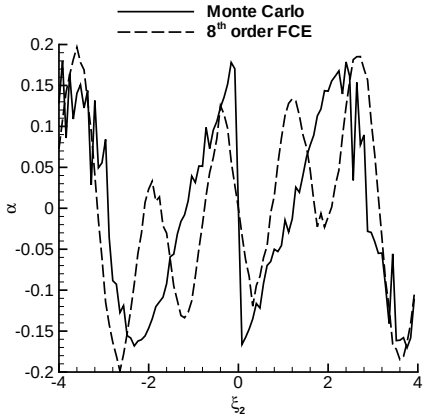

(b) **MCS vs. 8^{th} order FCE**

Figure 1.1 $\alpha(t, \boldsymbol{\xi})$ at $t = 2000$ vs. ξ_2 [25]

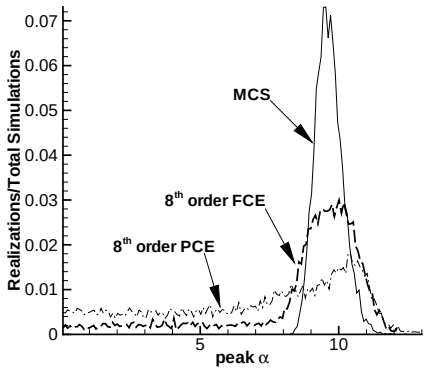

Figure 1.2 PDFs of a supercritical response, MCS vs. 8^{th} order PCE and FCE [25]

It will be shown that bifurcations, such as the LCO response of an airfoil, are discontinuities in the stochastic domain. Thus, the numerical issues faced by Chorin [22], Crow and Canavan [23], and Mathelin and Hussaini [28] must be dealt with in an efficient manner. In interpolation theory, discontinuities are treated as piecewise polynomials and researchers commonly employ B-splines to approximate these piecewise polynomials [29]. Constructing B-spline surfaces is also a collocation approach since the nodes of the surface are fitted exactly [30]. The nodes of the response (B-spline) surface can be computed

from a nonintrusive approach and, since the B-spline method is non-Galerkin, expected values need not be computed or stored [31].

1.2 Scope of Research

The objective of this research is to extend the stochastic projection method to include the construction of B-spline surfaces in the stochastic domain. These surfaces should adequately resolve discontinuities that arise from the bifurcations (LCO response) of a nonlinear airfoil in an inviscid transonic flow. An efficient MCS over the response surface will allow a rapid estimation of the PDF of an LCO response. The probability of failure can then be computed from the PDF. The scope of this research is defined by the following thesis statement, approach, and assumptions:

1.2.1 Thesis Statement. *The probability density function of a limit cycle oscillation response, and hence the probability of failure, can be accurately and efficiently estimated with a small sample size obtained from the solution of the nonlinear time dependent aeroelastic system of equations.*

1.2.2 Research Approach and Assumptions. The implementation and effectiveness of the stochastic projection method via B-splines will be demonstrated for the CFD application of a two-dimensional pitching and plunging airfoil in inviscid, transonic compressible flow. The structural components will be nonlinear in pitch. Since an MCS is impractical for the CFD application, the stochastic projection method via B-splines will first be validated against MCS results of a model problem: a structurally nonlinear airfoil in a linearly modeled, low speed incompressible flow. Convergence of the PDFs for the CFD application will then be presented.

The uncertainty distributions in this research effort are limited to Gaussian distributions, as given in Eq. (1.6). The choice of Gaussian distributions was made early in the research phase to allow a direct comparison with the classical PCE formulation. As will be shown, the choice in distributions is not critical to the development of this stochastic

algorithm. The number of uncertainties was limited to one initial condition uncertainty and one parametric uncertainty.

1.3 Document Organization

The remainder of this document is organized as follows:

Chapter II: Demonstrates estimating the probability of failure of a nonlinear airfoil in flow modeled with linear aerodynamics through a traditional Monte Carlo analysis.

Chapter III: Develops the theory of the stochastic projection method via B-splines. The stochastic algorithm is implemented on the nonlinear airfoil with linear aerodynamics to estimate the probability of failure.

Chapter IV: Describes the development of an inviscid aeroelastic code (EULER-AE) that computes the flow properties over a pitching and plunging airfoil with the Euler equations.

Chapter V: Implements the stochastic algorithm on the nonlinear airfoil in inviscid transonic compressible flow to estimate the probability of failure.

Chapter VI: Summarizes the results and conclusions of the current research. Discusses topics of future research suggested by the currrent research.

II. Nonlinear Pitch and Plunge Airfoil with Linear Aerodynamics

2.1 Introduction

Before choosing an expansion to represent a response in the stochastic domain, it is useful to examine the behavior of a set of nonlinear equations with parametric and initial condition uncertainties. An appropriate model problem to begin this analysis should be easily integrated in time such that an MCS is practical. To this end, a nonlinear pitch and plunge airfoil with linear aerodynamics is chosen. A stability analysis of this model problem was accomplished by Lee et al [3]. The goal of this chapter is not to replicate the stability analysis of a system of ordinary differential equations with the methods one finds in, for example, Seydel [32], but rather, to perform a numerical analysis of the behavior of the bifurcations of a system in the presence of uncertainties. Results from Lee et al. [3] and Beran and Pettit [8] are a basis for the validity of the numerical analysis performed here.

The equations of motion for a nonlinear pitch and plunge airfoil are first derived. The aerodynamics needed to compute the lift and moment coefficients are obtained from Fung's model [1] for incompressible flow based on the circulation theory of lift. A set of ordinary differential equations are then derived, following Lee et al [3]. PDFs of the LCO response in pitch, α_{LCO}, are developed from an MCS based on parametric and initial condition uncertainty. These PDFs are also used to generate the probability of failure based on encountering an LCO response. This analysis will serve as basis for the development in the next chapter of a stochastic algorithm that will approximate the PDFs obtained here without performing an MCS on the governing equations.

2.2 Equations of Motion

Various formulations for the pitching and plunging airfoil have been developed [1, 3, 33, 34]. The notation shown in Figure 2.1 is used for the derivation of the equations of motion for this model problem [1, 3]. The plunge, h, is measured positive in the

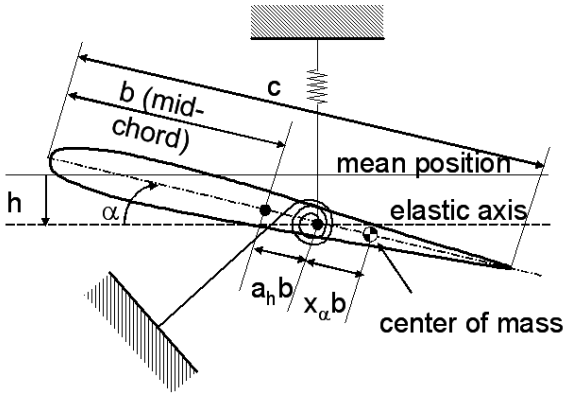

Figure 2.1 Schematic of a pitch and plunge airfoil

downward direction. The elastic axis (or hinge point) is located the distance $a_h b$ from the midchord, b, and is measured positive aft. The pitch angle, α, is positive nose up about the elastic axis. The center of mass is located the distance $x_\alpha b$ from the elastic axis, also measured positive aft. Summing the forces and moments, and assuming small pitch angles, results in

$$m\ddot{h} + S_\alpha \ddot{\alpha} + K_h h = -L \tag{2.1a}$$

$$S_\alpha \ddot{h} + I_\alpha \ddot{\alpha} + K_\alpha(\alpha + \beta_\alpha \alpha^3 + \gamma_\alpha \alpha^5) = M_{ea} \tag{2.1b}$$

where L is the lift, M_{ea} is the moment about the elastic axis, S_α is the first moment of inertia, I_α is the second moment of inertia, K_h is the plunge spring constant, and K_α is the pitch spring constant. The constants β_α and γ_α control the amount of structural nonlinearity. Note that [1]

$$S_\alpha = m x_\alpha b \tag{2.2a}$$

$$I_\alpha = m r_\alpha^2 b^2 \tag{2.2b}$$

$$K_h = m\omega_h^2 \tag{2.2c}$$

$$K_\alpha = I_\alpha \omega_\alpha^2 \tag{2.2d}$$

where m is the mass of the airfoil, $r_\alpha b$ is the radius of gyration, and ω_h and ω_α are the uncoupled natural frequencies of plunge and pitch, respectively. Also

$$L = \frac{1}{2}\rho_\infty V_\infty^2 c\, C_l \tag{2.3a}$$

$$M_{ea} = \frac{1}{2}\rho_\infty V_\infty^2 c^2 C_m \tag{2.3b}$$

where c is the chord length, ρ_∞ is the freestream density, V_∞ is the freestream velocity, and C_l and C_m are the lift and moment coefficients, respectively. By defining the following nondimensional parameters

$$y = \frac{h}{b} \tag{2.4a}$$

$$\omega_r = \frac{\omega_h}{\omega_\alpha} \tag{2.4b}$$

$$V_r = \frac{V_\infty}{\omega_\alpha b} \tag{2.4c}$$

$$\mu_s = \frac{m}{\rho_\infty b^2 \pi}. \tag{2.4d}$$

where y is the nondimensional plunge, ω_r is the frequency ratio, V_r is the reduced velocity, and μ_s is the mass ratio, and differentiating with respect to the nondimensional time

$$\tau = \frac{t\, V_\infty}{b}\,, \tag{2.5}$$

Eqs. (2.1a) and (2.1b) can be rewritten as

$$\ddot{y} + x_\alpha \ddot{\alpha} + \left(\frac{\omega_r}{V_r}\right)^2 y = -\frac{1}{\pi\mu_s} C_l \tag{2.6a}$$

$$\frac{x_\alpha}{r_\alpha^2}\ddot{y} + \ddot{\alpha} + \frac{1}{V_r^2}(\alpha + \beta_\alpha \alpha^3 + \gamma_\alpha \alpha^5) = \frac{2}{\pi\mu_s r_\alpha^2} C_m\,. \tag{2.6b}$$

Both the lift and moment coefficients are a function of time. Lee et al. [3] provide expressions for incompressible flow over a pitching and plunging airfoil based on a model

given by Fung [1]

$$\begin{aligned} C_l(\tau) &= \pi\left(\ddot{y} - a_h\ddot{\alpha} + \dot{\alpha}\right) + 2\pi\left[\alpha(0) + \dot{y}(0) + \left(\frac{1}{2} - a_h\right)\dot{\alpha}(0)\right]\phi(\tau) \\ &\quad + 2\pi\int_0^\tau \phi(\tau-\sigma)\left[\dot{\alpha}(\sigma) + \ddot{y}(\sigma) + \left(\frac{1}{2} - a_h\right)\ddot{\alpha}(\sigma)\right]\,\mathrm{d}\sigma \end{aligned} \tag{2.7a}$$

$$\begin{aligned} C_m(\tau) &= \pi\left(\frac{1}{2} + a_h\right)\left[\alpha(0) + \dot{y}(0) + \left(\frac{1}{2} - a_h\right)\dot{\alpha}(0)\right]\phi(\tau) \\ &\quad + \pi\left(\frac{1}{2} + a_h\right)\int_0^\tau \phi(\tau-\sigma)\left[\dot{\alpha}(\sigma) + \ddot{y}(\sigma) + \left(\frac{1}{2} - a_h\right)\ddot{\alpha}(\sigma)\right]\,\mathrm{d}\sigma \\ &\quad + \frac{1}{2}\pi\, a_h\left(\ddot{y} - a_h\ddot{\alpha}\right) - \frac{1}{2}\pi\left(\frac{1}{2} - a_h\right)\dot{\alpha} - \frac{1}{16}\pi\,\ddot{\alpha} \end{aligned} \tag{2.7b}$$

where the Wagner function, $\phi(\tau)$, is given by [1]

$$\phi(\tau) = 1 - \psi_1\, e^{-\varepsilon_1\tau} - \psi_2\, e^{-\varepsilon_2\tau}. \tag{2.8}$$

Fung [1] provides several values for the constants in the Wagner function. The values of $\psi_1 = 0.165$, $\psi_2 = 0.335$, $\varepsilon_1 = 0.0455$, and $\varepsilon_2 = 0.3$ are obtained from Jones [35].

2.3 Numerical Integration

Equations (2.6a), (2.6b), (2.7a) and (2.7b) represent a complete description of a pitching and plunging airfoil with incompressible aerodynamics. Since stability analysis techniques require a system of ordinary differential equations, Lee et al. [3] introduced four new variables

$$w_1(\tau) = \int_0^\tau e^{-\varepsilon_1(\tau-\sigma)}\alpha(\sigma)\,\mathrm{d}\sigma \tag{2.9a}$$

$$w_2(\tau) = \int_0^\tau e^{-\varepsilon_2(\tau-\sigma)}\alpha(\sigma)\,\mathrm{d}\sigma \tag{2.9b}$$

$$w_3(\tau) = \int_0^\tau e^{-\varepsilon_1(\tau-\sigma)}h(\sigma)\,\mathrm{d}\sigma \tag{2.9c}$$

$$w_4(\tau) \;=\; \int_0^\tau e^{-\varepsilon_2(\tau-\sigma)} h(\sigma)\, \mathrm{d}\sigma. \tag{2.9d}$$

These variables allow Eqs. (2.6a) and (2.6b) to be rewritten as

$$c_0\ddot{y} + c_1\ddot{\alpha} + c_2\dot{y} + c_3\dot{\alpha} + c_4 y + c_5\alpha + c_6 w_1 + c_7 w_2 + c_8 w_3 + c_9 w_4 = f(\tau) \tag{2.10a}$$

$$\begin{aligned} d_0\ddot{y} + d_1\ddot{\alpha} + d_2\dot{\alpha} + d_3\dot{y} + d_4\alpha + d_5\alpha^3 + d_6\alpha^5 + d_7 y \\ + d_8 w_1 + d_9 w_2 + d_{10} w_3 + d_{11} w_4 = g(\tau) \end{aligned} \tag{2.10b}$$

where the constants in Eq. (2.10a) are given by

$$c_0 = 1 + \frac{1}{\mu_s} \qquad c_1 = x_\alpha - \frac{a_h}{\mu_s}$$

$$c_2 = \frac{2}{\mu_s}(1 - \psi_1 - \psi_2) \qquad c_3 = \frac{1 + 2\left(\frac{1}{2} - a_h\right)(1 - \psi_1 - \psi_2)}{\mu_s}$$

$$c_4 = \left(\frac{\omega_r}{V_r}\right)^2 + \frac{2}{\mu_s}(\psi_1\varepsilon_1 + \psi_2\varepsilon_2) \qquad c_5 = \frac{2}{\mu_s}\left[(1 - \psi_1 - \psi_2) + \left(\frac{1}{2} - a_h\right)(\psi_1\varepsilon_1 + \psi_2\varepsilon_2)\right]$$

$$c_6 = \frac{2}{\mu_s}\psi_1\varepsilon_1\left[1 - \left(\frac{1}{2} - a_h\right)\varepsilon_1\right] \qquad c_7 = \frac{2}{\mu_s}\psi_2\varepsilon_2\left[1 - \left(\frac{1}{2} - a_h\right)\varepsilon_2\right]$$

$$c_8 = -\frac{2}{\mu_s}\psi_1\varepsilon_1^2 \qquad c_9 = -\frac{2}{\mu_s}\psi_2\varepsilon_2^2$$

and the constants in Eq. (2.10b) are given by

$$d_0 = \frac{x_\alpha}{r_\alpha^2} - \frac{a_h}{\mu_s r_\alpha^2} \qquad d_1 = 1 + \frac{1 + 8a_h^2}{8\mu_s r_\alpha^2}$$

$$d_2 = \frac{(1 - 2a_h) - (1 + 2a_h)(1 - 2a_h)(1 - \psi_1 - \psi_2)}{2\mu_s r_\alpha^2} \qquad d_3 = -\frac{(1 + 2a_h)(1 - \psi_1 - \psi_2)}{\mu_s r_\alpha^2}$$

$$d_4 = \frac{1}{V_r^2} - \frac{(1 + 2a_h)(1 - \psi_1 - \psi_2)}{\mu_s r_\alpha^2} - \frac{(1 + 2a_h)(1 - 2a_h)(\psi_1\varepsilon_1 + \psi_2\varepsilon_2)}{2\mu_s r_\alpha^2} \qquad d_5 = \frac{\beta_\alpha}{V_r^2}$$

$$d_6 = \frac{\gamma_\alpha}{V_r^2} \qquad d_7 = -\frac{(1 + 2a_h)(\psi_1\varepsilon_1 + \psi_2\varepsilon_2)}{\mu_s r_\alpha^2}$$

$$d_8 = -\frac{(1+2a_h)\,\psi_1\varepsilon_1\left[1-\left(\frac{1}{2}-a_h\right)\varepsilon_1\right]}{\mu_s r_\alpha^2} \qquad d_9 = -\frac{(1+2a_h)\,\psi_2\varepsilon_2\left[1-\left(\frac{1}{2}-a_h\right)\varepsilon_2\right]}{\mu_s r_\alpha^2}$$

$$d_{10} = \frac{(1+2a_h)\,\psi_1\varepsilon_1^2}{\mu_s r_\alpha^2} \qquad d_{11} = \frac{(1+2a_h)\,\psi_2\varepsilon_2^2}{\mu_s r_\alpha^2}.$$

The forcing terms, $f(\tau)$ and $g(\tau)$ are given by

$$f(\tau) = \frac{2}{\mu_s}\left[\left(\frac{1}{2}-a_h\right)\alpha(0)+y(0)\right]\left(\psi_1\varepsilon_1 e^{-\varepsilon_1\tau}+\psi_2\varepsilon_2 e^{-\varepsilon_2\tau}\right) \tag{2.11a}$$

$$g(\tau) = -\frac{1+2a_h}{2r_\alpha^2}f(\tau). \tag{2.11b}$$

With this formulation, the equations of motion can be separated into eight first order, ordinary differential equations. By letting $x_1 = \alpha$, $x_2 = \dot{\alpha}$, $x_3 = y$, $x_4 = \dot{y}$, $x_5 = w_1$, $x_6 = w_2$, $x_7 = w_3$, and $x_8 = w_4$, the following equations result

$$\dot{x_1} = x_2 \tag{2.12a}$$

$$\dot{x_2} = \frac{c_0H - d_0P}{c_1d_0 - c_0d_1} \tag{2.12b}$$

$$\dot{x_3} = x_4 \tag{2.12c}$$

$$\dot{x_4} = -\frac{c_1H - d_1P}{c_1d_0 - c_0d_1} \tag{2.12d}$$

$$\dot{x_5} = x_1 - \varepsilon_1 x_5 \tag{2.12e}$$

$$\dot{x_6} = x_1 - \varepsilon_2 x_6 \tag{2.12f}$$

$$\dot{x_7} = x_3 - \varepsilon_1 x_7 \tag{2.12g}$$

$$\dot{x_8} = x_3 - \varepsilon_2 x_8 \tag{2.12h}$$

where

$$P = c_2x_4 + c_3x_2 + c_4x_3 + c_5x_1 + c_6x_5 + c_7x_6 + c_8x_7 + c_9x_8 - f(\tau) \tag{2.13a}$$

and

$$H = d_2x_2 + d_3x_4 + d_4x_1 + d_5x_1^3 + d_6x_1^5 + d_7x_3 + d_8x_5 + d_9x_6 + d_{10}x_7 + d_{11}x_8 - g(\tau). \tag{2.13b}$$

With the aeroelastic equations formulated as a system of first order, ordinary differential equations, a variety of methods are available for numerical integration. The method chosen here is a simple forward Euler integration. The time step should be 1/256 of the shorter period of the two coupled modes of oscillation for an accurate time integration [3]. Lee et al. [3] used a time step of $\Delta t = 0.1$ to satisfy this requirement. The same time step was used in this study.

2.4 Bifurcation Behavior

Bifurcations are a change in the stability of a system that results in different dynamic responses [32]. A linear aeroelastic system, at some critical reduced velocity, will undergo a change from a stable stationary (no motion) solution to divergent flutter (unbounded motion). This critical point is termed by aeroelasticians as the flutter point [1]. Nonlinear aeroelastic systems can stabilize beyond the flutter point to a periodic dynamic response [3, 2, 4]. Mathematicians term this change from a stationary response to a periodic response the Hopf bifurcation point [32]. Note that the flutter point and the Hopf bifurcation point are coincident for an aeroelastic system. The periodic motion beyond the flutter point has been termed limited amplitude flutter or limit cycle oscillation (LCO). While the latter term is more a mathematical term, its use is prevalent in the aeroelastic literature [2]. In this study, the terms flutter point and LCO are used.

Two different types of dynamic responses are examined in this study. The first type of response was described above and is termed a supercritical response. A supercritical response is a stable periodic solution for reduced velocity beyond the flutter point. As the reduced velocity decreases through the flutter point, the periodic solution reduces to the stationary solution. A supercritical response was obtained by Beran and Pettit [8]

and Millman et al. [31] from the aeroelastic system described in the previous sections with the following structural parameters:

$$\mu_s = 100 \qquad a_h = -0.5 \qquad x_\alpha = 0.25$$
$$\omega_r = 0.2 \qquad \beta_\alpha = 3 \qquad r_\alpha = -0.5$$
$$\gamma_\alpha = 20$$

The value for γ_α was selected to to stabilize a subcritical response, which will be discussed shortly. For this supercritical case, both Beran and Pettit [8] and Millman et al. [31] located the flutter point at $V_r \approx 6.28$. The time histories of pitch at $V_r = 6.1$, 6.2, 6.3 and 6.4 with an initial pitch of $\alpha(0) = 1^\circ$ are shown in Figure 2.2. The remaining initial conditions are given by $\dot{\alpha}(0) = y(0) = \dot{y}(0) = 0$. For reduced velocities below the flutter point, Figs. 2.2(a) and (b), the initial pitch displacement damps to no motion. At reduced velocities above the flutter point, Figs. 2.2(c) and (d), the initial pitch displacement causes the airfoil to exhibit an LCO. Also note that a longer time integration is required to obtain the final motion of the airfoil the closer the reduced velocity is to the flutter point. By plotting the LCO amplitude at various reduced velocities, the bifurcation diagram in Figure 2.3 results. Time integrations near the flutter point were carried out to $\tau = 20,000$ before the stable response (stationary or LCO) was achieved.

Lee et al. [3] demonstrated that a subcritical response, i.e., a dynamically unstable response, results when a negative value for the cubic spring constant, β_α, and a zero quintic restoring force ($\gamma_\alpha = 0$) are applied [3]. At reduced velocities above the flutter point, the airfoil will exhibit divergent flutter for any initial pitch except $\alpha(0) = 0$, the dynamically unstable stationary branch. With a large initial pitch, divergent flutter can also be exhibited at reduced velocities below the flutter point. A bifurcation diagram of a subcritical response is shown in Figure 2.4. The source of this instability can be seen in the pitch spring term

$$K_\alpha(\alpha + \beta_\alpha \alpha^3 + \gamma_\alpha \alpha^5)$$

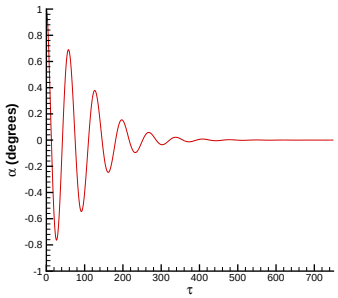

(a) $V_r = 6.1$

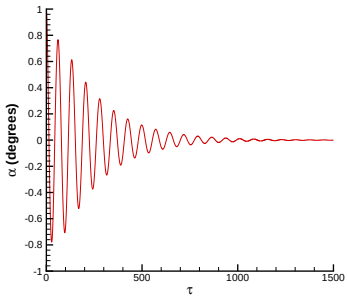

(b) $V_r = 6.2$

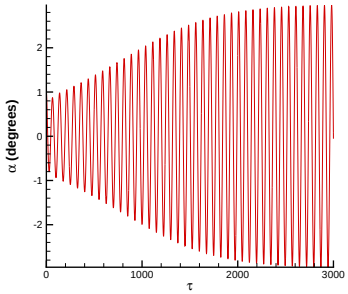

(c) $V_r = 6.3$

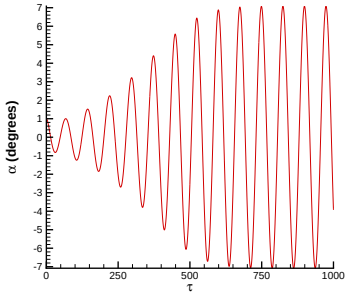

(d) $V_r = 6.4$

Figure 2.2 Time histories of pitch with $\alpha(0) = 1.0°$

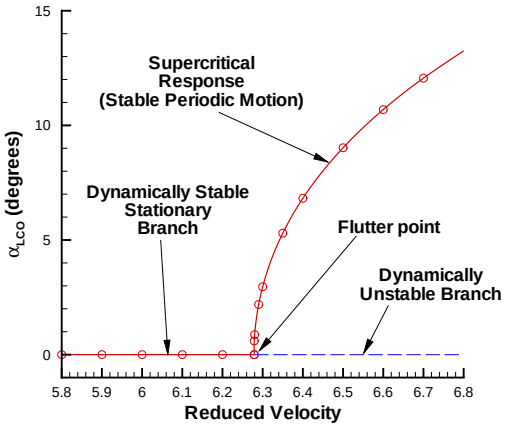

Figure 2.3 Bifurcation diagram of a supercritical response

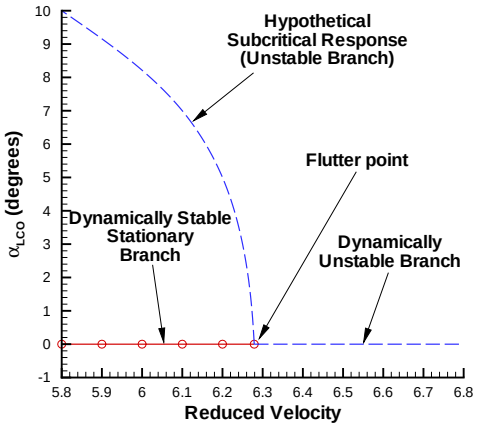

Figure 2.4 Bifurcation diagram of a subcritical response

in Eq. (2.1b). With the absence of the quintic spring constant γ_α, a negative value for cubic spring constant β_α can be viewed as loosening, or weakening, the pitch spring. For sufficiently large values of pitch, the negative cubic spring constant dominates the pitch spring resulting in a loss of stability.

In order to regain stability in the structure, Millman et al. [25] added the quintic restoring force in Eq. (2.1b). At large amplitudes, the quintic spring constant γ_α dominates the pitch spring and the structure exhibits a large amplitude LCO. Following Lee et al. [3], the cubic spring constant was changed from $\beta_\alpha = 3$ to $\beta_\alpha = -3$. Time histories of pitch are shown in Figure 2.5 at reduced velocities below and above the flutter point. At $V_r = 6.2$, below the flutter point, two responses are possible. With an initial pitch of $\alpha(0) = 5°$, Figure 2.5(a), the airfoil stabilizes at the stationary solution. However, if the initial pitch is increased to $\alpha(0) = 10°$, Figure 2.5(b), the airfoil exhibits a large amplitude LCO. At reduced velocities above the flutter point, Figure 2.5(c), even a small initial pitch, $\alpha(0) = 1°$, can lead to a large amplitude LCO. A bifurcation diagram with this subcritical response is shown in Figure 2.6.

The turning point in Figure 2.6 connects the subcritical branch to the stable periodic motion branch [32] and occurs at $V_r \approx 5.9$. The large amplitude LCO branch exhibits a hysteresis, i. e. the stationary solution bifurcates to the large amplitude LCO

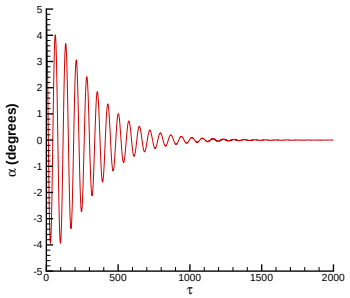

(a) $V_r = 6.2$, $\alpha(0) = 5°$

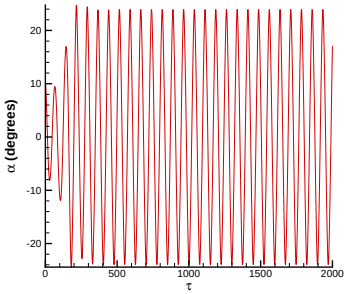

(b) $V_r = 6.2$, $\alpha(0) = 10°$

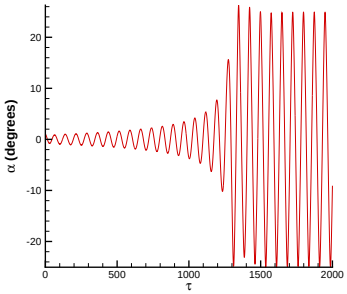

(c) $V_r = 6.3$, $\alpha(0) = 1°$

Figure 2.5 Time histories of pitch with $\beta_\alpha = -3$

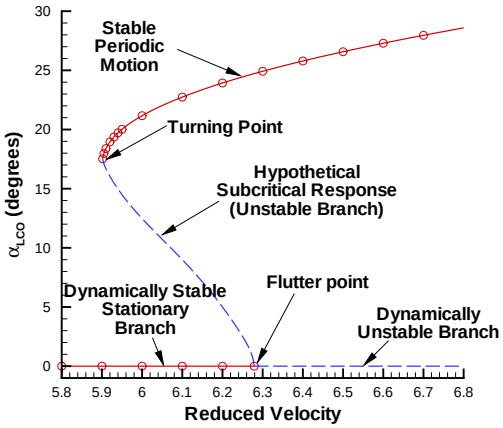

Figure 2.6 Bifurcation diagram of a subcritical response with a turning point

branch at the flutter point but the large amplitude LCO branch bifurcates to the stationary solution at the turning point. This hysteresis is not simply a pure mathematical construct, the same behavior has been observed in wind tunnel tests of a large aspect ratio wing [4] as well as in flight test of fighter aircraft [2]. The subcritical response with a turning point presents a greater risk to an aircraft than a supercritical response since a very large amplitude LCO can occur below the classically defined flutter point.

2.5 Uncertainty Quantification

While the analysis in the previous section was primarily deterministic, the initial pitch angle $\alpha(0)$ was carefully chosen, particularly in the case of the subcritical response, so that the desired behavior could be demonstrated. The initial pitch angle plays a key role in the large time behavior of this system. Thus, the initial pitch is chosen as a stochastic input.

It was also demonstrated in the previous section that the value of the cubic spring constant played a significant role in the dynamics of the response. While the location of the flutter point does not change with the introduction of the nonlinear structural parameters, the location of the turning point can change as these structural parameters are varied. For this reason, the second uncertainty parameter chosen in this study is the cubic spring constant, β_α.

Before analyzing how these uncertainties, $\alpha(0)$ and β_α, propagate in time, a distribution of the uncertainties must be selected. While any distribution can be chosen for this model problem, the most common starting point for stochastic projection methods such as the polynomial chaos expansion [15] is the Gaussian distribution. The Gaussian distribution allows a random variable to be expressed in terms of its mean value and its standard deviation. For example, realizations of the initial pitch angle and the cubic

spring constant are obtained from

$$\alpha(0) = \bar{\alpha}(0) + \xi_1 \tilde{\alpha}(0) \tag{2.14a}$$

$$\beta_\alpha = \bar{\beta}_\alpha + \xi_2 \tilde{\beta}_\alpha \tag{2.14b}$$

where the barred ($\bar{}$) quantities represent mean values, the tilde ($\tilde{}$) quantities represent standard deviations, and ξ_1 and ξ_2 are zero mean, unit variance Gaussian random variables. The mean value in the initial pitch angle is chosen as $\bar{\alpha}(0) = 0$. In order to obtain the desired responses shown in the previous section, a large initial pitch angle is required. This large initial pitch angle is generated by selecting $\tilde{\alpha}(0) = 0.2$ rads ($\approx 11.5°$). The mean value of the cubic spring constant determines whether a supercritical or subcritical response is produced. That is,

$$\bar{\beta}_\alpha = \begin{cases} 3 & \text{generates a supercritical response} \\ -3 & \text{generates a subcritical response} \end{cases} \tag{2.15}$$

The standard deviation of the cubic spring constant was chosen as $\tilde{\beta}_\alpha = 0.3$ for both the supercritical and subcritical responses. It should be emphasized that the parameters were chosen only to observe the desired responses.

Monte Carlo simulations of the nonlinear aeroelastic system are now performed in order to quantify the effects of the uncertainties. An MCS begins by choosing a sample size, N, and then obtaining N realizations of ξ_1 and ξ_2 based on the Gaussian distribution. These realizations of the random variables provide realizations of $\alpha(0)$ and β_α from Eqs. (2.14a) and (2.14b). Time integrations of the governing equations are then performed N times until a fully developed response (stationary or LCO) is obtained. The responses are saved as realizations and, through a Parzen windowing approach [36], used to estimate the PDF of the LCO response.

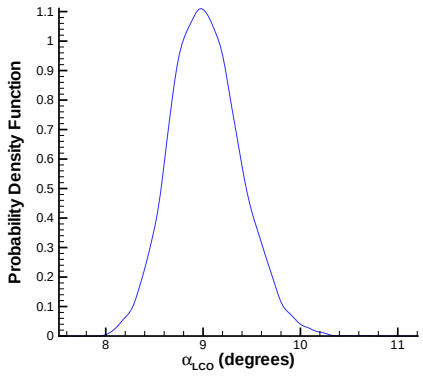

(a) $\bar{\beta}_\alpha = 3$, $V_r = 6.5$

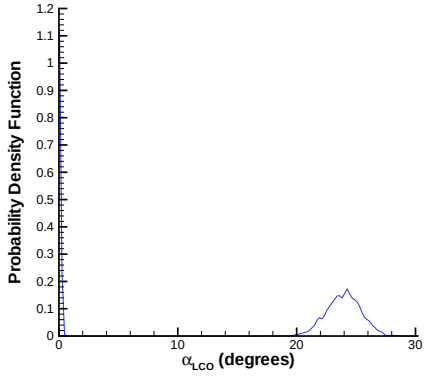

(b) $\bar{\beta}_\alpha = -3$, $V_r = 6.2$

Figure 2.7 Sample PDFs

The Parzen windowing approach provides a smooth estimate of the PDF through the following procedure. The maximum and minimum values of the LCO response are first determined. A buffer value, Δ, is computed as ten percent of the maximum value. Equally spaced nodes are selected on the interval $[(\alpha_{LCO})_{\min} - 0.5\Delta, (\alpha_{LCO})_{\max} + 0.5\Delta]$, where α_{LCO} is the pitch LCO response. Gaussian distributions of a specified standard deviation, σ, are placed over each of the nodes and the Gaussian densities of the responses are averaged together [36]. The standard deviation chosen was $\sigma = 0.005(\alpha_{LCO})_{\max}$. The choice in the interval and σ ensured the area under the PDF was identically one. With the smooth approximation to the PDF, the trapezoidal rule was used to obtain the area under the PDF. Sample PDFs at $V_r = 6.5$ for the supercritical response and $V_r = 6.2$ for the subcritical case are shown in Figures 2.7(a) and (b), respectively. It should be noted that for the subcritical case, the finite width of the PDF at $\alpha_{LCO} = 0$ is a result of the smoothing accomplished by the Parzen windowing approach.

Large time integrations were required to ensure the responses obtained were fully developed. In order to increase the efficiency of the MCS, i.e., decrease the required computer run times, the minimum sample size is selected that provides an accurate PDF of the response. One method for determining the minimum sample size required is to

run increasingly larger sample sizes and check for a convergence of the mean value, μ, of the response [37]. An MCS was run on the supercritical case with $V_r = 6.5$ and the subcritical case with $V_r = 6.2$. Computer run times and the mean LCO response are shown in Table 2.1. Each MCS for the supercritical case was integrated to a maximum time of $\tau_{\max} = 3000$. This was to ensure extremely small initial pitch angles achieved a fully developed LCO. For the subcritical response, a maximum time of $\tau_{\max} = 10000$ was required to achieve either a fully developed stationary response or a fully developed LCO. From Table 2.1, it was determined that $N = 4000$ would be a sufficient sample size to obtain accurate PDFs of both the supercritical and subcritical responses with the least amount of computational effort.

The effect of the uncertainties on the bifurcation behavior is demonstrated for the supercritical case in Figure 2.8(a) and (b). The supercritical response now has a range of possible LCO amplitudes for each reduced velocity owing to the uncertainty in the cubic spring constant. The PDFs allow an estimate of failure for the aeroelastic system. Failure is defined as the probability of encountering an LCO. Due to the smoothing of the Parzen windowing approach near $\alpha_{LCO} = 0$ for the subcritical case, failure is determined from a pitch LCO amplitude exceeding $\pm 1^\circ$. The area under the PDF from $\alpha_{LCO} = 1^\circ$ to the maximum LCO amplitude yields the probability of failure. The probability of failure for the supercritical case is 100% at and above the flutter point.

Table 2.1 Convergence of the mean on MCSs of supercritical and subcritical responses

	Supercritical ($\tau_{\max} = 3000$)		Subcritical ($\tau_{\max} = 2000$)	
N	Run time (secs)	μ	Run time (secs)	μ
1000	27.98	9.03	154.1	13.9
2000	55.86	9.04	307.9	13.2
3000	83.88	9.04	460.0	13.4
4000	112.1	9.05	614.4	13.5
5000	140.1	9.04	767.7	13.6
6000	169.8	9.04	922.5	13.6

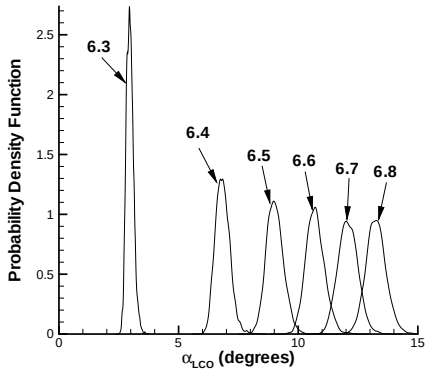

(a) **PDFs at various reduced velocities**

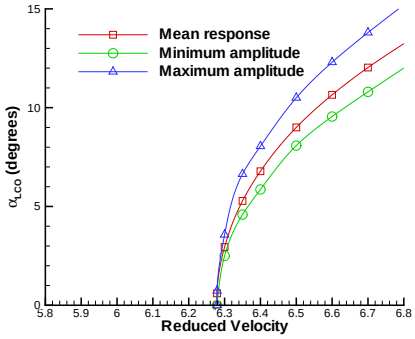

(b) **Bifurcation diagram**

Figure 2.8 Effects of uncertainties on the supercritical response

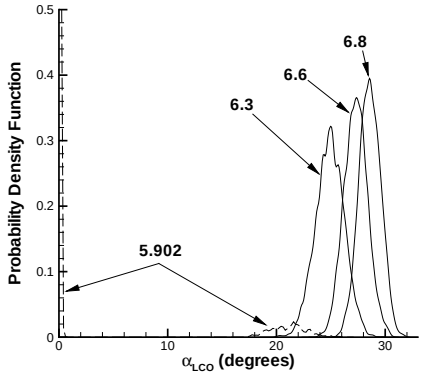

(a) **PDFs at various reduced velocities**

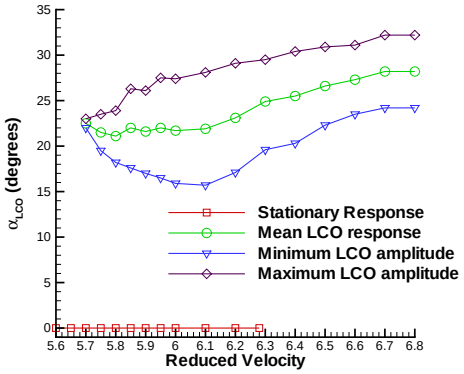

(b) **Bifurcation diagram**

Figure 2.9 Effects of uncertainties on the subcritical response

The effects of the uncertainties on the subcritical response are shown in Figs. 2.9(a) and (b). Again, the uncertainty in the cubic spring constant leads to a range of LCO amplitudes. Introducing uncertainty into the nonlinear system affects the location of the turning point, which now has a probability of occurring as low as $V_r \approx 5.7$. This variation in the location of the turning point agrees well with the results reported by Beran and Pettit[8]. With the same definition of failure given above, the probability of

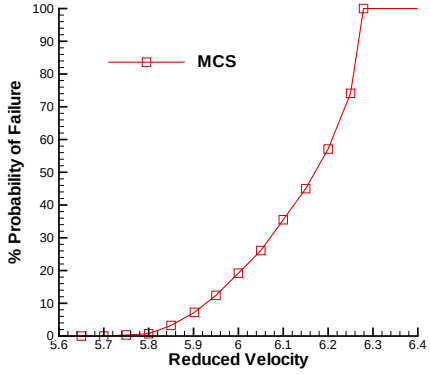

Figure 2.10 Probability of failure for the subcritical response

failure for the subcritical case is shown in Figure 2.10. While LCO below the flutter point was introduced by the nonlinear restoring forces, the initial condition uncertainty and parametric uncertainty increase the range where failure can occur below the flutter point.

2.6 Summary

In this chapter, a nonlinear aeroelastic system was described that leads to supercritical or subcritical responses based upon the structural parameters chosen. Uncertainty was introduced in the analysis by assigning a Gaussian distribution to the initial pitch angle and the cubic spring constant in pitch. The response examined was the LCO amplitude in pitch. It was shown that the flutter point is a function of the linear system only, while the turning point of the subcritical response is affected by both nonlinearities and uncertainties. The turning point is associated with LCO, and structural failure, at reduced velocities below the flutter point. Thus, to predict probability of failure, both nonlinearities and uncertainties must be included in the design analysis. The next chapter presents a new stochastic algorithm that can efficiently quantify the effects of uncertainties in the nonlinear aeroelastic system.

III. Development and Implementation of the Stochastic Projection Method via B-Splines

3.1 Introduction

The previous chapter presented an MCS analysis to determine the probability of failure of an aeroelastic system. While the MCS approach is robust enough to capture both supercritical and subcritical bifurcations, it is computationally inefficient. In this chapter, the stochastic projection of the pitch LCO response, α_{LCO}, is examined with respect to the stochastic axes. This examination reveals that the underlying behavior of a bifurcation in the stochastic domain is discontinuous and not amenable to spectral approaches, such as the PCE and FCE methods. A B-spline algorithm for the stochastic projection method is developed and applied to the problem of the structurally nonlinear airfoil with linear aerodynamics studied in the previous chapter. It is shown that this B-spline stochastic algorithm is both efficient and robust enough to deal with the discontinuous behavior associated with bifurcations.

3.2 Stochastic Projection

A stochastic projection is a projection of the response onto the random variables. Typically this projection is obtained at a specific instance in time. For a time domain analysis, at a very large time, these projections can become so complicated (nonlinear, discontinuous) in form that even a very large order expansion cannot capture the shape of the projection [26]. Beran and Pettit [8] circumvent this issue with the non-intrusive PCE approach. The non-intrusive PCE approach essentially removes the time dependency by obtaining samples of the LCO response once the LCO is fully developed. Beran and Pettit's [8] results were obtained from an efficient cyclic approach, not involving a time domain analysis. This present work examines the stochastic projections from a time domain approach.

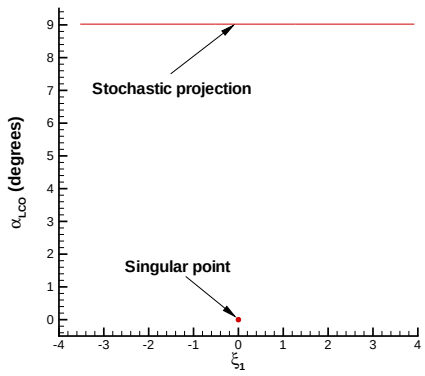

(a) $\boldsymbol{V_r = 6.5}$, $\boldsymbol{\bar{\beta}_\alpha = 3.0}$, $\boldsymbol{\tilde{\beta}_\alpha = 0.0}$, $\boldsymbol{\bar{\alpha}(0) = 0}$, $\boldsymbol{\tilde{\alpha}(0) = 0.2}$

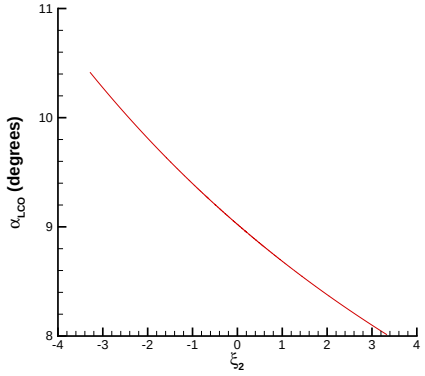

(b) $\boldsymbol{V_r = 6.5}$, $\boldsymbol{\bar{\beta}_\alpha = 3.0}$, $\boldsymbol{\tilde{\beta}_\alpha = 0.3}$, $\boldsymbol{\bar{\alpha}(0) = 0.261779}$, $\boldsymbol{\tilde{\alpha}(0) = 0}$

Figure 3.1 Stochastic projection of α_{LCO} onto the random variables ξ_1 and ξ_2 (supercritical response)

To better understand the behavior of the stochastic projections, two projections are plotted in Figure 3.1. These projections were obtained from a four thousand MCS for the supercritical case ($\bar{\beta}_\alpha = 3.0$) at $V_r = 6.5$. The responses were sorted with respect to each random variable. In Figure 3.1(a) a four thousand run MCS was performed with the cubic spring constant held at $\beta_\alpha = 3$ while the initial pitch angle was allowed to vary. The stochastic projection of the response, α_{LCO}, with respect to the uncertainty in the initial pitch angle, ξ_1, appears to be a smooth continuous function, but a singular point exists at $\xi_1 = 0$. This singularity corresponds to the dynamically unstable equilibrium branch on the bifurcation diagram (Figure 2.3). The MCS was repeated holding the initial pitch angle fixed at $\alpha(0) = 15°$, to ensure LCO developed, and allowing the cubic spring constant β_α to vary. Figure 3.1(b) shows the stochastic projection of the response with respect to the uncertainty in the cubic spring constant, ξ_2 is a smooth continuous function.

The stochastic projections for the subcritical response $\beta_\alpha = -3$ at $V_r = 6.2$ are shown in Figure 3.2. In Figure 3.2(a), the stochastic projection of the response with respect to the uncertainty in initial pitch indicates two jumps between a large LCO

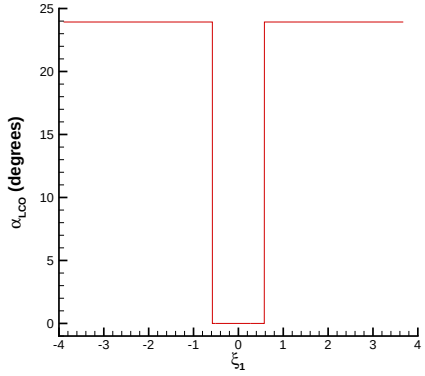

(a) $\boldsymbol{V_r = 6.2,}$ $\boldsymbol{\bar{\beta}_\alpha = -3.0,}$ $\boldsymbol{\tilde{\beta}_\alpha = 0.0,}$ $\boldsymbol{\bar{\alpha}(0) = 0,}$ $\boldsymbol{\tilde{\alpha}(0) = 0.2}$

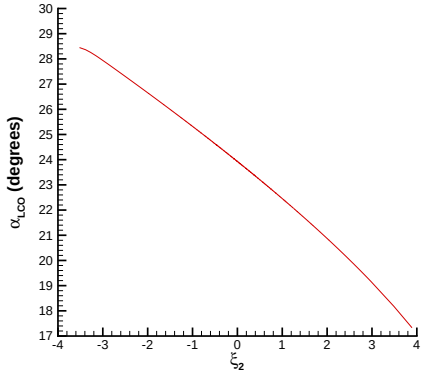

(b) $\boldsymbol{V_r = 6.2,}$ $\boldsymbol{\bar{\beta}_\alpha = -3.0,}$ $\boldsymbol{\tilde{\beta}_\alpha = 0.3,}$ $\boldsymbol{\bar{\alpha}(0) = 0.261779,}$ $\boldsymbol{\tilde{\alpha}(0) = 0}$

Figure 3.2 Stochastic projection of α_{LCO} onto the random variables ξ_1 and ξ_2 (subcritical response)

amplitude and a stationary response. This discontinuous behavior is a manifestation of the subcritical branch with a turning point as illustrated in Figure 2.6. Above a certain absolute value of the initial pitch angle, an LCO develops. Below this absolute value of the initial pitch angle, a dynamically stable stationary solution is achieved. In Figure 3.2(b), with an initial pitch angle of $\alpha(0) = 15^\circ$ and β_α allowed to vary, the stochastic projection with respect ξ_2 is a smooth continuous function.

3.3 Stochastic Projection Method via B-Splines

The stochastic projections shown in the previous section demonstrate that while a polynomial expansion may be appropriate for the supercritical case (Figure 3.1), provided the singular point at $\xi_1 = 0$ is not included in the development of the expansion, a polynomial expansion is inappropriate for the subcritical case (Figure 3.2) due to the discontinuous behavior in the projection with respect to ξ_1. Indeed, any spectral approach would have difficulty in resolving the discontinuous behavior.

The stochastic projections can be treated, however, as piecewise continuous over the interval of interest. Splines would then be an appropriate choice for approximating the stochastic projections. An important property of the multivariate B-splines chosen for this work is that they are a compact support basis; that is, the influence of any particular B-spline coefficient extends over a few intervals [30]. The practical importance of this property is that oscillations in the vicinity of discontinuous behavior can be avoided with the proper choice in the order of the B-spline. The order used in this work is $k_{\xi_1} = k_{\xi_2} = 2$, which is equivalent to a piecewise linear interpolation [30]. The expansion of the univariate B-splines for ξ_1 and ξ_2 are given by

$$\alpha(\xi_1) = \sum_{i=1}^{N_{\xi_1}} \hat{\alpha}_{i,\xi_1} B_{i,k_{\xi_1},\boldsymbol{x}_{\xi_1}}(\xi_1) \tag{3.1}$$

$$\alpha(\xi_2) = \sum_{j=1}^{N_{\xi_2}} \hat{\alpha}_{j,\xi_2} B_{j,k_{\xi_2},\boldsymbol{x}_{\xi_2}}(\xi_2) \tag{3.2}$$

where $\boldsymbol{x}_{\xi_1}$ is the vector of N_{ξ_1} knots on the ξ_1 axis and $\boldsymbol{x}_{\xi_2}$ is the vector of N_{ξ_2} knots on the ξ_2 axis. The multivariate B-spline is the tensor product of the two univariate B-splines and can be explicitly written as [30]

$$\alpha(\xi_1, \xi_2) = \sum_{i=1}^{N_{\xi_1}} \sum_{j=1}^{N_{\xi_2}} \hat{\alpha}_{ij} B_{j,k_{\xi_2},\boldsymbol{x}_{\xi_2}}(\xi_2) B_{i,k_{\xi_1},\boldsymbol{x}_{\xi_1}}(\xi_1) \ . \tag{3.3}$$

The coefficient matrix, made up of the elements $\hat{\alpha}_{ij}$, is solved by repeated evaluations of the univariate spline interpolation problem, the details of which are given in de Boor [30].

Now an efficient stochastic algorithm that is robust enough to identify bifurcations can be described. First, an interval is chosen in the stochastic domain over which samples of the LCO amplitude will be obtained. Next, the location of nodes to be sampled in that interval is determined. The multivariate B-spline that approximates the response surface in the stochastic domain is then determined. Finally, an MCS is performed on

this response surface to estimate the PDF of the response. Each of the steps of this algorithm are now described in detail.

The interval selected is based on the distribution of random variables. For this work, the random variables have a Gaussian distribution. Strictly speaking, the interval defined for a Gaussian random variable is the whole real line. There is, however, a practical limit to this interval. The random variables control parametric uncertainties and these parameters must be kept within specified bounds in order for the equations of motion to be numerically well behaved. In a real world application the mean and standard deviation may be dictated by manufacturing, instrument error, or physical phenomena such as wind gusts. For this model problem the mean and standard deviation were selected to illustrate supercritical and subcritical responses. It was found that for the large standard deviation chosen for the initial pitch angle, $\tilde{\alpha}(0) = 0.2$ radians, the model problem became unstable for large values of ξ_1 ($\xi_1 > 4$). Since

$$\left(\frac{1}{\sqrt{2\pi}}\right)^2 \int_{-4}^{4}\int_{-4}^{4} e^{-\frac{1}{2}\left(\xi_1^2+\xi_2^2\right)}\, \mathrm{d}\xi_1\, \mathrm{d}\xi_2 \approx 0.99994\ , \tag{3.4}$$

99.99% of all responses occur on the interval [-4,4] in both stochastic axes. Thus, this was the interval selected for both the ξ_1 and ξ_2 axes.

With the interval selected, nodes along the stochastic axis must be chosen that will efficiently capture the desired projection. In order for the B-spline to be valid over the entire interval, nodes must be selected that span the entire interval. However a Gaussian distribution of the nodes would cluster the nodes near the mean value, leaving a large gap between the Gaussian spaced nodes and the endpoints of the interval. Nodes at ± 4 are required to span the interval. Nodes at ± 2.5 are added to bridge the gap between the Gaussian spaced nodes and the endpoints of the interval. The Gaussian spaced nodes are determined by integration of the Gaussian PDF, $w(\xi_1)$ or $w(\xi_2)$ (Eq. (1.6) with $d = 1$). That is, the nodes are determined in one dimension and the same nodes are used in the other dimension. The determination of the nodes proceeds as follows. Some number of

Table 3.1 Gaussian distributed nodes

$I = 2$	$I = 4$	$I = 8$
–	–	± 0.15731
–	± 0.31864	± 0.31684
–	–	± 0.48878
± 0.67449	± 0.67449	± 0.67449
–	–	± 0.88715
–	± 1.15035	± 1.15035
–	–	± 1.53412
± 2.5	± 2.5	± 2.5
± 4.0	± 4.0	± 4.0

nodes are selected on the interval $[0, 4]$. Let this number of nodes be represented by I along the ξ_1 axis and J along ξ_2 axis. Noting that

$$\int_0^4 \frac{1}{\sqrt{2\pi}} e^{-\frac{1}{2}\xi_1^2} \, \mathrm{d}\xi_1 \approx \frac{1}{2} \tag{3.5}$$

the remaining nodes are selected based on equal intervals of the probabilities. For example, with $I = 2$ and one node fixed at $\xi_1 = 4$, the second node is determined from

$$\int_0^a \frac{1}{\sqrt{2\pi}} e^{-\frac{1}{2}\xi_1^2} \, \mathrm{d}\xi_1 = \frac{1}{4} \tag{3.6}$$

where a is the location of the node. A simple search leads to a value of $a = 0.67449$. Proceeding in a like manner for $I = 4$ and $I = 8$ leads to the node values given in Table 3.1. Due to the symmetry of the nodes and the extra nodes at $\xi_1 = \pm 2.5$, the total number of nodes along the ξ_1 stochastic axis is given by $2I + 2$.

Samples of the response are obtained at the selected values of ξ_1 and ξ_2. From these samples, the multivariate B-spline problem can be solved for the coefficient matrix, $\hat{\alpha}_{ij}$ in Eq. (3.3). After these coefficients are determined, an MCS is performed on Eq. (3.3). This MCS is extremely efficient, as is demonstrated in the next section.

Before preceeding to the next section, it is noted that this algorithm fits into the stochastic projection framework through the following derivation. Consider the set of

nodes $\boldsymbol{x}$ such that $x_i \in [-a, a]$ and $x_1 = -a < x_2 < \cdots < x_I = a$ for some integer I. Since it was noted that the above algorithm is a piecewise linear interpolation, the appropriate basis for expansion would be the hat function, which has the property [30]

$$\Psi_j(x_i) = \delta_{ij} \tag{3.7}$$

where δ_{ij} is the Dirac delta function. Thus

$$\Psi_j(x_i) = \begin{cases} 1 & i = j \\ 0 & i \neq j \end{cases} \tag{3.8}$$

Also notice that $\delta_j(x) = \delta(x - x_j)$, which indicates sampling at a node. Then inner products with $w(x) = 1$ are given as

$$\langle \Psi_i, \delta_j \rangle = \int_{-a}^{a} \Psi_i(x)\delta(x - x_j)\, \mathrm{d}x = \Psi_i(x_j) = \delta_{ij} \tag{3.9}$$

$$\langle x\Psi_i, \delta_j \rangle = \int_{-a}^{a} x\Psi_i(x)\delta(x - x_j)\, \mathrm{d}x = x_j\Psi_i(x_j) = x_j\delta_{ij} \tag{3.10}$$

The piecewise linear approximation to the response $\alpha(t, x)$ becomes

$$\alpha(t, x) = \sum_{i=1}^{I} \hat{\alpha}_i(t)\Psi_i(x) \tag{3.11}$$

and can be substituted into Eq. (1.3). By performing the stochastic projection as described by Le Maître [18] and making use of the above inner products, the following equation results

$$\mathcal{L}[\hat{\alpha}_j(t)] + \left(\bar{\beta}_\alpha + x_j\tilde{\beta}_\alpha\right)\hat{\alpha}_j^3(t) = 0 \tag{3.12}$$

Thus, the samples of the random variable are used to obtain samples of the response and a piecewise linear approximation to the response is obtained from the B-splines. While the PCE method provides a best fit to the stochastic projection and converges, in the mean square sense to an MCS, [38] the piecewise linear interpolation is exact at the

nodes and converges exactly to the MCS when the number of nodes equals the number of samples obtained by the MCS.

3.4 Results

The stochastic algorithm is now applied to the aeroelastic system described in the previous chapter. The supercritical case is examined first. Setting $I = 2$ and holding the cubic spring constant at $\beta_\alpha = 3.0$, samples were obtained along the ξ_2 axis at $V_r = 6.5$ to determine the coefficients $\hat{\alpha}_{i,\xi_1}$ in Eq. (3.1). An MCS on Eq. (3.1) produced the stochastic projection shown in Figure 3.3(a). Setting $J = 2$ and holding the initial pitch constant at $\alpha(0) = 15°$, samples were obtained along the ξ_2 axis. The univariate spline, Eq. (3.2) was solved for the coefficients $\hat{\alpha}_{j,\xi_2}$ and an MCS on this equation produced the stochastic projection shown in Figure 3.3(b). These projections are in excellent agreement with the projections shown in Figure 3.1. This should be expected since the projections are linear or very nearly linear across the respective intervals.

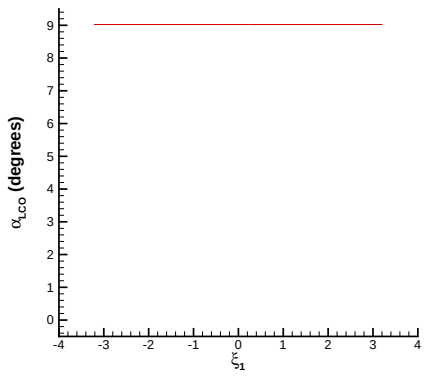

(a) $\boldsymbol{V_r = 6.5}$, $\boldsymbol{\bar{\beta}_\alpha = 3.0}$, $\boldsymbol{\tilde{\beta}_\alpha = 0.0}$, $\boldsymbol{\bar{\alpha}(0) = 0}$, $\boldsymbol{\tilde{\alpha}(0) = 0.2}$, $\boldsymbol{I = 2}$

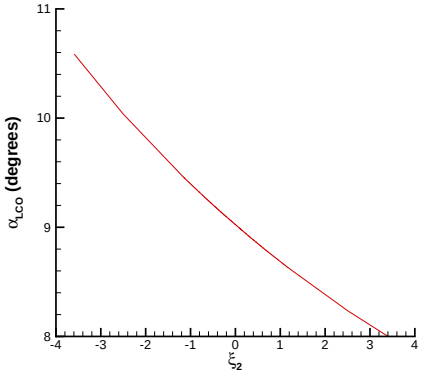

(b) $\boldsymbol{V_r = 6.5}$, $\boldsymbol{\bar{\beta}_\alpha = 3.0}$, $\boldsymbol{\tilde{\beta}_\alpha = 0.3}$, $\boldsymbol{\bar{\alpha}(0) = 0.261779}$, $\boldsymbol{\tilde{\alpha}(0) = 0.0}$,$\boldsymbol{J = 2}$

Figure 3.3 Stochastic projection of α_{LCO} onto the random variables ξ_1 and ξ_2 (supercritical response)

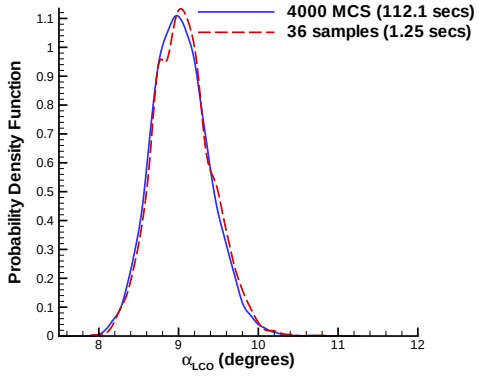

Figure 3.4 PDF comparisons for the supercritical response

Now allowing both the initial pitch angle and the cubic spring constant to vary and setting $I = 2$ and $J = 2$, thirty-six samples of the LCO responses were obtained. After the coefficients in Eq. (3.3) were determined, an MCS was performed on this equation. The PDF of the response was computed and compared to the PDF from the MCS on the governing equations. The agreement between the two PDFs is excellent, as shown in Figure 3.4. Again this should be expected due to the smoothness of the approximated functions. Obtaining samples of the response, solving the multivariate B-spline problem, and performing an MCS on Eq. (3.3) was two orders of magnitude faster than performing an MCS on the governing equations.

The subcritical response was examined at $V_r = 6.2$. The stochastic projection in Figure 3.5(a) was obtained as before with the initial pitch angle allowed to vary and the cubic spring constant held at $\beta_\alpha = -3$. The stochastic projection in Figure 3.5(b) was obtained by allowing the cubic spring constant to vary and keeping the initial pitch at $\alpha(0) = 15°$. The projection with respect to ξ_1 required $I = 8$ (18 samples) to obtain a good approximation to the discontinuous behavior. The projection with respect to ξ_2 required $J = 4$ (10 samples) to obtain the proper curvature. These stochastic projections compare well with those in Figure 3.2.

Again allowing both the initial pitch angle and the cubic spring constant to vary, PDFs were obtained from the stochastic projection method with $I = 2, 4$, and 8 and

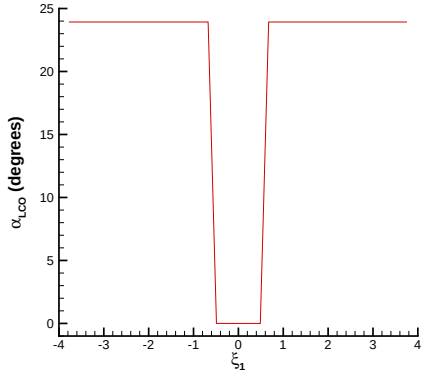

(a) $\boldsymbol{V_r = 6.2,\quad \bar{\beta}_\alpha = -3.0,\quad \tilde{\beta}_\alpha = 0.0,\ \bar{\alpha}(0) = 0,\ \tilde{\alpha}(0) = 0.2,\quad I = 8}$

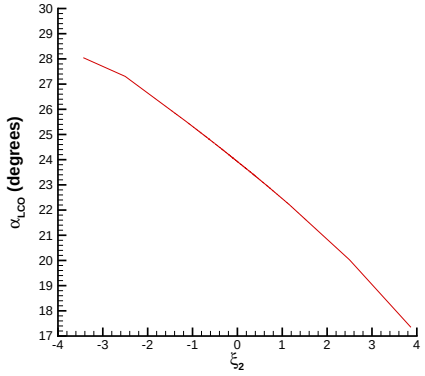

(b) $\boldsymbol{V_r = 6.2,\quad \bar{\beta}_\alpha = -3.0,\quad \tilde{\beta}_\alpha = 0.3,\quad \bar{\alpha}(0) = 0.261779,\quad \tilde{\alpha}(0) = 0.0, J = 4}$

Figure 3.5 Stochastic projection of α_{LCO} onto the random variables ξ_1 and ξ_2 (subcritical response)

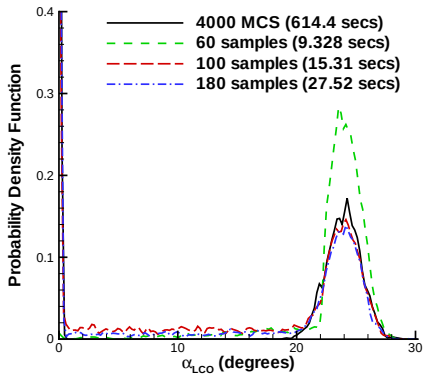

Figure 3.6 PDF comparisons for the subcritical response

$J = 4$, (60, 100, and 180 samples, respectively). These PDFs are compared with the PDF from the MCS and are shown in Figure 3.6. As the number of nodes increase along the ξ_1 axis, agreement with the PDF obtained from the MCS improves rapidly. The PDF with $I = 4$, is already in excellent agreement with the MCS results. With $I = 8$, the steeper slope in the approximation of the discontinuous behavior results in fewer realizations between the peak and secondary responses (a better bi-modal approximation).

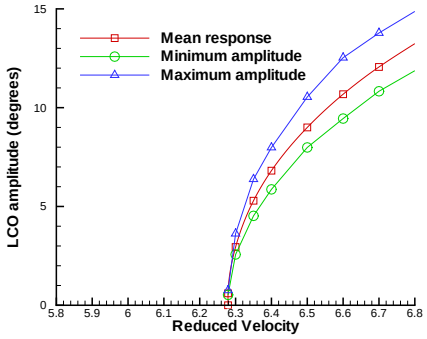

(a) **Supercritical response**

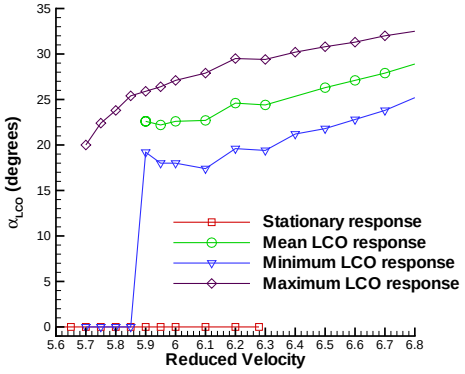

(b) **Subcritical response**

Figure 3.7 Bifurcation diagrams built with the stochastic projection method

With the stochastic algorithm verified for the above cases, bifurcation diagrams with the inclusion of uncertainties were developed. For $\bar{\beta}_\alpha = 3$, PDFs were obtained over the same range of reduced velocities as for the MCSs. Setting $I = J = 2$ was sufficient for these cases since all the responses were supercritical. For $\bar{\beta}_\alpha = -3$, the PDFs below the flutter point were obtained with $I = 8$ and $J = 4$, since these responses were subcritical. Above the flutter point, once again $I = J = 2$ was sufficient. These PDFs were then used to build the bifurcation diagrams shown in Figure 3.7. For the supercritical case, the mean pitch LCO amplitudes from the stochastic projection method are within 2% of the amplitudes from the MCS results (see Figure 2.8(b)). The mean pitch LCO amplitudes for the subcritical case were much more difficult to determine. Due to the lack of resolution in the ξ_1 axis, numerous responses are realized between the stationary response and the maximum pitch LCO amplitude (see Figure 3.6). A minimum pitch LCO amplitude could not be determined below $V_r = 5.902$. Thus, while the stochastic algorithm accurately predicts an LCO response below $V_r = 5.902$, only the maximum value of that response could be determined. Above $V_r = 5.902$, the mean pitch LCO amplitudes were within 2% of the amplitudes predicted by the MCS analysis (see Figure

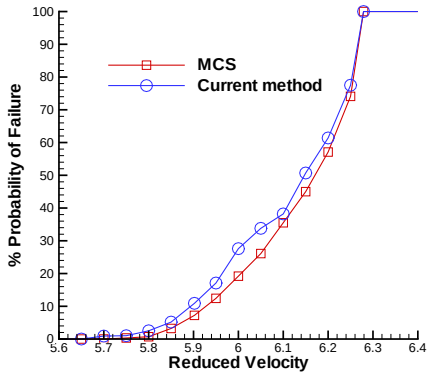

Figure 3.8 Comparison of probability of failure predictions with MCS and B-spline algorithm

2.9(b)). It should be noted that the time required to build these bifurcation diagrams was approximately two orders of magnitude less than with the MCS approach.

From the subcritical responses, an estimate of the probability of failure was obtained. As in the MCS analysis, failure is defined as encountering an LCO. The probability of failure is computed by integrating the area under the PDF from $\alpha_{LCO} = 1^\circ$ to the maximum LCO pitch amplitude. A comparison between the MCS prediction and the B-spline prediction is shown in Figure 3.8. The presence of realizations between the peak and secondary responses lead to a conservative estimate in the probability of failure, as seen in Table 3.2. Each failure estimate from the MCS required over ten minutes of computer time, while each estimate from the stochastic algorithm required approximately fifteen seconds.

3.5 Summary

An efficient algorithm for determining the propagation of uncertainties in a highly nonlinear aeroelastic system has been presented. The uncertainty in the initial pitch angle $\alpha(0)$ was allowed to propagate in a time dependent manner until an LCO or a dynamically stable solution was achieved. The stochastic algorithm consisted of building an interpolating function in the stochastic domain through sampling and the use of a

Table 3.2 Estimates for the probability of failure

Reduced Velocity (V_r)	MCS (%)	Stochastic Algorithm (%)	Difference (%)
5.70	0.005	0.91	0.905
5.75	0.33	1.02	0.69
5.80	0.70	2.52	1.82
5.85	3.23	5.17	1.94
5.90	7.23	10.9	3.67
5.95	12.4	17.1	4.7
6.00	19.2	27.6	8.4
6.05	26.1	33.8	7.7
6.10	35.5	38.2	2.7
6.15	45.0	50.7	5.7
6.20	57.1	61.4	4.3
6.25	74.1	77.5	3.4
6.279	100.0	100.0	0

multivariate B-spline. Advantages of this method over the traditional PCE approach were that expected values were never computed or stored and two orders of magnitude reduction in computational time over an MCS analysis were obtained. Based on the PDFs predicted by the stochastic algorithm, a rapid and accurate estimate of the probability of failure was also obtained. It should be noted that while, thus far, only the pitch LCO amplitude has been examined as a response, the stochastic algorithm is easily extended to examining other responses such as plunge LCO amplitude or the coupled pitch and plunge frequency. These additional responses will be examined in the next chapter where a computation of the nonlinear aerodynamics is obtained from the Euler equations.

IV. The Inviscid Aeroelastic Code EULER-AE

4.1 Introduction

To this point aerodynamic nonlinearities in the aeroelastic system have been neglected. Limit cycle oscillations often occur in transonic flow [2], where the nonlinearities due to moving shocks cannot be ignored. Other effects, such as boundary layer separation and turbulence, are also important in the study of LCO at transonic speeds [5]; however, many researchers have demonstrated LCOs on typical airfoil sections with the inviscid Euler equations [34, 39, 40, 41]. Therefore, validation of the stochastic algorithm presented in the previous chapter does not require viscosity to be included in the modeling of the fluid dynamics.

An inviscid aeroelastic code, EULER-AE, has been developed to investigate the response of a nonlinear airfoil in an inviscid transonic flow. The code implements a finite volume formulation and loose coupling between the structure and fluid, i.e., the structural dynamics lag the fluid dynamics by the integration time step size. The airfoil selected for this study was the symmetric NACA 64A006 airfoil. This airfoil was investigated by Morton and Beran [34] to determine the flutter point of a linear airfoil ($\beta_\alpha = \gamma_\alpha = 0$) in inviscid flow. The grid generation and dynamic boundary conditions used by EULER-AE are presented. The nonlinear airfoil equations are modified to use the notation of Morton and Beran [34]. The strategy of EULER-AE is to first attempt convergence to a steady state solution at a fixed initial pitch angle. Once convergence or the maximum number of iterations is achieved, the airfoil is allowed to move subject to the lift and moment induced by the fluid flow (See Figure 4.1). Static solutions with the airfoil at different angles of attack were computed with EULER-AE and compared against results from the commercial fluid solver FLUENT™ as well as experimental data [42]. A comparison with the parameters used by Morton and Beran to obtain an LCO for this airfoil is also presented.

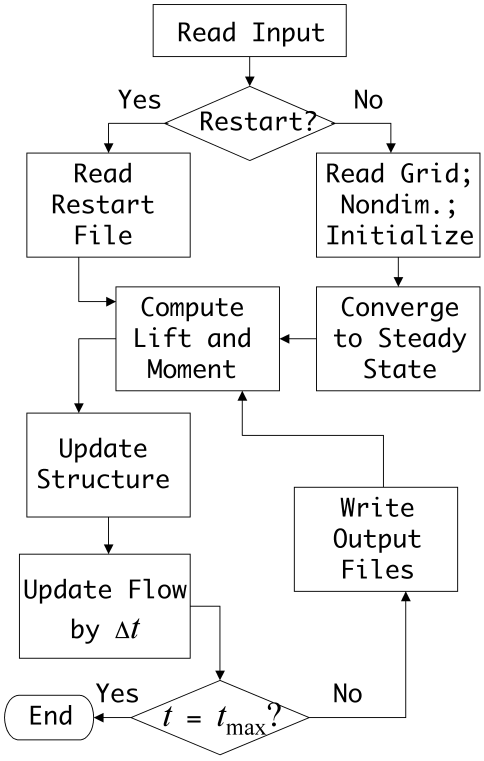

Figure 4.1 EULER-AE Flow Chart

4.2 Euler Equations

Before presenting the Euler equations, a new set of nondimensional parameters are introduced. In Sec. 2.2 the nondimensionalization was based on the airfoil midchord, b, as a reference length. In CFD algorithms, the airfoil chord, c, is typically chosen as a reference length. The nondimensional parameters are now

$$\begin{aligned} x^* &= \frac{x}{c} & y^* &= \frac{y}{c} & u^* &= \frac{u}{V_\infty} & v^* &= \frac{v}{V_\infty} \\ \rho^* &= \frac{\rho}{\rho_\infty} & p^* &= \frac{p}{\rho_\infty V_\infty^2} & E_t^* &= \frac{E_t}{\rho_\infty V_\infty^2} & t^* &= \frac{t\,V_\infty}{c} \end{aligned} \tag{4.1}$$

From this point the asterisk is dropped from the nondimensional parameters and the primitive variables and grid locations are assumed to be nondimensional unless otherwise stated.

The Euler equations in generalized coordinates with a moving grid are given by [43]

$$\frac{\partial}{\partial t}\left(\frac{1}{J}\mathbf{Q}\right)+\frac{\partial}{\partial \xi}\left(\frac{1}{J}\mathbf{E}\right)+\frac{\partial}{\partial \eta}\left(\frac{1}{J}\mathbf{F}\right)=0 \tag{4.2}$$

where the Jacobian J is equivalent to the cell volume, the conserved variables are

$$\mathbf{Q}=\begin{bmatrix}\rho\\ \rho u\\ \rho v\\ E_t\end{bmatrix} \tag{4.3}$$

and the flux vectors are given by

$$\mathbf{E}=\begin{bmatrix}\rho U\\ \xi_x p+\rho U u\\ \xi_y p+\rho U v\\ (p+E_t)U-\xi_t p\end{bmatrix}, \qquad \mathbf{F}=\begin{bmatrix}\rho V\\ \eta_x p+\rho V u\\ \eta_y p+\rho V v\\ (p+E_t)V-\eta_t p\end{bmatrix}. \tag{4.4}$$

The contravarient velocities U and V are obtained from

$$U=\xi_t+\xi_x u+\xi_y v \tag{4.5a}$$

$$V=\eta_t+\eta_x u+\eta_y v \tag{4.5b}$$

For a finite volume approach, the spatial metrics of transformation (ξ_x, ξ_y, η_x, and η_y) are obtained from a relationship with the area vectors normal to the cell faces [44]. The temporal metrics of transformation are obtained from a first order backward difference. At time level n, the x-component and y-component of the grid velocity are given by

$$x_t=\frac{x^n-x^{n-1}}{\Delta t} \tag{4.6a}$$

$$y_t=\frac{y^n-y^{n-1}}{\Delta t}\,, \tag{4.6b}$$

respectively, and the metrics are computed from

$$\xi_t = -\left(\xi_x x_t + \xi_y y_t\right) \tag{4.7a}$$

$$\eta_t = -\left(\eta_x x_t + \eta_y y_t\right) \tag{4.7b}$$

An equation of state is required to close the system of equations. For an ideal gas with a constant ratio of specific heats, γ, the equation of state is written as

$$E_t = \frac{p}{\gamma - 1} + \frac{1}{2}\rho\left(u^2 + v^2\right) \tag{4.8}$$

where $\gamma = 1.4$.

4.3 Numerical Procedure

The two-stage Runge-Kutta time integration in EULER-AE uses Euler's forward difference as a predictor and the trapezoidal method as a corrector. Atkinson [29] shows this is scheme is second order accurate in time. Notationally, the integration scheme can be written as

$$\mathbf{Q}_{i,j}^{n+1} = \mathbf{Q}_{i,j}^{n} + \frac{1}{2}\frac{\Delta t_{i,j}}{\mathcal{V}_{i,j}}\left(\boldsymbol{\mathcal{R}}_{i,j}^{n} + \boldsymbol{\mathcal{R}}_{i,j}^{*}\right) \tag{4.9}$$

where $\mathcal{V}_{i,j}$ is the cell volume, $\boldsymbol{\mathcal{R}}^{\boldsymbol{n}}{}_{i,j}$ is the residual at time step n, and $\boldsymbol{\mathcal{R}}^{\boldsymbol{*}}{}_{i,j}$ is the residual obtained from the Euler prediction.

The residual $\boldsymbol{\mathcal{R}}_{i,j}$ is computed from the flux differencing Roe method [45], a first order (spatial) approximate Riemann solver. The Roe method linearizes the flux Jacobian matrices $[A]$ and $[B]$, where

$$[A] = \frac{\partial \mathbf{E}}{\partial \mathbf{Q}} \qquad\qquad [B] = \frac{\partial \mathbf{F}}{\partial \mathbf{Q}}\,, \tag{4.10}$$

by replacing these matrices with Roe averaged matrices $[\tilde{A}]$ and $[\tilde{B}]$ so that the solution to the linear problem provides an approximate solution to the nonlinear problem [44].

The averaging is based on the states to the left and right of the node being computed, e.g.

$$\mathbf{Q}_L = \mathbf{Q}_{i-1} \tag{4.11a}$$

$$\mathbf{Q}_R = \mathbf{Q}_i \tag{4.11b}$$

along a constant j line. The Roe averaged matrices are represented by the diagonal transformations

$$[\tilde{A}] = [\tilde{T}_\xi][|\tilde{\Lambda}_\xi|][\tilde{T}_\xi]^{-1} \tag{4.12a}$$

$$[\tilde{B}] = [\tilde{T}_\eta][|\tilde{\Lambda}_\eta|][\tilde{T}_\eta]^{-1} \tag{4.12b}$$

where $[\tilde{T}_\xi]$ is composed of columns of the right eigenvectors of $[\tilde{A}]$, $[\tilde{T}_\xi]^{-1}$ is composed of rows of the left eigenvectors of $[\tilde{A}]$, and $[|\tilde{\Lambda}_\xi|]$ is a diagonal matrix of the absolute values of eigenvalues of $[\tilde{A}]$. The diagonalization for $[\tilde{B}]$ is made up of similar matrices. An efficient formulation of the Roe method that pre-multiplies the transformation matrices [45] is used in EULER-AE.

The residuals are computed by summing the fluxes across the cell faces from

$$\boldsymbol{\mathcal{R}}_{i,j} = \left(\hat{\mathbf{E}}_{i+\frac{1}{2},j} - \hat{\mathbf{E}}_{i-\frac{1}{2},j}\right) + \left(\hat{\mathbf{F}}_{i,j+\frac{1}{2}} - \hat{\mathbf{F}}_{i,j-\frac{1}{2}}\right) \tag{4.13}$$

where

$$\hat{\mathbf{E}}_{i+\frac{1}{2},j} = \frac{1}{2}\left[\mathbf{E}_R + \mathbf{E}_L - [\tilde{T}_\xi][|\tilde{\Lambda}_\xi|][\tilde{T}_\xi]^{-1}(\mathbf{Q}_R - \mathbf{Q}_L)\right]_{i+\frac{1}{2},j} \tag{4.14a}$$

$$\hat{\mathbf{F}}_{i,j+\frac{1}{2}} = \frac{1}{2}\left[\mathbf{F}_R + \mathbf{F}_L - [\tilde{T}_\eta][|\tilde{\Lambda}_\eta|][\tilde{T}_\eta]^{-1}(\mathbf{Q}_R - \mathbf{Q}_L)\right]_{i,j+\frac{1}{2}} . \tag{4.14b}$$

Higher order spatial discretizations can be obtained from the monotone upstream-centered schemes for strong conservation laws (MUSCL) [44]. The MUSCL scheme ex-

trapolates left and right states from more than one neighboring node. For example

$$\mathbf{Q}_L = \mathbf{Q}_{i-1} + \frac{1-\kappa}{4}\delta\mathbf{Q}_{i-\frac{3}{2}} + \frac{1+\kappa}{4}\delta\mathbf{Q}_{i-\frac{1}{2}} \tag{4.15a}$$

$$\mathbf{Q}_R = \mathbf{Q}_i - \frac{1+\kappa}{4}\delta\mathbf{Q}_{i-\frac{1}{2}} - \frac{1-\kappa}{4}\delta\mathbf{Q}_{i+\frac{1}{2}} \tag{4.15b}$$

where δ is the central difference operator [44]. The constant κ determines the order and method of the MUSCL scheme from

$$\kappa = \begin{cases} -1 & 2^{\text{nd}} \text{ order upwind scheme} \\ 0 & 2^{\text{nd}} \text{ order Fromm's method} \\ \frac{1}{3} & 3^{\text{rd}} \text{ order upwind scheme} \\ 1 & 2^{\text{nd}} \text{ order central difference} \end{cases} \tag{4.16}$$

The third order Roe method was used throughout this investigation.

Because of the extrapolations made to obtain higher order schemes non-physical overshoots, such as negative densities, are numerically possible in regions with discontinuities, i.e. shocks. Limiters are used to prevent these overshoots by enforcing the first order Roe method in the vicinity of discontinuities. EULER-AE uses the MINMOD limiter [44] to control overshoots.

For steady state convergence, local time stepping is used as an acceleration technique. The time step $\Delta t_{i,j}$ is determined from each cell volume and local contravarient velocities from

$$\Delta t_{i,j} = \mathcal{V}_{i,j} \frac{\text{CFL}}{\frac{1}{2}[(\lambda_1)_{i,j} + (\lambda_2)_{i,j}]} \tag{4.17}$$

where

$$(\lambda_1)_{i,j} = u_{i,j}\left(\frac{\xi_x}{J}\right)_{i,j} + v_{i,j}\left(\frac{\xi_y}{J}\right)_{i,j} + a_{i,j}\sqrt{\left(\frac{\xi_x}{J}\right)^2_{i,j} + \left(\frac{\xi_y}{J}\right)^2_{i,j}} \tag{4.18a}$$

$$(\lambda_2)_{i,j} = u_{i,j}\left(\frac{\eta_x}{J}\right)_{i,j} + v_{i,j}\left(\frac{\eta_y}{J}\right)_{i,j} + a_{i,j}\sqrt{\left(\frac{\eta_x}{J}\right)^2_{i,j} + \left(\frac{\eta_y}{J}\right)^2_{i,j}} \tag{4.18b}$$

and CFL, the Courant-Friedrichs-Lewey number, is a multipication factor that is chosen to achieve the largest possible explicit time step without losing stability. For the third order Roe scheme employed, CFL = 1 was used.

A time accurate integration requires a global time step. This global time step is the minimum time step obtained from Eq. (4.17). For this study, a constant time step of $\Delta t = 0.0002$ was chosen. This was equivalent to using CFL ≈ 1.25 in Eq. (4.17).

4.4 Grid Generation

Gordnier and Melville [7] demonstrated the ability to predict LCO behavior is dependent upon the fidelity of the grid. They showed that for an inviscid solver the estimated flutter point was in better agreement with experimental data with a coarse grid rather than with a fine grid. Since boundary layer effects, such as flow separation and turbulence, cannot be modeled by an inviscid code, the shock is predicted in the wrong location. A high order spatial integration on a fine grid results in the shock being sharply refined at this wrong location, leading to errors in the lift and moment coefficients. While grid refinement was an issue near the leading edge of the NACA 64A006 airfoil due to the small leading edge radius, the grid was allowed to be coarser towards the trailing edge in order to spread (or weaken) the shock over a larger area.

The ordinates for the NACA 64A006 airfoil are shown in Table 4.1 [46, 47]. In order to construct the airfoil, a cubic spline of the ordinates was merged to the leading edge radius. The trailing edge was pinched down so that the trailing edge radius was zero. This was necessary since the inviscid code cannot handle the flow separation induced by the small trailing edge radius. The change in geometry is minor and should not have a significant effect on the aerodynamics.

A 257×65 point C-grid was constructed from the airfoil geometry. A cut line was defined from the airfoil trailing edge to the the far field boundary. Along the $j = 1$ line,

Table 4.1 Ordinates for the NACA 64A006 Airfoil[a]

x	y	x	y
0.0000	0.00000	0.2000	0.02557
0.0005	0.00158	0.2500	0.02757
0.0010	0.00221	0.3000	0.02896
0.0015	0.00270	0.3500	0.02977
0.0020	0.00311	0.4000	0.02999
0.0025	0.00347	0.4500	0.02945
0.0030	0.00379	0.5000	0.02825
0.0035	0.00409	0.5500	0.02653
0.0040	0.00435	0.6000	0.02438
0.0050	0.00485	0.6500	0.02188
0.0075	0.00585	0.7000	0.01907
0.0125	0.00739	0.7500	0.01602
0.0250	0.01016	0.8000	0.01285
0.0500	0.01399	0.8500	0.00967
0.0750	0.01684	0.9000	0.00649
0.1000	0.01919	0.9500	0.00331
0.1500	0.02283	1.0000	0.00013[b]

[a]L.E. radius 0.00246, T.E. radius 0.00014
[b]This y-ordinate was changed to 0.00000

the cut line and airfoil surface are given by

$$i = \begin{cases} 1 - 65 & \text{cut line} \\ 65 - 129 & \text{airfoil lower surface} \\ 129 - 193 & \text{airfoil upper surface} \\ 193 - 257 & \text{cut line} \end{cases} \tag{4.19}$$

The leading edge radius required fine spacing to reduce pressure oscillations seen in a coarser grid. The initial spacing on the leading edge was 0.00025 chords and the spacing was allowed to increase slowly as the curvature decreased. The grid spacing was coarsest near the midpoint of the airfoil and then became more finely spaced near the trailing edge to accommodate flow field gradients in this region. The final grid point spacing at the trailing edge was approximately 0.01 chords. The radial spacing was chosen

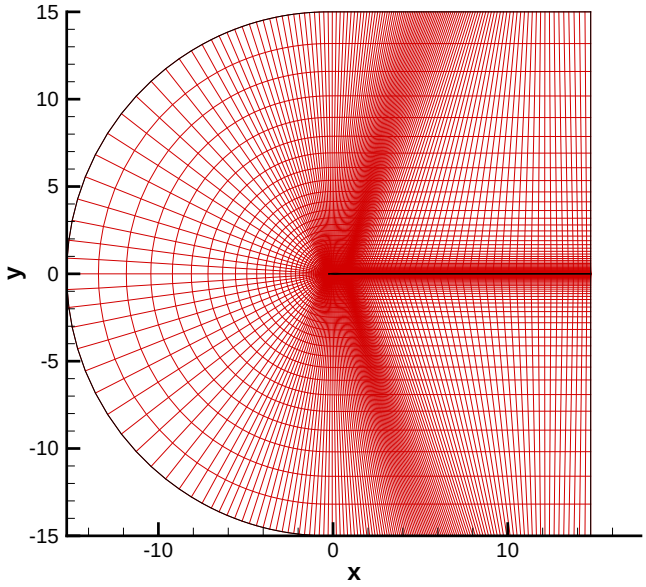

Figure 4.2 NACA64A006 structured grid - far field

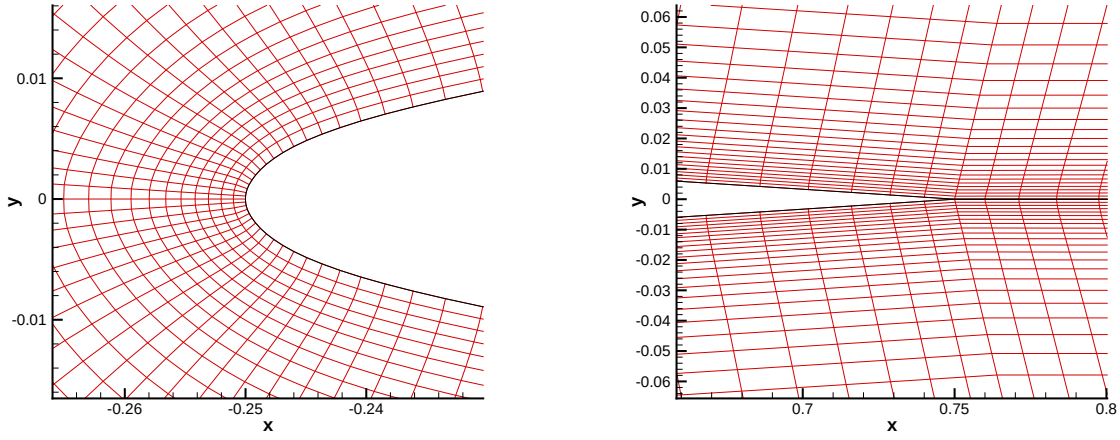

(a) **Leading edge** (b) **Trailing edge**

Figure 4.3 NACA64A006 structured grid - detail

to minimize cell aspect ratio near the leading edge without becoming so fine as to be considered a viscous mesh. The initial grid spacing off the wall was 0.001 chords and spacing exponentially increased out to fifteen chord lengths.

Two control points were defined approximately 10° forward and aft of the airfoil on the far field boundary. Grid points were redistributed between these control points until the algebraic grid was nearly orthogonal to the airfoil surface. An elliptic solver was then run on the subdomain defined by the first forty grid points off the wall and the cut line to further improve orthogonality. The resulting grid is shown in Figure 4.2. A close-up of the grid near the leading and trailing edges is shown in Figure 4.3.

4.5 Boundary Conditions

The boundary conditions consist of three types – solid wall (impermeable surface), far field (inflow or outflow), and a cut. The following first order formulation comes primarily from Whitfield and Janus [48] with modifications to include the fluxes induced by the rigid body motion of the grid. Since the flow solver is node centered, the metrics of transformation at the nodes are computed with standard finite difference techniques (see Tannehill et al. [44]).

The inviscid, solid wall boundary condition requires the flow to remain tangential to the wall. For a general airfoil geometry, the tangential flow is obtained by computing the unit normals at each node from the metrics of transformation, i.e.

$$\hat{n}_x = \frac{\eta_x}{\sqrt{\eta_x^2 + \eta_y^2}} \tag{4.20a}$$

$$\hat{n}_y = \frac{\eta_y}{\sqrt{\eta_x^2 + \eta_y^2}} \,. \tag{4.20b}$$

The tangential velocities at the solid wall are then given by

$$u_{wall} = u - U\hat{n}_x \tag{4.21a}$$

$$v_{wall} = v - U\hat{n}_y \,. \tag{4.21b}$$

Both the pressure and density gradients were assumed to be zero at the wall [43]. Thus p_{wall} and ρ_{wall} were set to the same values as those one grid point off the wall. The total energy at the wall was computed from the ideal gas equation of state, Eq. (4.8).

The subsonic far field boundary conditions depends upon whether the flow is in to or out of the computational domain. The standard unit normal direction is defined to point into the computational domain. This direction is in the same direction (sign = 1) as the unit normal determined from the metrics of transformation for the $i = 1$ and $j = 1$ faces, and in the opposite direction (sign $= -1$) for the $i = i_{\max}$ and $j = j_{\max}$ faces. Thus, when sign $\times U > 0$, the flow is in to the computational domain, and when sign $\times U < 0$ the flow is out of the computational domain.

For a subsonic inflow, three of the characteristic variables are determined from the free stream conditions, but the fourth must be determined from the computational domain. For a subsonic outflow, two of the characteristic variables must be determined from the computational domain while the third is determined from the free stream conditions [44]. Whitfield and Janus [48] relate these characteristic variables back to the primitive variables. For subsonic inflow the boundary conditions are given by

$$\rho_{\text{in}} = \rho_\infty \tag{4.22a}$$

$$p_{\text{in}} = \frac{1}{2}\left(p_\infty + p_{\text{ref}} + \text{sign}\,\rho_{\text{ref}} a_{\text{ref}} \left\{n_x \left[u_\infty - (u_{\text{ref}} - x_t)\right] + n_y \left[v_\infty - (v_{\text{ref}} - y_t)\right]\right\}\right) \tag{4.22b}$$

$$u_{\text{in}} = u_\infty + \text{sign}\, n_x \frac{p_\infty - p_{\text{ref}}}{\rho_{\text{ref}} a_{\text{ref}}} \tag{4.22c}$$

$$v_{\text{in}} = v_\infty + \text{sign}\, n_y \frac{p_\infty - p_{\text{ref}}}{\rho_{\text{ref}} a_{\text{ref}}} \tag{4.22d}$$

where the reference values (p_{ref}, ρ_{ref}, etc.) are obtained from the first interior node. The subsonic outflow boundary conditions are given by

$$p_{\text{out}} = p_\infty \tag{4.23a}$$

$$\rho_{\text{out}} = \rho_{\text{ref}} + \frac{p_\infty - p_{\text{ref}}}{a_{\text{ref}}^2} \tag{4.23b}$$

$$u_{\text{out}} = u_{\text{ref}} + \text{sign}\, n_x \frac{p_\infty - p_{\text{ref}}}{\rho_{\text{ref}} a_{\text{ref}}} \tag{4.23c}$$

$$v_{\text{out}} = v_{\text{ref}} + \text{sign}\, n_y \frac{p_\infty - p_{\text{ref}}}{\rho_{\text{ref}} a_{\text{ref}}} \tag{4.23d}$$

In both cases, the total energy was computed from the ideal gas equation of state.

The boundary condition employed along the cut line of the C-grid was a simple average. For example

$$p_{1,j} = \frac{1}{2}(p_{2,j} + p_{i_{\max}-1,j}) \tag{4.24}$$

Lift and Moment Computations

The lift and moment coefficients, assuming unit span, are given by

$$C_l = -\oint_{\text{airfoil}} p \, \mathrm{d}A_y \tag{4.25a}$$

$$C_m = \oint_{\text{airfoil}} p \, (x \, \mathrm{d}A_y - y \, \mathrm{d}A_x) \tag{4.25b}$$

These equations were derived assuming the grid underwent rigid body motion and the moment was taken about the origin. The minus sign in the coefficient of lift equation ensures that lift is positive up. The moment coefficient is measured positive nose up. The components of the area vector normal to the airfoil surface are given by

$$\mathrm{d}A_x = \frac{\eta_x}{J} \tag{4.26a}$$

$$\mathrm{d}A_y = \frac{\eta_y}{J} \; . \tag{4.26b}$$

By a straightforward application of the trapezoidal rule, the lift and moment coefficients were computed from

$$C_l = -p_{i_{c1},1} \left(\frac{\eta_y}{J}\right)_{i_{c1},1} - 2 \sum_{i=i_{c1}+1}^{i_{c2}-1} \left[p_{i,1} \left(\frac{\eta_y}{J}\right)_{i,1} \right] - p_{i_{c2},1} \left(\frac{\eta_y}{J}\right)_{i_{c2},1} \tag{4.27a}$$

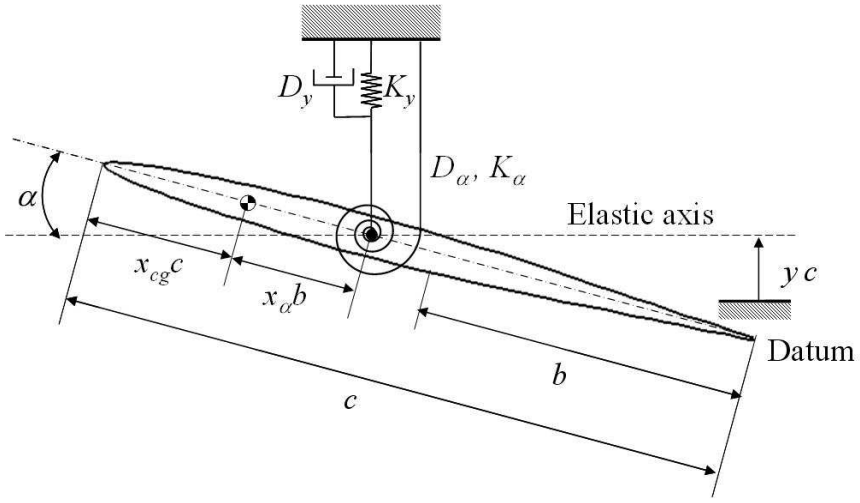

Figure 4.4 Notation for the Pitch and Plunge Airfoil used in EULER-AE

and

$$C_m = p_{i_{c1},1}\left[x_{i_{c1},1}\left(\frac{\eta_y}{J}\right)_{i_{c1},1} - y_{i_{c1},1}\left(\frac{\eta_x}{J}\right)_{i_{c1},1}\right] + 2\sum_{i=i_{c1}+1}^{i_{c2}-1}\left\{p_{i,1}\left[x_{i,1}\left(\frac{\eta_y}{J}\right)_{i,1} - y_{i,1}\left(\frac{\eta_x}{J}\right)_{i,1}\right]\right\} + p_{i_{c2},1}\left[x_{i_{c2},1}\left(\frac{\eta_y}{J}\right)_{i_{c2},1} - y_{i_{c2},1}\left(\frac{\eta_x}{J}\right)_{i_{c2},1}\right] . \tag{4.27b}$$

The indices i_{c1} and i_{c2} are located on the trailing edge of the airfoil, where $i_{c1} = 65$ and $i_{c2} = 193$.

4.6 Aeroelastic Equations of Motion

The equations of motion for the airfoil differ slightly from those presented in Sec. 2.2. The nomenclature shown in Figure 4.4 was used by Morton and Beran [34] and was also used in the development of EULER-AE. Viscous dampers are now included in both the pitch and plunge axes. They are modeled by [34]

$$D_\alpha = 2\zeta_\alpha m r_\alpha^2 b^2 \omega_\alpha \tag{4.28a}$$

$$D_h = 2\zeta_y m \omega_h \tag{4.28b}$$

The location of the center of gravity is measured from the airfoil leading edge and is scaled by the airfoil chord. Plunge is measured positive up and is also scaled by the airfoil chord. Additionally, the nondimensionalization for reduced velocity is given by

$$V_r = \frac{V_\infty}{\omega_\alpha c} \tag{4.29}$$

and the time t is given in Eq. (4.1). Cubic and quintic nonlinear responses are still assumed for the pitch spring. With the above assumptions and the remaining nondimensional parameters given in Sec. 2.2, the equations of motion become

$$\ddot{y} + \frac{x_\alpha}{2}\ddot{\alpha} + 4\zeta_y \frac{\omega_r}{V_r}\dot{y} + 4\left(\frac{\omega_r}{V_r}\right)^2 y = \frac{2}{\mu_s \pi} C_l \tag{4.30a}$$

$$x_\alpha \ddot{y} + \frac{r_\alpha^2}{2}\ddot{\alpha} + 2\zeta_\alpha \frac{r_\alpha^2}{V_r}\dot{\alpha} + 2\frac{r_\alpha^2}{V_r^2}\left(\alpha + \beta_\alpha \alpha^3 + \gamma_\alpha \alpha^5\right) = \frac{4}{\mu_s \pi} C_m \, . \tag{4.30b}$$

By letting

$$\mathbf{S} = \begin{pmatrix} s_1 \\ s_2 \\ s_3 \\ s_4 \end{pmatrix} = \begin{pmatrix} \alpha \\ \dot{\alpha} \\ y \\ \dot{y} \end{pmatrix} \tag{4.31}$$

the equations of motion can be written in the compact notation

$$[M]\dot{\mathbf{S}} + [K_1]\mathbf{S} + [K_3]\mathbf{S}^3 + [K_5]\mathbf{S}^5 = \mathbf{G} \tag{4.32}$$

where the mass matrix is

$$[M] = \begin{bmatrix} 1 & 0 & 0 & 0 \\ 0 & \frac{x_\alpha}{2} & 0 & 1 \\ 0 & 0 & 1 & 0 \\ 0 & \frac{r_\alpha^2}{2} & 0 & x_\alpha \end{bmatrix} , \tag{4.33a}$$

the linear stiffness matrix is

$$[K_1] = \begin{bmatrix} 0 & -1 & 0 & 0 \\ 0 & 0 & 4\left(\frac{\omega_r}{V_r}\right)^2 & 4\zeta_y\frac{\omega_r}{V_r} \\ 0 & 0 & 0 & -1 \\ \frac{r_\alpha^2}{V_r^2} & 2\zeta_\alpha\frac{r_\alpha^2}{V_r} & 0 & 0 \end{bmatrix}, \tag{4.33b}$$

the nonlinear stiffness matrices are

$$[K_3] = \begin{bmatrix} 0 & 0 & 0 & 0 \\ 0 & 0 & 0 & 0 \\ 0 & 0 & 0 & 0 \\ 2\frac{r_\alpha^2}{V_r^2}\beta_\alpha & 0 & 0 & 0 \end{bmatrix} \qquad [K_5] = \begin{bmatrix} 0 & 0 & 0 & 0 \\ 0 & 0 & 0 & 0 \\ 0 & 0 & 0 & 0 \\ 2\frac{r_\alpha^2}{V_r^2}\gamma_\alpha & 0 & 0 & 0 \end{bmatrix} \tag{4.33c}$$

and the aerodynamic forcing term is

$$\mathbf{G} = \begin{pmatrix} 0 \\ f \\ 0 \\ g \end{pmatrix} = \begin{pmatrix} 0 \\ \frac{2}{\mu_s\pi}C_l \\ 0 \\ \frac{4}{\mu_s\pi}C_m \end{pmatrix}. \tag{4.33d}$$

Solving for $\dot{\mathbf{S}}$ yields

$$\dot{\mathbf{S}} = [M]^{-1}\left(\mathbf{G} - [K_1]\mathbf{S} - [K_3]\mathbf{S}^3 - [K_5]\mathbf{S}^5\right) \tag{4.34}$$

which fully expanded becomes

$$\begin{pmatrix} \dot{s_1} \\ \dot{s_2} \\ \dot{s_3} \\ \dot{s_4} \end{pmatrix} = \begin{pmatrix} s_2 \\ \frac{2}{r_\alpha^2 - x_\alpha^2}\left[g_1 - x_\alpha f_1\right] \\ s_3 \\ \frac{1}{r_\alpha^2 - x_\alpha^2}\left[r_\alpha^2 f_1 - x_\alpha g_1\right] \end{pmatrix} \tag{4.35}$$

where

$$f_1 = f - 4\left(\frac{\omega_r}{V_r}\right)^2 s_3 - 4\zeta_y \frac{\omega_r}{V_r} s_4 \tag{4.36a}$$

$$g_1 = g - 2\frac{r_\alpha^2}{V_r^2}\left(s_1 + \beta_\alpha s_1^3 + \gamma_\alpha s_1^5\right) - 2\zeta_\alpha \frac{r_\alpha^2}{V_r} s_2 \ . \tag{4.36b}$$

Equation (4.35) is integrated explicitly in time by the two-stage Runge-Kutta method already described.

4.7 Rigid Body Motion

At each step in time, the grid is translated and rotated with respect to the elastic axis, where the elastic axis is initially placed at the origin. Defining

$$\Delta\alpha = \alpha^n - \alpha^{n-1} \tag{4.37a}$$

$$\Delta y = y^n - y^{n-1} \tag{4.37b}$$

the translation is accomplished by

$$y^* = y^{n-1} + \Delta y \tag{4.38}$$

and the rotation by

$$\begin{pmatrix} x^n \\ y^n \end{pmatrix} = \begin{bmatrix} \cos(\Delta\alpha) & \sin(\Delta\alpha) \\ -\sin(\Delta\alpha) & \cos(\Delta\alpha) \end{bmatrix} \begin{pmatrix} x^{n-1} \\ y^* \end{pmatrix} \ . \tag{4.39}$$

The transformation metrics are unaffected by the translation, but must be rotated by the same rotation matrix in Eq. (4.39) in order for the area vectors to remain normal to the cell faces.

4.8 Sample Cases

Two static cases and an LCO case are presented as validation of the research code. The static cases are compared with results from FLUENT™ and with experimental data [42]. The first case was run at $M_\infty = 0.86$ and $\alpha = 0$ and the second case was run at $M_\infty = 0.85$ and $\alpha = 4°$. The resulting pressure distributions are shown in Figure 4.5. Both EULER-AE and FLUENT™ are in very good agreement with one another. The predicted shock locations are one cell different between the two codes. This is probably due to EULER-AE being run with a third order spacial scheme, while FLUENT™ is limited to a second order scheme. The difference in order of spatial discretization also explains why the shock is more sharply defined with EULER-AE. As expected, the inviscid shocks are stronger and further aft on the wing than the experimental data, especially at large angles of attack (Figure 4.5(b)). This will lead to a prediction of a much larger lift

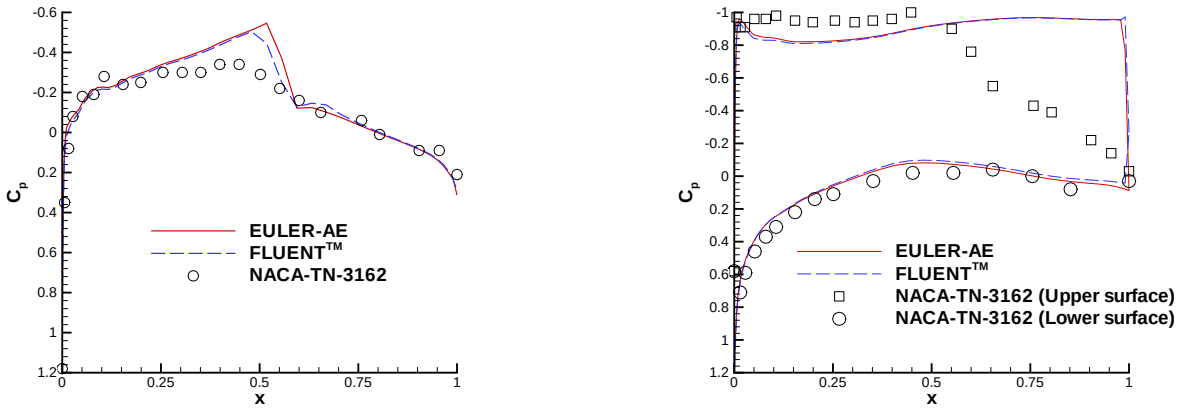

(a) $M_\infty = 0.86$, $\alpha = 0$ (b) $M_\infty = 0.85$, $\alpha = 4°$

Figure 4.5 Pressure distributions on the NACA 64A006 airfoil

coefficient for the inviscid cases. While comparison with the experimental data is only fair, due to the lack of viscous and turbulence modeling, the code to code comparison with FLUENT™ indicates that EULER-AE properly predicts an inviscid flow over the airfoil.

The time accurate fluid-structure interaction was verified by comparing with an LCO prediction given by Morton and Beran [34]. A complete validation was not possible due to the different formulations of EULER-AE and Morton and Beran [34]. EULER-AE employs a matched point analysis whereas the method of Morton and Beran [34] employs a non-matched point analysis. A matched point analysis ensures the reduced velocity, freestream air density and freestream Mach number are consistent with standard atmospheric conditions [49]. A given density and Mach number implies a freestream velocity which in turn implies the values of the viscous dampers and spring constants, as shown in Eqs. (4.29) and (4.30). Thus, the amplitude and frequency of the coupled response from a matched point and non-matched point analysis will not necessarily be the same (see Appendix A).

Morton and Beran [34] use the following parameters to obtain an LCO from the NACA 64A006 airfoil with linear pitch ($\beta_\alpha = \gamma_\alpha = 0$) and plunge springs.

$$\begin{array}{lll} x_{cg} = 0.375 & x_\alpha = -0.25 & r_\alpha^2 = 0.25 \\ M_\infty = 0.85 & \mu_s = 125 & \omega_r = 0.2 \\ \zeta_y = 0.5 & \zeta_\alpha = 0.5 & \end{array} \tag{4.40}$$

At a reduced velocity of $V_r = 11$ and standard sea level conditions ($p_\infty = 101325$ N/m^2 and $\rho_\infty = 1.225$ kg/m^3), EULER-AE predicts the pitch and plunge LCOs shown in Figure 4.6. Table 4.2 shows the differences between the results from EULER-AE and Morton and Beran [34]. The shorter period from EULER-AE indicates that the pitch spring stiffness for the aeroelastic system is greater than that from Morton and Beran [34]. However, the larger amplitudes in pitch and, especially, plunge indicate just the

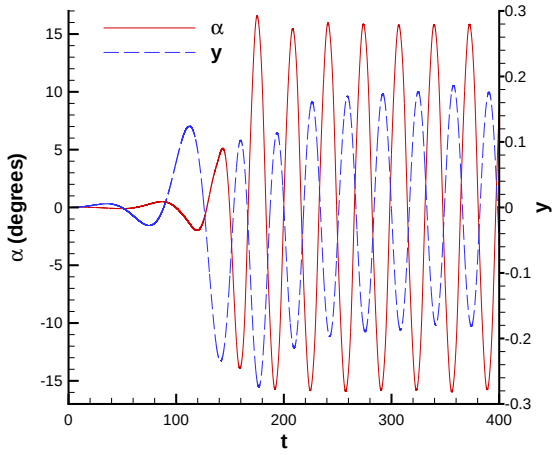

Figure 4.6 LCO at $V_r = 11.0$

Table 4.2 Differences between LCOs from EULER-AE and Morton and Beran [34]

	α_{LCO}	y_{LCO}	Period	Flutter Point
EULER-AE	15.8°	0.176	32.9	6.78
Reference [34]	13.0°	0.020	61.6	10.28

opposite. The reason for the apparent discrepancy, as will demonstrated in the next chapter, is the flutter point for the matched point aeroelastic system is located at a much lower reduced velocity ($V_r \approx 6.78$) than that of the non-matched point aeroelastic system ($V_r = 10.28$).

4.9 Summary

An inviscid aeroelastic code has been developed to investigate the response of a nonlinear airfoil. The equations and numerical procedures used by the code EULER-AE were described. Sample solutions to verify and validate the numerical procedures were presented. In the next chapter, this code is used to determine the effects of initial condition and parametric uncertainty on the nonlinear NACA 64A006 airfoil.

V. A CFD Application of the Stochastic Projection Method via B-Splines

5.1 Introduction

A typical aeroelastic simulation performed by EULER-AE took approximately 36 to 48 hours to reach a fully developed LCO, making the MCS approach to determining PDFs of a response impractical. The stochastic algorithm developed in Chapter III was applied to this CFD application to determine the subcritical response of the NACA 64A006 airfoil. The subcritical case was examined since LCOs can be obtained below the classically defined flutter point.

To produce a subcritical response with a turning point, such as the one shown in Figure 2.6, nonlinear structural parameters were chosen for the NACA 64A006 airfoil. Care was taken to choose parameters such that pitch and plunge excursions were still valid in the context of an Euler code, i. e. small amplitude LCOs. With the parameters chosen, the flutter point, turning point, and bifurcation diagram were estimated from numerous computational runs. To demonstrate the utility of the stochastic algorithm in estimating PDFs and probabilities of failure in this CFD application, a single reduced velocity below the flutter point was examined ($V_r = 6.5$). Probability density functions of the LCO amplitude in both pitch, α_{LCO}, and plunge, y_{LCO}, and of the coupled frequency of the response, ω_{LCO}, estimated from the stochastic projection method via B-splines are presented. Refined B-spline surfaces are also presented to demonstrate convergence of the PDFs and thus provide a validation of the stochastic algorithm.

5.2 Bifurcation Diagram of the Aeroelastic System

Development of the bifurcation diagram begins with an estimation of the flutter point. Recall from Sec. 2.4 that the flutter point is a loss of linear stability and its location is unaffected by the nonlinear parameters. Gordnier and Melville [7] efficiently estimate the flutter point of an aeroelastic system by first computing a few cycles at reduced

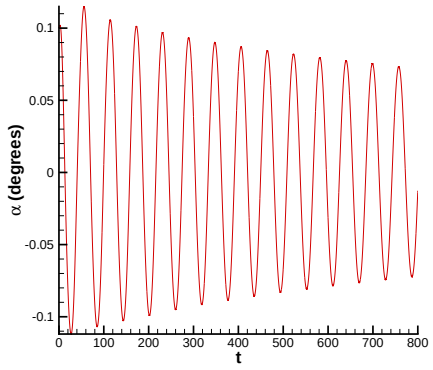

(a) $V_r = 6.7$

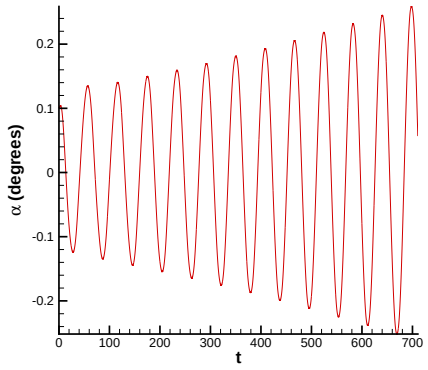

(b) $V_r = 6.9$

Figure 5.1 Examples of the pitch response

velocities above and below the flutter point and then comparing amplitude factors as the cycles either increase or decrease. The amplitude factor is defined as the ratio of the peak magnitude with the magnitude of the previous peak with the same sign (i.e., one period) [7]. The parameters given in Eq. (4.40) with $\beta_\alpha = \gamma_\alpha = 0$ provide a supercritical response from which the flutter point can be estimated. With an initial pitch of $\alpha(0) = 0.1°$, cases were run at reduced velocities of $V_r = 6.6$, 6.7, 6.8, 6.9, and 7.0. Examples of the different pitch responses are shown in Figure 5.1. Note that the amplitudes are of such small magnitudes that any nonlinear restoring forces would be completely unimportant, i.e. $\alpha^3, \alpha^5 \ll 0$. An average of the last few amplification factors for each of the responses results in the plot show in Figure 5.2. From Figure 5.2 the flutter point is estimated to occur at $V_r \approx 6.78$.

Once the flutter point was determined, nonlinear parameters were selected to produce a subcritical response with a turning point. Following the model problem, a cubic spring constant of $\beta_\alpha < 0$ was chosen to destabilize the aeroelastic system below the flutter point. The goal was to choose a β_α such that the aeroelastic system was destabilized at a small initial pitch angle. Numerical experimentation led to a value of $\beta_\alpha = -30$, which caused the aeroelastic system to become unstable with $\alpha(0) \approx 3°$ at a reduced

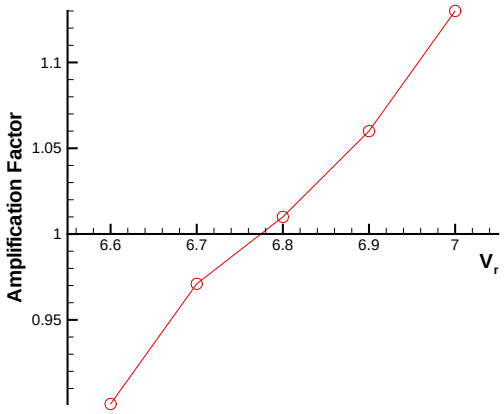

Figure 5.2 Flutter point estimation

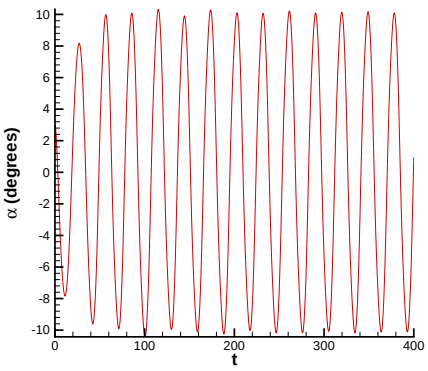

Figure 5.3 LCO due to a subcritical response, $V_r = 6.5$, $\alpha(0) = 3°$, $\beta_\alpha = -30$, $\gamma_\alpha = 500$

velocity of $V_r = 6.5$. The quintic spring constant γ_α was then chosen to restabilize the system. Again through numerical experimentation, a value of $\gamma_\alpha = 500$ was selected. This value resulted in an LCO at $V_r = 6.5$ with an initial pitch angle of $\alpha(0) = 3°$, as shown in Figure 5.3. For clarity, the parameters of the aeroelastic system are presented again. The structural parameters, with the inclusion of the nonlinear spring constants,

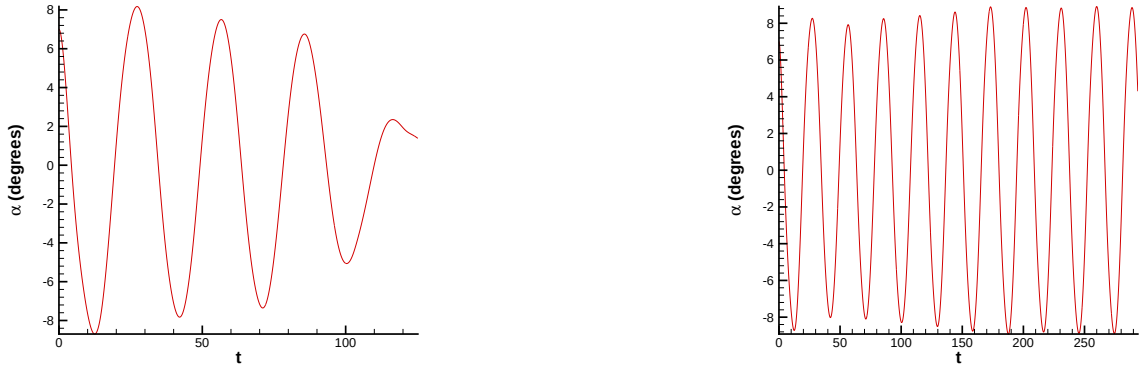

(a) $V_r = 6.105$, $\alpha(0) = 7°$ (b) $V_r = 6.115$, $\alpha(0) = 7°$

Figure 5.4 Identification of the turning point

are

$$\begin{array}{lll} x_{cg} = 0.375 & x_\alpha = -0.25 & r_\alpha^2 = 0.25 \\ \mu_s = 125 & \zeta_y = 0.5 & \zeta_\alpha = 0.5 \\ \omega_r = 0.2 & \beta_\alpha = -30 & \gamma_\alpha = 500\ , \end{array} \tag{5.1}$$

and the aerodynamic parameters are

$$p_\infty = 37612\ \text{N/m}^2 \qquad \rho_\infty = 0.5489\ \text{kg/m}^3 \qquad M_\infty = 0.85 \tag{5.2}$$

The freestream pressure and density correspond to an altitude of 25,000 ft.

With the parameters chosen, numerous computer runs were conducted on a range of reduced velocities at and below the flutter point to map out the subcritical bifurcation. In each case a sufficiently large initial pitch angle of $\alpha(0) = 7°$ was chosen to ensure the aeroelastic system would exhibit LCO. It was found that the system would rapidly exhibit LCO or rapidly proceed to a stationary response near the turning point, as shown in Figure 5.4. The turning point was estimated at $V_r \approx 6.11$. The resulting bifurcation diagram is shown in Figure 5.5.

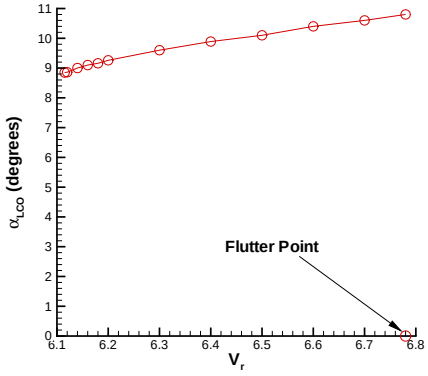

Figure 5.5 Bifurcation diagram for the nonlinear aeroelastic system

5.3 Uncertainty Quantification

As with the model problem, an initial condition uncertainty and a parametric uncertainty were added to the formulation. A Gaussian distribution in the uncertainties was assumed. These uncertainties are, as before, given by

$$\alpha(0) = \bar{\alpha}(0) + \xi_1 \tilde{\alpha}(0) \tag{5.3a}$$

$$\beta_\alpha = \bar{\beta}_\alpha + \xi_2 \tilde{\beta}_\alpha \tag{5.3b}$$

For this aeroelastic system, the following mean and standard deviation values were used

$$\bar{\alpha}(0) = 0 \qquad \bar{\beta}_\alpha = -30 \tag{5.4a}$$

$$\tilde{\alpha}(0) = 1.5^\circ \qquad \tilde{\beta}_\alpha = 3 \tag{5.4b}$$

Samples of the responses in pitch, plunge, and frequency were obtained at the nodes given in Table 3.1 at a reduced velocity of $V_r = 6.5$. The following is a summary of the results.

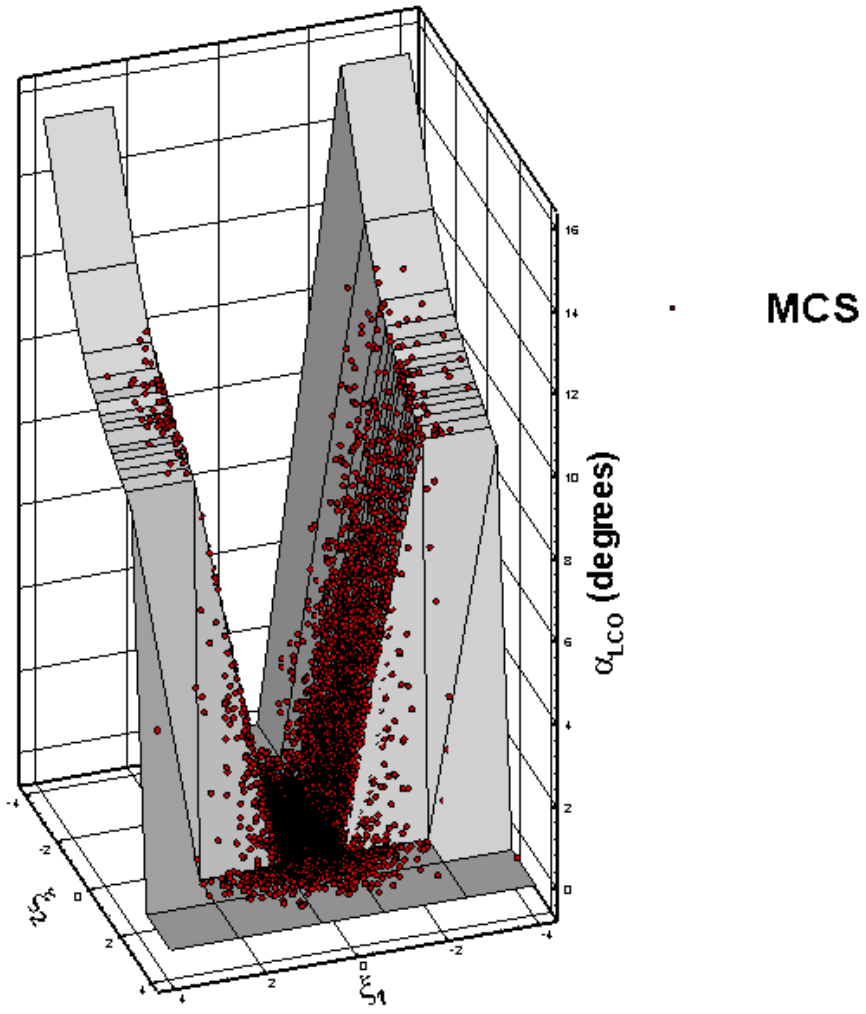

Figure 5.6 B-spline surfaces of the pitch response ($I = 2$, $J = 8$)

$I = 2$, $J = 2, 4, 8$

The effect of increasing resolution on the ξ_2 axis (uncertainty in the cubic spring constant) as the resolution on the ξ_1 axis (uncertainty in the initial pitch angle) remained fixed was investigated first. Each simulation was carried out to $t_{\max} \approx 500$ or until the LCO became fully developed. A fully developed LCO was considered achieved when two successive amplitudes, α_{LCO}, were within 0.1° of each other. The samples obtained from the simulations were used to build the B-spline (piecewise linear) surfaces from Eq. (3.3). An example of the resulting surfaces is shown in Figure 5.6.

Immediately of note from the B-spline surface in Figure 5.6 is that, as in the model problem, the symmetric airfoil and the zero mean initial pitch angle lead to symmetry on the ξ_1 axis. Also, if an LCO develops for a given set of structural parameters, the amplitude of the LCO is the same regardless of the initial pitch angle. These two properties of the B-spline surface for this aeroelastic system can lead to a reduction in both the number and the computational effort of simulations as the resolution increases in either axis. It will be noted later in the discussion when these properties were invoked.

A bifurcation is observed on the ξ_2 axis. This bifurcation occurs between $\xi_2 = 1.53415$ and $\xi_2 = 2.5$. This corresponds to $\beta_\alpha = -25.398$ and $\beta_\alpha = -22.5$, respectively. Thus, as the overall pitch spring stiffness becomes greater, i.e. less destabilization from the cubic spring constant, LCO will not develop for any initial pitch angle. This is an example of how uncertainty in the structural components has an effect on the LCO of an aeroelastic system.

Also shown on Figure 5.6 are the results of a 10,000 MCS obtained from the B-spline surface. (Note: ten thousand randomly generated Gaussian variables can occasionally, although rarely, exceed the interval $[-4, 4]$. When this occurred, the value of that random variable was mapped to the closest boundary.) As expected, the MCS samples are concentrated near the zero means. Since the discontinuities associated with the bifurcations are not sharply resolved, many realizations fall on values intermediate to the stationary response and the LCO response. The effect of these intermediate values can be seen in the PDFs of the response shown in Figure 5.7. Since the bulk of intermediate values are a result of the poor resolution in the ξ_1 axis, increasing resolution in the ξ_2 axis had little effect on the the convergence of the PDF of the pitch response. A very close examination reveals that with $J = 4$ and $J = 8$ the PDFs are essentially identical. Further investigation of the uncertainty quantification is, therefore, continued holding the resolution in the ξ_2 axis fixed at $J = 4$.

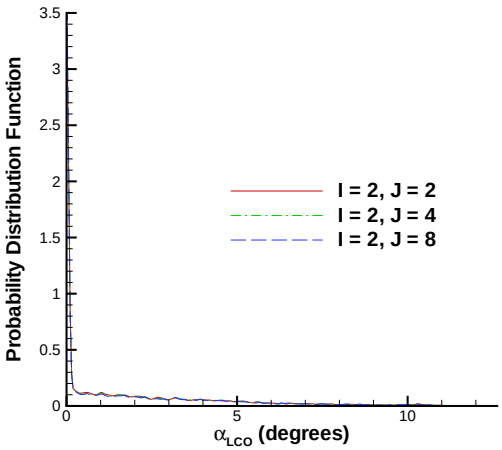

(a) **PDFs of the pitch response**

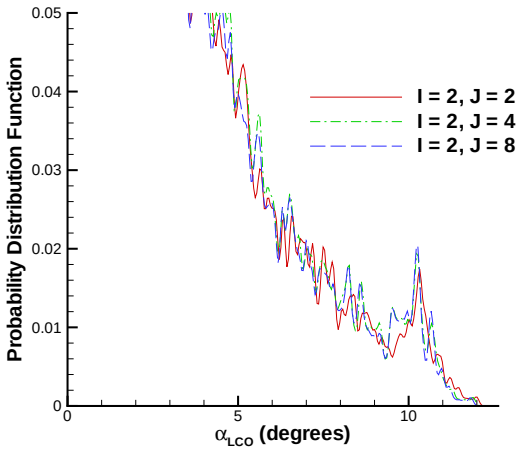

(b) **Close up of PDFs of the pitch response**

Figure 5.7 Pitch Response

I = 2, 4, 8; J = 4

Having examined the stochastic response surface with increasing resolution along the ξ_2 axis, simulations were then performed with increasing resolution on the ξ_1 axis. Since the amplitudes of the LCOs were already known from the previous set of simulations, these simulations were carried out just far enough in time ($t_{\max} < 250$) to determine if an LCO was developing or if the response was damped. Examples of the resulting B-spline surfaces are shown in Figure 5.8. Note that as the resolution increases, the discontinuity is more sharply refined. This refinement leads to fewer realizations intermediate to the LCO and the stationary responses.

As expected, fewer intermediate realizations leads to a better convergence for the PDFs of the response, as shown in Figure 5.9. With each increase in resolution, the PDFs show fewer intermediate realizations while at the same time an area near $\alpha_{LCO} \approx 10°$ remains unchanged. Note that from Figure 5.5, the mean responses at $V_r = 6.5$ is $\alpha_{LCO} = 10.1°$. Thus, from these simulations, it is estimated that a bimodal response exists with the primary response at $\alpha_{LCO} = 0$ and the secondary response at $\alpha_{LCO} = 10°$.

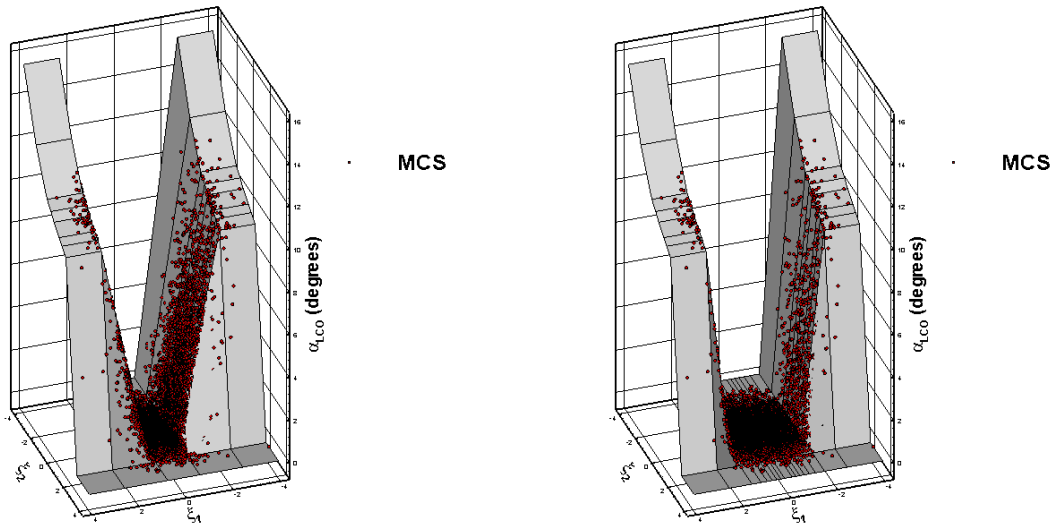

(a) $I = 2,\ J = 4$ (b) $I = 8,\ J = 4$

Figure 5.8 B-spline surfaces of the pitch response (α_{LCO})

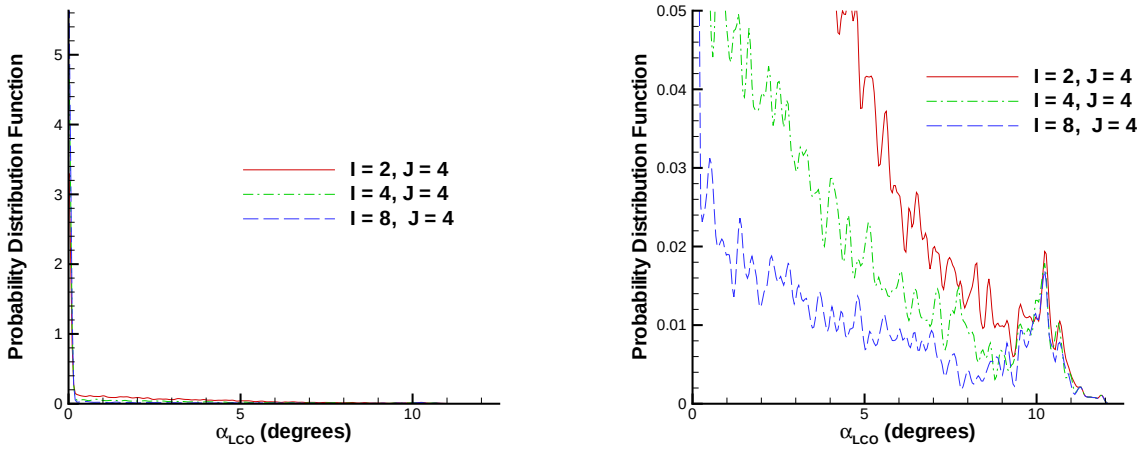

(a) **PDFs of the pitch response**

(b) **Close up of PDFs of the pitch response**

Figure 5.9 Pitch Response

Additionally, the uncertainty bounds for the secondary response are estimated to be from $\alpha_{LCO} = 9°$ to $\alpha_{LCO} = 12°$. The subcritical response and the uncertainty bounds were identified with a sample size of 180 simulations.

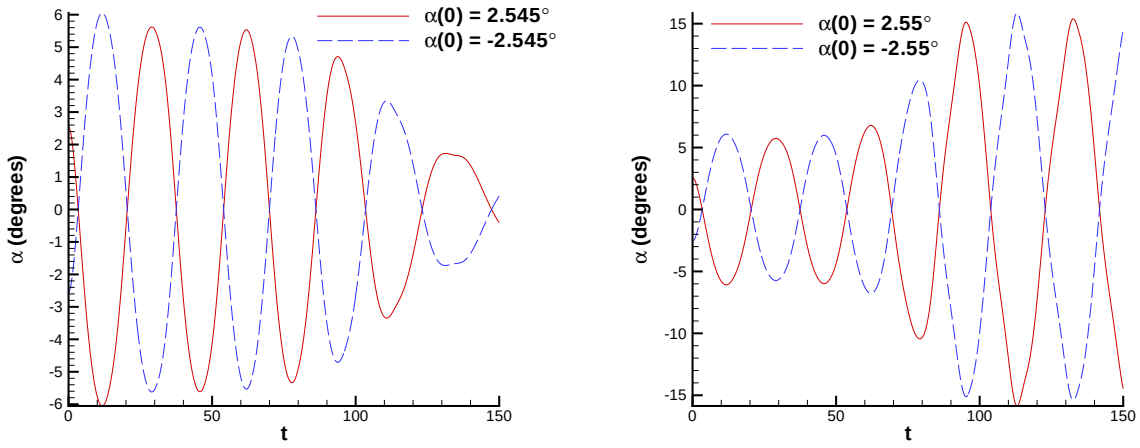

(a) **Damped response** (b) **LCO response**

Figure 5.10 Symmetric responses with $\beta_\alpha = -42$, ($\xi_2 = -4$)

5.4 Refined B-spline surface

A better estimate of the subcritical response can easily be obtained by making use of the information already gained. The locations of the bifurcations have been bounded and can be better refined with a simple binary search. Further validation of this method can also be shown by refining the B-spline surface at a different set of nodes. Thus the nodes chosen along the ξ_2 axis were uniformly spaced until reaching the bifurcation while the nodes along the ξ_1 were selected to refine the bifurcations on that axis. Additionally, only the positive half of the ξ_1 axis was investigated and symmetry was assumed on the negative half of the axis. A few simulations were conducted to verify this symmetry, such as the ones shown in Figure 5.10. With the above assumptions, approximately one hundred simulations were performed to obtain the nodes for the refined B-spline shown in Table 5.1. Since the nodes no longer compose a regular mesh, the multivariate B-spline approach is difficult to implement. The 10,000 run MCS is accomplished by a simple linear interpolation scheme, which is equivalent to a piecewise linear approximation of the second order B-spline [30]. A comparison of the B-spline surface obtained with $I = 8$ and $J = 4$ with the refined B-spline surface and the associated MCS realizations is shown

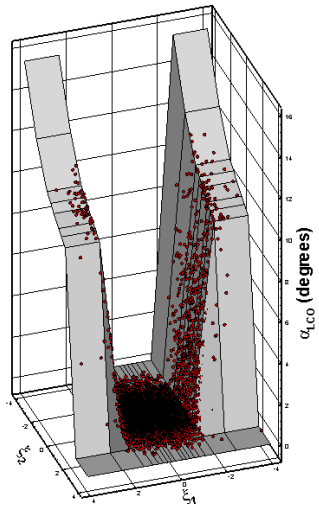

(a) **B-spline surface from the Gaussian nodes ($I = 8$, $J = 4$)**

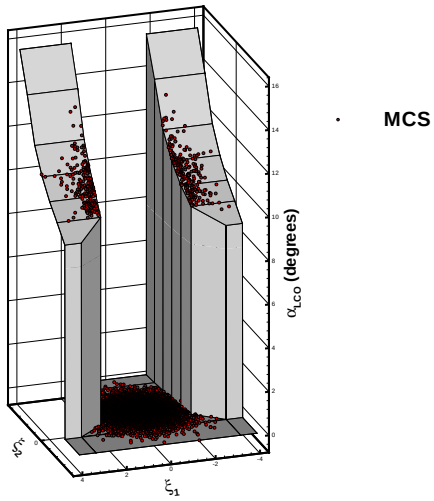

(b) **Refined B-spline surface**

Figure 5.11 Pitch Response

Table 5.1 Nodes for the refined B-spline surface

ξ_1	ξ_2	α_{LCO}	ξ_1	ξ_2	α_{LCO}	ξ_1	ξ_2	α_{LCO}
-4	-4	15.6°	-4	-1	10.9°	-4	2.03333	8.89°
-1.7		15.6°	-1.83667		10.9°	-3.26		8.89°
-1.69667		0	-1.83333		0	-3.25667		0
1.69667		0	1.83333		0	3.25667		0
1.7		15.6°	1.83667		10.9°	3.26		8.89°
4		15.6°	4		10.9°	4		8.89°
-4	-3	13.9°	-4	0	10.1°	-4	2.06666	0
-1.73		13.9°	-1.91667		10.1°	-3.26		0
-1.72667		0	-1.91333		0	-3.25667		0
1.72667		0	1.91333		0	3.25667		0
1.73		13.9°	1.91667		10.1°	3.26		0
4		13.9°	4		10.1°	4		0
-4	-2	12.0°	-4	1	9.53°	-4	4	0
-1.78		12.0°	-2.04		9.53°	-3.26		0
-1.77667		0	-2.03667		0	-3.25667		0
1.77667		0	2.03667		0	3.25667		0
1.78		12.0°	2.04		9.53°	3.26		0
4		12.0°	4		9.53°	4		0

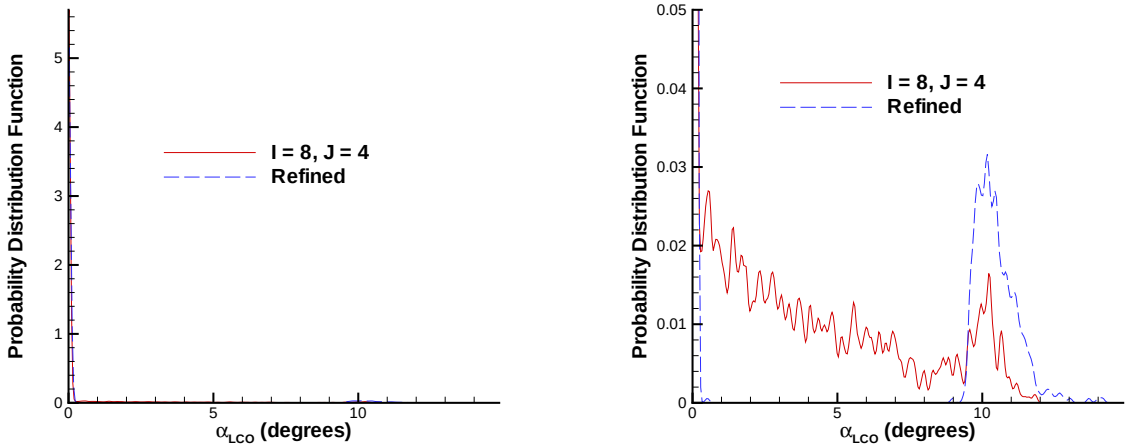

(a) **PDFs of the pitch response**

(b) **Close up of PDFs of the pitch response**

Figure 5.12 Convergence of the pitch subcritical response

in Figure 5.11. A PDF of the pitch response obtained from the refined B-spline surface is seen to achieve convergence in Figure 5.12, where the intermediate values between the stationary response and the LCO response are practically non-existent.

Plunge and Coupled Frequency

The same uncertainty analysis was investigated for the plunge LCO amplitude and the coupled frequency. B-spline surfaces of the plunge LCO amplitude, y_{LCO}, and the coupled frequency, ω_{LCO} were developed for the $I = 8$ and $J = 4$ Gaussian nodes and for the refined nodes. These surfaces are shown in Figures 5.13 and 5.14. Convergence of the PDFs for these responses is shown in Figures 5.15 and 5.16.

5.5 Probability of Failure

The PDFs of the LCO responses allow an estimate the probability of failure for the aeroelastic system. As with the model problem, criteria need to be chosen that define the failure mode. Recalling that the subcritical LCO response develops below the flutter

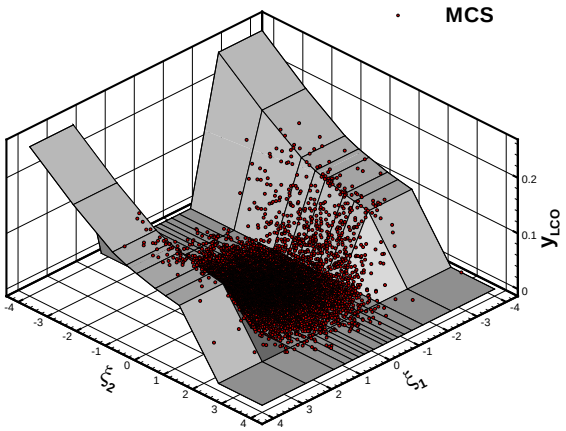

(a) **B-spline surface from the Gaussian nodes ($I = 8$, $J = 4$)**

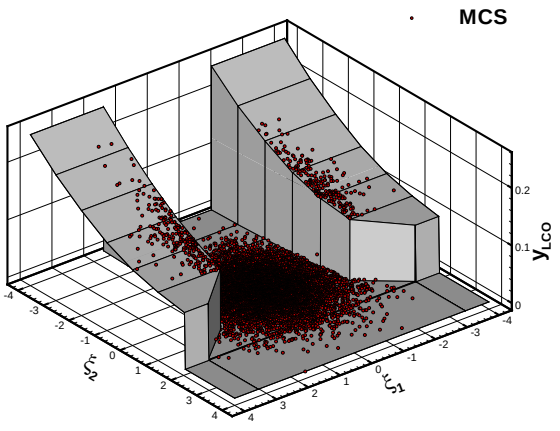

(b) **Refined B-spline surface**

Figure 5.13 Plunge Response

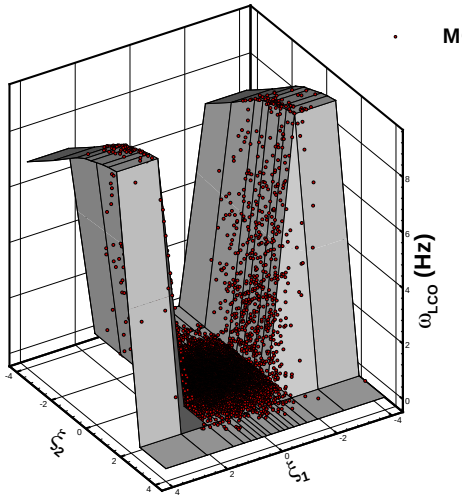

(a) **B-spline surface from the Gaussian nodes ($I = 8$, $J = 4$)**

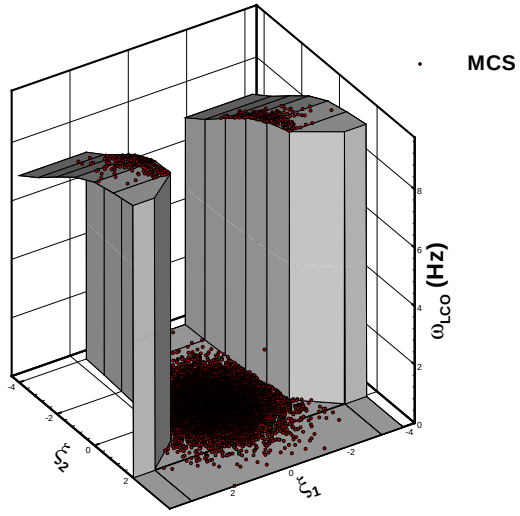

(b) **Refined B-spline surface**

Figure 5.14 Frequency Response

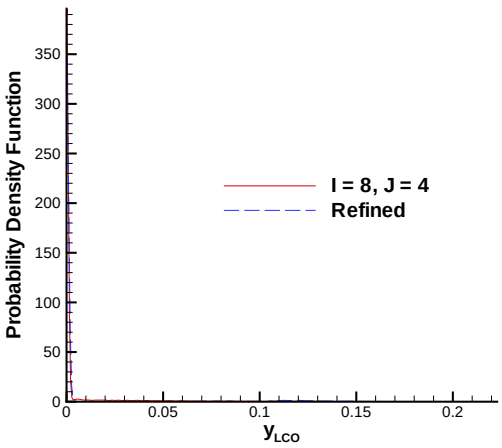

(a) **PDFs of the plunge response**

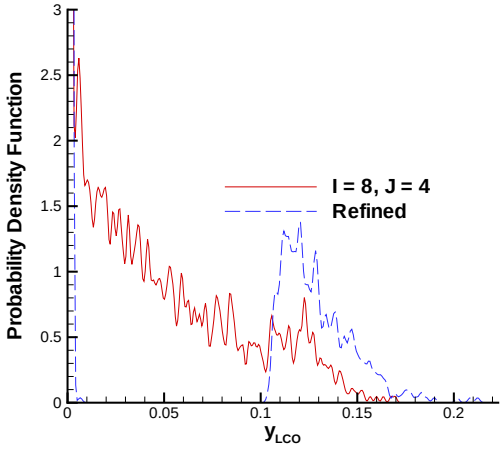

(b) **Close up of PDFs of the plunge response**

Figure 5.15 Convergence of the plunge subcritical response

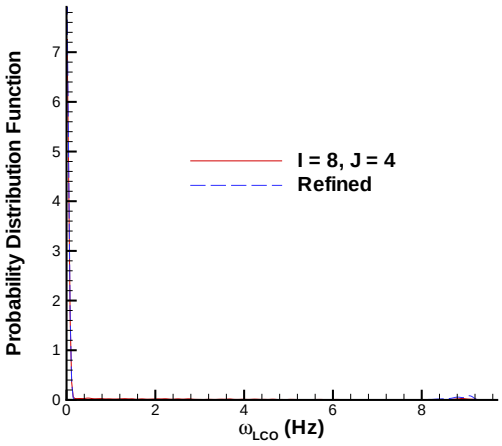

(a) **PDFs of the plunge response**

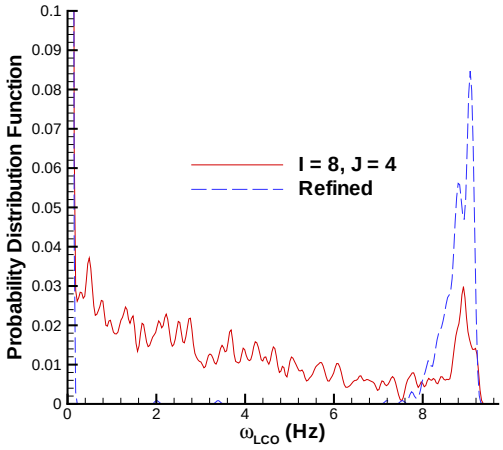

(b) **Close up of PDFs of the plunge response**

Figure 5.16 Convergence of the frequency subcritical response

point, failure is defined as the onset of an LCO. In order to perform the integration of the PDFs, and to avoid the smoothing error inherent in the Parzen windowing approach, failure in each mode (pitch, plunge, and frequency) were set at

$$\alpha_{\text{fail}} = 1^\circ \tag{5.5a}$$

$$y_{\text{fail}} = 0.01 \tag{5.5b}$$

$$\omega_{\text{fail}} = 1 \text{ Hz} \tag{5.5c}$$

With these failure modes defined, the probability of failure was estimated from the PDFs obtained from the Gaussian nodes as well as from the refined nodes. The results are summarized in Table 5.2. As resolution increases, the estimation of the probability of failure improves until, at the refined surface, all three probability of failures converge to the same value. The convergence of all three probabilities of failure to the same value is an expected result since the three events (pitch, plunge, and frequency) are not independent of each other. If the aeroelastic system experiences a pitch (plunge) LCO, it must also exhibit a plunge (pitch) LCO, and these LCOs will occur at some frequency. Due to the numerous realizations at the intermediate values, the Gaussian nodes provide a conservative estimate of the probability of failure while the refined nodes provides an estimate comparable to a full-order MCS. The total number of actual simulations performed, however, are two orders of magnitude less than that of a 10,000 run MCS.

Table 5.2 Estimates of the Probability of Failure

	Probability of Failure (%)		
Nodes	Pitch	Plunge	Frequency
$I = 2$, $J = 4$	38.1	39.7	36.9
$I = 4$, $J = 4$	19.6	20.3	18.9
$I = 8$, $J = 4$	10.3	10.6	10.1
Refined	4.36	4.36	4.36

5.6 Summary

This chapter demonstrated the efficiency of the stochastic projection method via B-splines in estimating the probability of failure for a CFD application of an aeroelastic system. The structure was a low fidelity, two degree of freedom, nonlinear airfoil modeled in a higher fidelity inviscid transonic flow. The number of simulations actually performed was two orders of magnitude less than a full order MCS. Verification of the stochastic algorithm was demonstrated by the convergence of the PDFs to a subcritical response.

VI. Summary and Conclusions

6.1 Summary

A stochastic algorithm based upon the PCE and FCE stochastic projection methods was developed by employing multivariate B-splines. This method is a nonintrusive (sampling approach) that does not require the computation or storage of expected values to estimate the stochastic projection of the response. Instead, the B-spline approach is a collocation method that fits a surface to the nodes provided. The nodes were selected both by a Gaussian distribution as well as a uniform distribution of probabilities.

An aeroelastic model problem was first investigated by a traditional Monte Carlo approach. Bifurcation diagrams, PDFs, and probabilities of failure were provided for comparison with the stochastic algorithm. The computational effort for this model problem was shown to be quite large.

A small sample set based upon a Gaussian distribution of probabilities was then obtained. A B-spline surface was developed from which a fast MCS could be performed. Although the LCOs developed were due to initial conditions and large time integrations, the sampling approach removes the samples from the time domain by tracking the LCO amplitude once the LCO is fully devloped. Results from the stochastic algorithm were in excellent agreement with the traditional MCS approach. Additionally, the stochastic algorithm was two orders of magnitude more efficient than the MCS approach.

The applicability of the stochastic algorithm was investigated for the more computationally demanding CFD simulation of an aeroelastic system. An inviscid aeroelastic code (EULER-AE) was developed, verified, and validated to perform this investigation. Parameters were selected to obtain a subcritical response with a turning point. This response is considered high risk since large amplitude LCOs can develop below the classically defined flutter point. Monte Carlo simulations were impractical for this problem since each simulation took 36 to 48 hours to perform. Validity of the stochastic projection method via B-splines was determined by convergence of the PDFs and the probability

of failure. Again, efficiency was two orders of magnitude greater than that of the Monte Carlo approach, making this stochastic algorithm applicable to large time, CFD applications.

6.2 Conclusions

Based upon this research effort, the following conclusions were reached:

1. *For large time and highly nonlinear problems, nonintrusive (sampling) methods are more efficient than intrusive methods.* This point was alluded to in the introduction. For large time problems, the frequency content in the stochastic domain at any particular time can become so large, or contain so many discontinuities, that even a basis that might be considered optimal would require such a high order expansion that all computational efficiency is lost.
2. *Bifurcations are represented by discontinuities in the stochastic domain, making spectral approaches inefficient.* When the spectral approach is recognized as an attempt to approximate a global response surface, its limitations are the same as in any interpolation problem. An infinite expansion is required to sharply define a discontinuity.
3. *Efficiency can be regained by distribution based sampling and approximating the global response surface with a multivariate B-spline.* Splines are the most appropriate method for approximating a peicewise continuous function in any interpolation problem. The selection of nodes should initially be based on the distribution of input uncertainty. Refinement comes once information is obtained from an initial set of simulations.
4. *The stochastic projection method via B-splines is applicable to CFD based research.* Uncertainty quantification is an expensive proposition. As CFD codes become faster due to improvements of algorithms and processor power, the ability to conduct multiple simulations, though not at the level of a full-order MCS, moves into

the realm of possibilities. The stochastic algorithm presented here makes uncertainty quantification possible at the current level of processor power.

6.3 Recommendations for Future Research

The stochastic algorithm was applied to an inviscid, transonic aeroelastic problem. The next step in the study of aeroelastic responses would be to include viscous fluxes, turbulence modeling, and eventually a three dimensional configuration. Since the method is nonintrusive, any research or commercial code could be used to conduct this investigation.

Future research with the stochastic algorithm should include:

1. *The inclusion of higher order multivariate splines* The piecewise linear interpolation was nearly optimal for the two dimensional aeroelastic system. This will not always be the case. Indeed, for the projection with respect to ξ_2, Figures 3.2(b) and 5.11(b), a higher order interpolation would provide a better fit than the piecewise linear interpolation. However, the bifurcation in Figure 5.11(b) produces overshoots with higher order B-splines. The Akima spline [30] is shape preserving and may be more appropriate for this type of projection.
2. *Determination of the maximum number of uncertainties that can be included in the algorithm.* The number of simulations increases geometrically if the same number of nodes are used in each dimension of uncertainty. Thus, there is a practical limit to the number of uncertainties that can be modeled before the computational effort reaches that of a Monte Carlo simulation. Investigating each dimension individually and determining the maximum nodes required before moving to the next dimension, as was done with the CFD application, can lead to an algebraic increase in effort as dimensions are added.
3. *Multiple distributions of uncertainties.* In the CFD application, both Gaussian nodes and uniformly spaced nodes were used to build the B-spline surface. This

is an indication that, unlike other stochastic projection methods, the distribution of uncertainties do not need to be homogeneous among the random variables. The intervals and nodes can be selected based upon the individual distribution of the random variables.

4. *Automation.* Once the Gaussian nodes were computed, an interactive approach was employed to refine the sampling mesh. Automating this process would be a major undertaking but could provide a great value to the aircraft designer.

5. *Dimensional Analysis* It was demonstrated that different LCO solutions were obtained from the matched and non-matched point assumptions. The proper nondimensional parameters for the fluid-structure coupling should be determined.

References

1. Fung, Y.C. *An Introduction to Aeroelasticity*. New York: Dover Pubilications, Inc., 1969.

2. Bunton, Robert W. and Charles M. Denegri. "Limit Cycle Oscillation Characteristics of Fighter Aircraft," *Journal of Aircraft*, *37*(5):916–918 (September-October 2000).

3. Lee, B.H.K. and L.Y. Jiang and Y.S. Wong, "Flutter of an Airfoil with a Cubic Nonlinear Restoring Force." AIAA-98-1725, SDM Conference, 1998.

4. Matsushita, Hiroshi and Kenichi Saitoh and Péter Gránásy, "Wind Tunnel Investigation of Transonic Limit Cycle Oscillation." AIAA-98-1728, April, 1998.

5. Tang, L. and R.E. Bartels and P.C. Chen and D.D. Liu, "Simulation of Transonic Limit Cycle Oscillation using a CFD Time Marching Method." AIAA-2001-1292, 42nd AIAA/ASME/ASCE/AHS/ASC Structures, Structural Dynamics, and Materials Conference, Seattle, WA, April 16-19, 2001.

6. Beran, P.S., "Computation of Limit Cycle Oscillation Using a Direct Method." AIAA-99-1462, 40th AIAA/ASCE/AHS/ASC Structures, Structural Dynamics, and Materials Conference, St. Louis, MO, April 12-15, 1999.

7. Gordnier, Raymond E. and Reid B. Melville. "Transonic Flutter Simulations Using an Implicit Solver," *Jounal of Aircraft*, *37*(5):872–879 (September–October 2000).

8. Beran, Philip S. and Chris L. Pettit, "A Direct Method for Quantifying Limit Cycle Oscillation Response Characteristics in the Presence of Uncertainties." AIAA 2004-1695, 45th AIAA/ASME/ASCE/AHS/ASC Structures, Structural Dynamics, and Materials Conference, Palm Springs, CA, April 19–22, 2004.

9. Grigoriu, Mircea. *Stochastic Calculus: Applications in Science and Engineering*. Boston: Birkhäuser, 2002.

10. Beran, P. and W. Silva, "Reduced Order Modeling: New Approaches to Computational Physics." AIAA-2001-0853, 39th Aerospace Sciences Meeting and Exhibit, Reno, NV, January 8-11, 2001.

11. Beran, Philip S. and Chris L. Pettit, "Prediction of Nonlinear Panel Response Using Proper Orthogonal Decomposition." AIAA-2001-1292, 42nd AIAA/ASME/ASCE/AHS/ASC Structures, Structural Dynamics, and Materials Conference, Seattle, WA, April 16-19, 2001.

12. Beran, P.S. and C.L. Pettit, "Reduced-Order Modeling for Flutter Prediction." AIAA-2000-1446-CP, 2000.

13. Wiener, Norbert. "The Homogeneous Chaos," *American Journal of Mathematics*, *60*:897–936 (1938).

14. Cameron, R.H. and W.T. Martin. "The Orthogonal Development of Nonlinear Functionals in Series of Fourier-Hermite Functionals," *Annals of Mathematics*, *48*:385–392 (1947).

15. Ghanem, Roger G. and Pol D. Spanos. *Stochastic Finite Element Methods: A Spectral Approach*. Springer-Verlag, 1991.

16. Ghanem, Roger. "A Comparative Analysis of FORM/SORM and Polynomial Chaos Expansions for Highly Nonlinear Systems." *Engineering Mechanics: Proceedings of the 11th Conference1*, edited by Y.K. Lin and D. Ghiocel. 535–538. New York: American Society of Civil Engineers, 1996.

17. Li, R. and R. Ghanem. "Adaptive Polynomial Chaos Expansions Applied to Statistics of Extremes in Non-Linear Random Vibration," *Probabilistic Engineering Mechanics*, *13*(2):125–136 (1997).

18. Le Maître, Oliver P. and Omar M. Knio and Habib N. Najm and Roger G. Ghanem. "A Stochasitc Projection Method for Fluid Flow," *Journal of Computational Physics*, *173*(2):481–511 (2001).

19. Xiu, Dongbin and George Em Karniadakis. "Modeling Uncertainty in Flow Simulations via Generalized Polynomial Chaos," *Journal of Computational Physics*, *187*(1):137–168 (May 2003).

20. Xiu, Dongbin and Didier Lucor and C.-H. Su and George Em Karniadakis. "Stochastic Modeling of Flow-Structure Interactions Using Generalized Polynomial Chaos," *Journal of Fluids Engineering*, *124*:51–58 (March 2002).

21. Xiu, Dongbin and George Em Karniadakis. "Modeling Uncertainty in Steady State Diffusion Problems via Generalized Polynomial Chaos," *Computational Methods in Applied Mechanics*, *191*(43):4927–4948 (2002).

22. Chorin, Alexandre Joel. "Guassian Fields and Random Flows," *Journal of Fluid Mechanics*, *63*(1):21–32 (1974).

23. Crow, S. C. and G. H. Canavan. "Relationship between a Wiener-Hermite Expansion and an Energy Cascade," *Journal of Fluid Mechanics*, *41*:387–403 (1970).

24. Millman, D. R. and P. I. King and P. S. Beran, "A Stochastic Approach for Predicting Bifurcation of a Pitch and Plunge Airfoil." AIAA 2003-3515, 21st AIAA Applied Aerodynamics Conference, Orlando, FL, June 23–26, June 23–26, 2003.

25. Millman, D.R. and P.I. King and P.S. Beran. "Airfoil Pitch and Plunge Bifurcation Behavior with Fourier Chaos Expansions," *AIAA Journal* (to appear 2004).

26. Pettit, Chris L. and Philip S. Beran, "Polynomial Chaos Expansion Applied to Airfoil Limit Cycle Oscillations." AIAA 2004-1695, 45th AIAA/ASME/ASCE/AHS/ASC Structures, Structural Dynamics, and Materials Conference, Palm Springs, CA, April 19–22, 2004.

27. Myers, Raymond H. and Douglas C. Montgomery. *Response Surface Methodology: Process and Product Optimization using Designed Experiments*. New York: John Wiley and Sons, 1995.

28. Mathelin, Lionel and M. Yousuff Hussaini. *A Stochastic Collocation Algorithm for Uncertainty Analysis*. Technical Report, NASA/CR-2003-212153, 2003.

29. Atkinson, Kendall E. *An Introduction to Numerical Analysis* (2 Edition). New York: John Wiley and Sons, Inc., 1989.

30. de Boor, Carl. *A Practical Guide to Splines* (Revised Edition). New York: Springer-Verlag, 2001.

31. Millman, Daniel R. and Paul I. KIng and Raymond C. Maple and Philip S. Beran, "Predicting Uncertainty Propogation in a Highly Nonlinear System with a Stochastic Projection Method." 45th AIAA/ASME/ASCE/AHS/ASC Structures, Structural Dynamics, and Materials Conference, Palm Springs, CA, April 19–22, 2004.

32. Seydel, Rùdiger. *From Equilibrium to Chaos: Practical Bifurcation and Stability*. New York: Elsevier Science Publishing Co., Inc, 1988.

33. Hodges, Dewey H. and G. Alvin Pierce. *Introduction to Structural Dynamics and Aeroelasticity*. Cambridge: Cambridge University Press, 2002.

34. Morton, S.A. and P.S. Beran. "Hopf-Bifurcation Analysis of Airfoil Flutter at Transonic Speeds," *Journal of Aricraft*, *36*(2):421–429 (March–April 1999).

35. Jones, R.T. *The Unsteady Lift of a Wing with Finite Aspect Ratio*. Technical Report, NACA Report 681, 1940.

36. Duda, Richard O. and Peter E. Hart and David G. Stork. *Pattern Classification* (2 Edition). New York: John Wiley and Sons, Inc., 2001.

37. Sobol, Illia Meerovich. *The Monte Carlo Method* (2 Edition). Moscow: Mir Publishers, 1984.

38. Ghanem, R. and P.D. Spanos. "A Stochastic Galerkin Expansion for Nonlinear Random Vibration Analysis," *Probabilistic Engineering Mechanics*, *8*:255–264 (1993).

39. Thomas, Jeffery P. and Earl H. Dowell and Kenneth C. Hall. "Nonlinear, Inviscid Aerodynamic Effects on Transonic Divergence, Flutter, and Limit Cycle Oscillation," *AIAA Journal*, *40*(4):638–646 (April 2002).

40. Kousen, Kenneth A. and Oddvar O. Bendiksen, "Nonlinear Aspects of the Transonic Aeroelastic Stability Problem." AIAA 88-2306, 29th AIAA Structures, Structural Dynamics and Materials Conference, Williamsburg, VA, April 18–20 1988.

41. Alonso, J.J. and A. Jameson, "Fully-Implicit Time-Marching Aeroelastic Solutions." AIAA-94-0056, 32nd Aerospace Sciences Meeting and Exhibit, January 10–13 1994.

42. Stivers, Loius S. Jr. *Effects of Subsonic Mach Number on the Forces and Pressure Distributions on Four NACA 64A-Series Airfoil Sections at Angles of Attack as High as* 28°. Technical Report, NACA-TN-3162, 1954.

43. Hoffmann, Klaus A. and Steve T. Chiang. *Computational Fluid Dynamics, Vol. II, 4th ed.*. Engineering Education System, 2000.

44. Tannehill, John C. and Dale A. Anderson and Richard H. Pletcher. *Computational Fluid Mechanics and Heat Transfer, 2nd ed.*. Taylor and Francis, 1997.

45. Krist, S.L. and R.T. Bierdon and C.L. Rumsey. *CFL3D User's Manual*. Technical Report, NASA/TM-1998-208444, 1998.

46. Bland, S.R., "AGARD Two Dimensional Aeroelastic Configurations." AGARD Report 156, 1979.

47. Abbott, Ira H. and Albert E. von Doenhoff. *Theory of Wing Sections, Incluing a Summary of Airfoil Data* (Revised Edition). New York: Dover Pubilications, Inc., 1959.

48. Whitfield, D.L. and J.M. Janus, "Three-Dimensional Unsteady Euler Equations Solution Using Flux Vector Splitting." AIAA-84-1552, AIAA 17th Fluid Dynamics, Plasma Dynamics, and Lasers Conference, Snowmass, CO, June 25–27, 1984.

49. Bhatia, Kumar G. *A Computer Program for Automated Flutter Solution and Matched Point Determination*. Technical Report, NASA TM-X-2846, 1973.

50. Bhatia, Kumar G., "An Automated Method for Determining the Flutter Velocity and the Matched Point." AIAA Paper 73-195, AIAA 11th Aerospace Sciences Meeting, Washington, D.C., January 10–12 1973.

51. Kim, Taeyoun and Moeljo Hong and Kumar G. Bhatia and Gautam Sengupta, "AIAA-2004-2040, Aeroelastic Model Reduction for an Affordable CFD Based Flutter Analysis, Palm Springs, CA." Add data for field: HowPublished, April 19–22 2004.

Appendix A. Coupling of the Nondimensional Parameters

As early as 1973 [50] and as recently as 2004 [51] it has been recognized that if Mach number is specified when solving an aeroelastic system, compatibility should be enforced between freestream Mach number, freestream density, and the reduced velocity. This compatibility is referred to as a matched point analysis. Other researchers [34, 40] prefer a non-matched point solution where only the nondimensional parameters are specified and it is assumed that a similarity solution which conforms to a matched point solution exists. It will be shown that both approaches have limitations that exist due to the coupling of the fluid and structure.

A straightforward dimensional analysis of the Euler equations leads to the nondimensional parameters shown in Eq. (4.1). Of particular note is the nondimensionalization of the farfield boundary condition (here the asterisk indicates a nondimensional quantity)

$$\rho_\infty^* = 1 \tag{A.1a}$$

$$u_\infty^* = \cos\alpha \tag{A.1b}$$

$$v_\infty^* = \sin\alpha \tag{A.1c}$$

$$p_\infty^* = \frac{1}{\gamma M_\infty^2} \tag{A.1d}$$

Thus, a properly nondimensionalized Euler code only requires the freestream Mach number and angle of attack to compute, say, a pressure distribution over an airfoil. The resulting solution is a similarity solution for any two given thermodynamic quantities, say pressure (p_∞) and density (ρ_∞).

A similar dimensional analysis can be performed on the pitch and plunge airfoil equations with modeled aerodynamics, Eq. (2.1). Lift and moment are scaled by the

dynamic pressure and chord, that is

$$L = \frac{1}{2}\rho_\infty V_\infty^2 c\, C_l(t) \tag{A.2a}$$

$$M = \frac{1}{2}\rho_\infty V_\infty^2 c^2 C_m(t) \tag{A.2b}$$

It is important to recognize that for the modeled aerodynamics, the lift and moment coefficients are functions only of time and the flow is assumed incompressible. Thus, the nondimensionalization that leads to the reduced velocity (V_r), frequency ratio (ω_r), and mass ratio (μ_s) provide a similarity solution for any given dynamic pressure (ρ_∞ and V_∞) and structural parameters (m, ω_α, ω_h, x_α, and r_α).

When coupling the Euler equations to the structural equations, a coupling also occurs in the nondimensional parameters. The reduced velocity, for example, is given by (for convenience, all lengths in this section are scaled by the chord c)

$$V_r = \frac{V_\infty}{\omega_\alpha c} \tag{A.3}$$

Typically the reduced velocity is taken as a free parameter in the structural problem, but it will be shown that for the coupled fluid-structure problem the reduced velocity should instead be derived from the remaining system parameters.

To demonstrate this assertion, consider the definition of Mach number

$$M_\infty \equiv \frac{V_\infty}{a_\infty} \tag{A.4}$$

where a_∞ is the freestream speed of sound and is given by

$$a_\infty = \sqrt{\gamma \frac{p_\infty}{\rho_\infty}}\,. \tag{A.5}$$

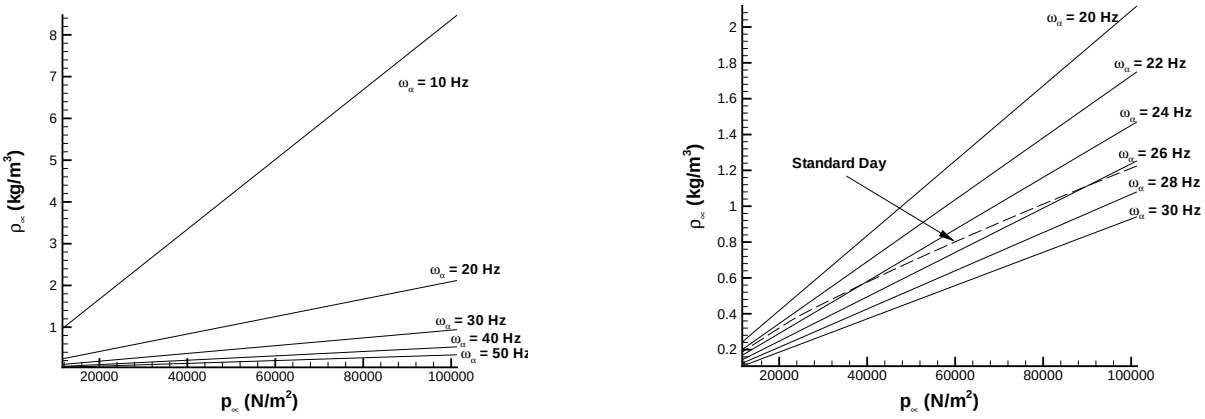

(a) **Matching density with remaining parameters**

(b) **Comparison with standard day**

Figure A.1 Density determined by varying ω_α and p_∞

The reduced velocity is then rewritten as

$$V_r = \frac{M_\infty}{\omega_\alpha c}\sqrt{\gamma\frac{p_\infty}{\rho_\infty}}\ . \tag{A.6}$$

Rearranging terms to solve for freestream density yields

$$\rho_\infty = \frac{\gamma p_\infty M_\infty^2}{\omega_\alpha^2 c^2 V_r^2} \tag{A.7}$$

Equation (A.7) shows that for a given Mach number and reduced velocity the freestream density is a function of freestream pressure (a fluid parameter) and of the uncoupled natural frequency in pitch (a structural parameter). The implications of this relationship between fluid and structure parameters is shown in Figure A.1. To obtain these results, the Mach number was selected as $M_\infty = 0.85$ and the reduced velocity as $V_r = 11$. The freestream pressure was allowed to vary with altitude according to standard day tables and the uncoupled natural frequency in pitch was allowed to vary from $\omega_\alpha = 10$ to $\omega_\alpha = 50$. Figure A.1(a) shows the large variation obtained in density, particularly near sea level pressure. These results are typical of a non-matched point analysis where

only the nondimensional parameters (to include Mach number and reduced velocity) are specified. In order to obtain the solution for $\omega_\alpha = 10Hz$ at sea level pressure, density is on the order of 8 kg/m^3, an unrealistic value for air. Even at low pressures, $p_\infty \approx 20000$ N/m^2 (approximately 40,000 ft pressure altitude), density varies from greater than sea level values ($\rho_\infty \approx 1.67$ kg/m^3) to approximately 70,000 ft density altitude. In contrast, a matched point solution specifies a pressure and density that vary with a standard day. Figure A.1(b) shows where the standard day pressure and density lie with comparison to the non-matched point data. Note that the matched point solution allows only a small range of possible structural parameters. One point is clearly evident from Figures A.1(a) and (b), i.e., the matched point and non-matched point parameters will not necessarily provide the same solution.

The above analysis indicates similarity solutions for a general structure and general freestream conditions are difficult to obtain. In order to obtain solutions of realistic structures in realistic freestream conditions, the following parameters should be specified: two thermodynamic properties (such as p_∞ and ρ_∞) and the structural parameters (m, ω_α, ω_h, x_α and r_α). The reduced velocity and frequency and mass ratios become derived quantities. The only free parameter is then Mach number.

Appendix B. A Summary of Computer Runs

The following are the contents of the data compact disc (CD).

1. Directory containing EULER-AE source files and executable. Also contains a make-file for a 64-bit processor. Two grid files are included, one for the NACA 64A006 and one for NACA 64A010 (asymmetric). The input file and the script to submit the job are also included.
2. Directory containing the time histories of the cases run to generate the results in this dissertation.
3. Directory containing restart files for some of the cases that were run.

A brief explanation of how to use the EULER-AE code is presented along with a summary of the computer runs.

The Linux/UNIX version of EULER-AE is designed to be run from the command line with the following statement:

```
./euler_ae <input_file_name> <grid_file_name> <restart_file_name>
```

A sample of the input file is shown in Figure B.1. The Start/Restart information provides names for the output files. The input files `restartfile` and `gridfile` are ignored since these are obtained from the command line. The name of the restart file to be read in subsequent runs is saved as binary in `newrestartfile`. The final flowfield, at the end of steady state convergence or the last time accurate solution, is saved as ASCII and Tecplot™ format in `fflow`. The animation file for Tecplot™ is saved as ASCII in `mflow`. The time history file, `timehist`, is saved in ASCII. The first variable is nondimensional time, the second is pitch, the third is plunge, the fourth is the coefficient of lift, and the last is the moment coefficient. The grid size `imax` and `jmax` must match the grid input file.

The inflow and reference length parameters are entered next. The code expects dimensional SI units for input and will perform the nondimensionalizations. Some of

```
Input paramters for EULER_AE

Start/Restart Information
                           1 ! (restart) 0 = restart, 1 = new case
            restartcase293.dat ! (restartfile) Name of restart file to be read
            restartcase293.dat ! (newrestartfile) Name of new restart file to be written
              fflowcase293.dat ! (fflow) Final flow file
              mflowcase293.dat ! (mflow) Movie flow file (animation)
           timehistcase293.dat ! (timehist) Time history of pitch, plunge, C_l, and C_m
              naca64a006v3.dat ! (gridfile) Name of grid file
                         257 ! (imax)
                          65 ! (jmax)

Inflow and reference length
   37612.0 ! (p_in) Free-stream pressure (N/m^2)
    0.5489 ! (rho_in) Free-stream density (kg/m^3)
1.7887e-5 ! (mu_in) Free-stream viscosity (kg/ms^2)
    287.05 ! (R_gas) Gas constant (N*m/kg*K)
       1.4 ! (gamma) Ratio of specific heats
     0.850 ! (M_in) Free-stream Mach
      6.00 ! (aoa_deg) Angle of attack (degrees)
      0.72 ! (Pr) Prandtl Number
    1.0000 ! (ref_len) Reference length (m)
    288.15 ! (T_w) Wall Temperature (K) (Make this negative for adiabatic wall)

Program Parameters
     25000 ! (mmax) maximum number of time steps (steady-state)
     26000 ! (jump) output interval
    1.0e-5 ! (tol) Convergence tolerance (steady state)
     500.0 ! (tend) Final time (time accurate)
         1 ! (istep) 0 = use computed time step, 1 = user defined time step (time accurate)
   0.00020 ! (user_dt) user defined time step (time accurate)

Solution Parameters
         0 ! (march) 0 = time explicit, 1 = dual time implicit
      1.00 ! (CFL) Stability time step control
         1 ! (method) 0 = JST   1 = Roe
       1.0 ! (psi) 0 = 1st order Roe, 1 = higher order Roe
0.333333333333333 ! (kappa) -1 = O(2) upwind, 0 = O(2) Fromm, 1/3 = O(3) upwind, 1 = O(2) cen. diff.
         1 ! (limiter) 0 = no limiter, 1 = minmod, 2 = superbee
       0.0 ! (ent) 0 = no entropy fix, 1 = Harten and Hyman, 4 = Kermani and Plet

Boundary Conditions
         0 ! (iminbndry) imin boundary condition, 0 = farfield, 1 = wall
         0 ! (imaxbndry) imax boundary condition, 0 = farfield, 1 = wall
         1 ! (jminbndry) jmin boundary condition, 0 = farfield, 1 = wall
         0 ! (jmaxbndry) jmax boundary condition, 0 = farfield, 1 = wall
        65 ! (icut1) Set to 0 unless using a C-grid
       193 ! (icut2) Will be set to imax + 1 if icut1 = 0

Airfoil Parameters
     0.375 ! (x_cg) Distance (% chord) from the airfoil leading edge to the CG
     -0.25 ! (x_alpha) Distance (% semi-chord) from the CG to the elastic axis
      0.25 ! (r_alpha_sq) Radius (% semi-chord) of gyration (squared)
       0.2 ! (omega_bar) Frequency ratio
       0.5 ! (zeta_h)
       0.5 ! (zeta_alpha)
   -25.398 ! (beta_alpha)
     500.0 ! (gamma_alpha)
     125.0 ! (m_bar) mass ratio
      6.50 ! (V_bar) Reduced velocity (nondimensional) (% semi-chord)
      0.00 ! (plunge) Initial plunge (nondimensional) (positive in the up direction)
```

Figure B.1 Typical input file for EULER-AE

these parameters (`mu_in`, `Pr`, `T_w`) are for a viscous code and are ignored in the current version of EULER-AE.

The program parameters control the number of steady state iterations and the maximum time for the time accurate integration. For a steady state solution only, set `mmax` to the desired number of iterations and `tend` to 0. To start a time accurate solution from a converged steady state solution or to restart a time accurate solution, set `restart` to 1, `mmax` to 0 and `tend` to the desired maximum time. Since the restart file saves the time the last integration was performed to, `tend` must be greater that that time in order for the program to continue integrating. The output interval `jump` controls how often each animation file is written to `mflow`.

The solution parameters control the type of time integration to use and the scheme used to compute the flux vectors. The dual time step option (`march` set to 1) is not fully functional and should not be used. The code is capable of computing the flux vectors from the Jameson-Schmidt-Turkel scheme or the Roe scheme. The Roe scheme incorporates the MUSCL scheme to allow for higher order spatial integration. Additionally, two different limiters and entropy correction schemes can be chosen. The parameters shown in Figure B.1 were used throughout this study, i.e. a second order explicit time integration with a third order Roe scheme with the minmod limiter and no entropy correction.

Two different boundary conditions are set explicitly – farfield and wall. The third is selected based upon the value of `icut1`. This is the cut condition. If `icut1` is set to 0, no cut boundaries are assumed (e.g. a supersonic ramp). For the 257×65 point grid used in this study, the values of `icut1` and `icut2` shown in Figure B.1 indicate a cut boundary condition exists from 1 to 65 and 193 to 257.

Finally, the structural parameters of the airfoil are entered. These parameters are x_{cg} (`x_cg`), x_α (`x_alpha`), r_α^2 (`r_alpha_sq`), ω_r (`omega_bar`), ζ_h (`zeta_h`), ζ_α (`zeta_alpha`), β_α (`beta_alpha`), γ_α (`gamma_alpha`), and μ_s (`m_bar`). The reduced velocity V_r (`V_bar`) and the initial nondimensional plunge displacement $y(0)$ (`plunge`) are also entered here. Note the initial rates $\dot{\alpha}(0)$ and $\dot{y}(0)$ are assumed to be zero.

The parameters that changed from run to run were $\alpha(0)$ (`aoa_deg`), β_α (`beta_alpha`), γ_α (`gamma_alpha`), and V_r (`V_bar`). Table B.1 summarizes each of the cases. Cases 1, 2, and 3 are not shown since they were used to perform final verification of the code.

Table B.1 Summary of computer runs

Case	$\alpha(0)$	β_α	γ_α	V_r
4	1.0	-3.0	0.0	6.0
5	2.0	-3.0	0.0	6.0
6	3.0	-3.0	0.0	6.0
7	4.0	-3.0	0.0	6.0
8	5.0	-3.0	0.0	6.0
9	6.0	-3.0	0.0	6.0
10	7.0	-3.0	0.0	6.0
11	1.0	-10.0	0.0	6.6
12	2.0	-10.0	0.0	6.6
13	3.0	-10.0	0.0	6.6
14	4.0	-10.0	0.0	6.6
15	5.0	-10.0	0.0	6.6
16	6.0	-10.0	0.0	6.6
17	7.0	-10.0	0.0	6.6
18	1.0	-40.0	0.0	6.5
19	2.0	-40.0	0.0	6.5
20	3.0	-40.0	0.0	6.5
21	4.0	-40.0	0.0	6.5
22	5.0	-40.0	0.0	6.5
23	6.0	-40.0	0.0	6.5
24	7.0	-40.0	0.0	6.5
25	1.0	-40.0	2000.0	6.5
26	2.0	-40.0	2000.0	6.5
27	3.0	-40.0	2000.0	6.5
28	4.0	-40.0	2000.0	6.5
29	5.0	-40.0	2000.0	6.5
30	6.0	-40.0	2000.0	6.5
31	7.0	-40.0	2000.0	6.5
32	1.0	-40.0	2500.0	6.5
33	2.0	-40.0	2500.0	6.5
34	3.0	-40.0	2500.0	6.5
35	4.0	-40.0	2500.0	6.5
36	5.0	-40.0	2500.0	6.5
37	6.0	-40.0	2500.0	6.5
38	7.0	-40.0	2500.0	6.5
39	1.0	-40.0	2000.0	6.5
40	2.0	-40.0	2000.0	6.5
41	3.0	-40.0	2000.0	6.5
42	4.0	-40.0	2000.0	6.5
43	5.0	-40.0	2000.0	6.5

Table A.1 Summary of computer runs (continued)

Case	$\alpha(0)$	β_α	γ_α	V_r
44	6.0	-40.0	2000.0	6.5
45	7.0	-40.0	2000.0	6.5
46	1.0	-40.0	1500.0	6.5
47	2.0	-40.0	1500.0	6.5
48	3.0	-40.0	1500.0	6.5
49	4.0	-40.0	1500.0	6.5
50	5.0	-40.0	1500.0	6.5
51	6.0	-40.0	1500.0	6.5
52	7.0	-40.0	1500.0	6.5
53	1.0	-40.0	1000.0	6.5
54	2.0	-40.0	1000.0	6.5
55	3.0	-40.0	1000.0	6.5
56	4.0	-40.0	1000.0	6.5
57	5.0	-40.0	1000.0	6.5
58	6.0	-40.0	1000.0	6.5
59	7.0	-40.0	1000.0	6.5
60	1.0	-30.0	500.0	6.5
61	2.0	-30.0	500.0	6.5
62	3.0	-30.0	500.0	6.5
63	4.0	-30.0	500.0	6.5
64	5.0	-30.0	500.0	6.5
65	6.0	-30.0	500.0	6.5
66	7.0	-30.0	500.0	6.5
67	7.0	-30.0	500.0	6.0
68	7.0	-30.0	500.0	6.1
69	7.0	-30.0	500.0	6.2
70	7.0	-30.0	500.0	6.3
71	7.0	-30.0	500.0	6.4
72	7.0	-30.0	500.0	6.6
73	7.0	-30.0	500.0	6.12
74	7.0	-30.0	500.0	6.14
75	7.0	-30.0	500.0	6.16
76	7.0	-30.0	500.0	6.18
77	7.0	-30.0	500.0	6.105
78	7.0	-30.0	500.0	6.11
79	7.0	-30.0	500.0	6.115
80	2.25	-30.0	500.0	6.5
81	2.50	-30.0	500.0	6.5
82	2.75	-30.0	500.0	6.5
83	6.0	-27.0	500.0	6.5

Table A.1 Summary of computer runs (continued)

Case	$\alpha(0)$	β_α	γ_α	V_r
84	6.0	-24.0	500.0	6.5
85	6.0	-21.0	500.0	6.5
86	6.0	-18.0	500.0	6.5
87	6.0	-33.0	500.0	6.5
87b[1]	6.0	-33.0	500.0	6.5
88	6.0	-36.0	500.0	6.5
88b	6.0	-36.0	500.0	6.5
89	6.0	-39.0	500.0	6.5
89b	6.0	-39.0	500.0	6.5
90	6.0	-42.0	500.0	6.5
91	7.0	-30.0	500.0	6.65
92	7.0	-30.0	500.0	6.7
93	7.0	-30.0	500.0	6.75
94	2.8	-30.0	500.0	6.5
95	2.85	-30.0	500.0	6.5
96	2.9	-30.0	500.0	6.5
97	2.95	-30.0	500.0	6.5
98	7.0	30.0	500.0	6.55
99	7.0	30.0	500.0	6.6
100	7.0	30.0	500.0	6.65
101	6.0	-23.5	500.0	6.5
102	6.0	-23.0	500.0	6.5
103	6.0	-22.5	500.0	6.5
104	6.0	-22.0	500.0	6.5
105	6.0	-23.9	500.0	6.5
106	6.0	-23.8	500.0	6.5
107	6.0	-23.7	500.0	6.5
108	6.0	-23.6	500.0	6.5
109	7.0	30.0	500.0	6.8
110	7.0	30.0	500.0	6.9
111	7.0	30.0	500.0	7.0
112	7.0	30.0	500.0	7.1
113	2.86	-30.0	500.0	6.5
114	2.865	-30.0	500.0	6.5
115	2.87	-30.0	500.0	6.5
116	2.875	-30.0	500.0	6.5
116b	2.875	-30.0	500.0	6.5
117	2.88	-30.0	500.0	6.5
117b	2.88	-30.0	500.0	6.5
118	2.885	-30.0	500.0	6.5

[1] "b" indicates a restart file

Table A.1 Summary of computer runs (continued)

Case	$\alpha(0)$	β_α	γ_α	V_r
119	2.89	-30.0	500.0	6.5
120	-2.875	-30.0	500.0	6.5
121	-2.87	-30.0	500.0	6.5
122	0.5	-42.0	500.0	6.5
123	1.0	-42.0	500.0	6.5
124	1.5	-42.0	500.0	6.5
125	2.0	-42.0	500.0	6.5
126	2.5	-42.0	500.0	6.5
127	3.0	-42.0	500.0	6.5
128	3.0	-39.0	500.0	6.5
129	3.0	-36.0	500.0	6.5
130	3.0	-33.0	500.0	6.5
131	3.0	-30.0	500.0	6.5
132	7.0	30.0	500.0	7.1
133	7.0	30.0	500.0	7.2
134	2.95	-42.0	500.0	6.5
135	2.9	-42.0	500.0	6.5
136	2.85	-42.0	500.0	6.5
137	2.8	-42.0	500.0	6.5
138	2.75	-42.0	500.0	6.5
139	2.7	-42.0	500.0	6.5
140	2.69	-42.0	500.0	6.5
141	2.68	-42.0	500.0	6.5
142	2.67	-42.0	500.0	6.5
143	2.66	-42.0	500.0	6.5
144	2.65	-42.0	500.0	6.5
145	2.64	-42.0	500.0	6.5
146	2.63	-42.0	500.0	6.5
147	2.62	-42.0	500.0	6.5
148	2.61	-42.0	500.0	6.5
149	2.60	-42.0	500.0	6.5
150	2.59	-42.0	500.0	6.5
151	7.0	30.0	500.0	7.3
151b	7.0	30.0	500.0	7.3
152	7.0	30.0	500.0	7.4
152b	7.0	30.0	500.0	7.4
153	7.0	30.0	500.0	7.5
153b	7.0	30.0	500.0	7.5
154	7.0	30.0	500.0	7.2
154b	7.0	30.0	500.0	7.2

Table A.1 Summary of computer runs (continued)

Case	$\alpha(0)$	β_α	γ_α	V_r
155	2.585	-42.0	500.0	6.5
156	2.58	-42.0	500.0	6.5
157	2.575	-42.0	500.0	6.5
158	2.57	-42.0	500.0	6.5
159	2.565	-42.0	500.0	6.5
160	2.56	-42.0	500.0	6.5
161	2.555	-42.0	500.0	6.5
162	2.55	-42.0	500.0	6.5
163	2.545	-42.0	500.0	6.5
164	2.54	-42.0	500.0	6.5
165	2.535	-42.0	500.0	6.5
166	2.53	-42.0	500.0	6.5
167	2.525	-42.0	500.0	6.5
168	-2.545	-42.0	500.0	6.5
169	-2.55	-42.0	500.0	6.5
170	2.61	-39.0	500.0	6.5
171	2.62	-39.0	500.0	6.5
172	2.63	-39.0	500.0	6.5
173	2.64	-39.0	500.0	6.5
174	2.65	-39.0	500.0	6.5
175	2.66	-39.0	500.0	6.5
176	2.67	-39.0	500.0	6.5
177	2.68	-39.0	500.0	6.5
178	2.69	-39.0	500.0	6.5
179	2.555	-39.0	500.0	6.5
180	2.56	-39.0	500.0	6.5
181	2.565	-39.0	500.0	6.5
182	2.57	-39.0	500.0	6.5
183	2.575	-39.0	500.0	6.5
184	2.58	-39.0	500.0	6.5
185	2.585	-39.0	500.0	6.5
186	2.59	-39.0	500.0	6.5
187	2.595	-39.0	500.0	6.5
188	2.6	-39.0	500.0	6.5
189	2.605	-39.0	500.0	6.5
190	2.66	-36.0	500.0	6.5
191	2.665	-36.0	500.0	6.5
192	0.5	30.0	500.0	6.8
192b	0.5	30.0	500.0	6.8
193	0.5	30.0	500.0	6.9

Table A.1 Summary of computer runs (continued)

Case	$\alpha(0)$	β_α	γ_α	V_r
194	0.5	30.0	500.0	7.0
195	0.5	30.0	500.0	7.1
196	0.5	30.0	500.0	6.85
197	2.67	-36.0	500.0	6.5
198	2.675	-36.0	500.0	6.5
199	0.1	30.0	500.0	6.75
200	2.76	-33.0	500.0	6.5
201	2.765	-33.0	500.0	6.5
202	2.77	-33.0	500.0	6.5
203	2.775	-33.0	500.0	6.5
204	2.9	-27.0	500.0	6.5
205	2.925	-27.0	500.0	6.5
206	2.95	-27.0	500.0	6.5
207	2.975	-27.0	500.0	6.5
208	3.0	-27.0	500.0	6.5
209	2.755	-33.0	500.0	6.5
210	2.75	-33.0	500.0	6.5
211	2.745	-33.0	500.0	6.5
212	2.74	-33.0	500.0	6.5
213	2.735	-33.0	500.0	6.5
214	2.73	-33.0	500.0	6.5
215	3.05	-27.0	500.0	6.5
216	3.10	-27.0	500.0	6.5
217	3.15	-27.0	500.0	6.5
218	3.20	-27.0	500.0	6.5
219	3.25	-27.0	500.0	6.5
220	3.30	-27.0	500.0	6.5
221	3.35	-27.0	500.0	6.5
222	0.1	30.0	500.0	6.7
223	0.1	30.0	500.0	6.8
224	0.1	30.0	500.0	6.9
225	0.1	30.0	500.0	7.0
226	3.055	-27.0	500.0	6.5
227	3.06	-27.0	500.0	6.5
228	3.065	-27.0	500.0	6.5
229	3.070	-27.0	500.0	6.5
230	3.075	-27.0	500.0	6.5
231	3.080	-27.0	500.0	6.5
232	3.1	-23.9	500.0	6.5
233	3.125	-23.9	500.0	6.5

Table A.1 Summary of computer runs (continued)

Case	$\alpha(0)$	β_α	γ_α	V_r
234	3.15	-23.9	500.0	6.5
235	3.175	-23.9	500.0	6.5
236	3.2	-23.9	500.0	6.5
237	3.225	-23.9	500.0	6.5
238	3.25	-23.9	500.0	6.5
239	0.1	30.0	500.0	6.6
240	3.225	-23.9	500.0	6.5
241	3.26	-23.9	500.0	6.5
242	3.265	-23.9	500.0	6.5
243	3.27	-23.9	500.0	6.5
244	3.275	-23.9	500.0	6.5
245	3.28	-23.9	500.0	6.5
246	3.285	-23.9	500.0	6.5
247	3.29	-23.9	500.0	6.5
248	3.295	-23.9	500.0	6.5
249	3.3	-23.9	500.0	6.5
250	3.5	-23.9	500.0	6.5
251	3.75	-23.9	500.0	6.5
252	4.0	-23.9	500.0	6.5
253	4.25	-23.9	500.0	6.5
254	4.5	-23.9	500.0	6.5
255	4.75	-23.9	500.0	6.5
256	5.0	-23.9	500.0	6.5
257	5.25	-23.9	500.0	6.5
258	4.775	-23.9	500.0	6.5
259	4.8	-23.9	500.0	6.5
260	4.825	-23.9	500.0	6.5
261	4.85	-23.9	500.0	6.5
262	4.875	-23.9	500.0	6.5
263	4.9	-23.9	500.0	6.5
264	4.925	-23.9	500.0	6.5
265	4.95	-23.9	500.0	6.5
266	4.975	-23.9	500.0	6.5
267	0.1	0.0	0.0	7.0
268	-2.15	-30.38	500.0	6.5
269	4.88	-23.9	500.0	6.5
270	4.885	-23.9	500.0	6.5
271	4.89	-23.9	500.0	6.5
272	4.895	-23.9	500.0	6.5
273	4.125	-23.9	500.0	6.5

Table A.1 Summary of computer runs (finished)

Case	$\alpha(0)$	β_α	γ_α	V_r
274	-2.775	-31.44	500.0	6.5
275	-1.764	-32.96	500.0	6.5
276	1.748	-29.26	500.0	6.5
277	0.6263	-24.0	500.0	6.5
278	-0.825	-33.02	500.0	6.5
279	6.0	-37.5	500.0	6.5
280	6.0	-34.602	500.0	6.5
281	6.0	-33.451	500.0	6.5
282	6.0	-32.661	500.0	6.5
283	6.0	-32.023	500.0	6.5
284	6.0	-31.466	500.0	6.5
285	6.0	-30.956	500.0	6.5
286	6.0	-30.472	500.0	6.5
287	6.0	-29.528	500.0	6.5
288	6.0	-29.044	500.0	6.5
289	6.0	-28.534	500.0	6.5
290	6.0	-27.977	500.0	6.5
291	6.0	-27.339	500.0	6.5
292	6.0	-26.549	500.0	6.5
293	6.0	-25.398	500.0	6.5
294	1.7255	-26.549	500.0	6.5
295	2.30118	-26.549	500.0	6.5
296	3.75	-26.549	500.0	6.5
297	1.7255	-25.398	500.0	6.5
298	2.30118	-25.398	500.0	6.5
299	3.75	-25.398	500.0	6.5

Vita

Major Daniel R. Millman graduated from Thomas Jefferson High School in San Antonio, Texas in May 1982. He attended undergraduate studies at Rice University in Houston, Texas and received a Bachelor of Science in Mechanical Engineering in 1986. He then attended the Joint Institute for Advancement of Flight Sciences at the National Aeronautics and Space Administration's Langley Research Center in Hampton, Virginia. He worked as a graduate research scholar assistant in the Aerothermodynamics Branch of the Space Systems Division while earning a Master of Science in Astronautical Engineering from the George Washington University. Upon his graduation in 1989, he returned to San Antonio where he attended the Air Force Officer Training School.

Upon receiving his commission in 1990, he attended Undergraduate Pilot Training at Laughlin AFB, Texas. He graduated in 1991 and was assigned to Minot AFB, North Dakota as a B-52 and T-38 pilot. After aircraft commander upgrade training in 1996, he was assigned to Barksdale AFB, Louisiana where he served as a B-52 aircraft commander and instructor pilot. He was accepted to the Air Force Test Pilot School (TPS) at Edwards AFB, California in 1997 and graduated from TPS in 1998. He then served as a B-52 and B-1 test pilot, Chief of Standardization and Evaluation, and the B-52 Flight Commander for the 419th Flight Test Squadron at Edwards AFB. He tested the newest weapons for B-52 and B-1 aircraft, including the Joint Direct Attack Munition, the Wind Corrected Munitions Dispenser, the Joint Stand-Off Weapon, and the Joint Air to Surface Stand-off Missile. Thus far, in his flying career, he has accumulated over 2700 hours in 31 different aircraft.

In 2001 he was assigned to the Air Force Institute of Technology at Wright-Patterson AFB, Ohio. Upon graduation he will be assigned to TPS as an instructor.

REPORT DOCUMENTATION PAGE

Form Approved
OMB No. 0704-0188

PLEASE DO NOT RETURN YOUR FORM TO THE ABOVE ORGANIZATION.

1. REPORT DATE *(DD-MM-YYYY)*	2. REPORT TYPE	3. DATES COVERED *(From - To)*
27-08-2004	Dissertation	July 2003 - August 2004

4. TITLE AND SUBTITLE
QUANTIFYING INITIAL CONDITION AND PARAMETRIC UNCERTAINTIES IN A NONLINEAR AEROELASTIC SYSTEM WITH AN EFFICIENT STOCHASTIC ALGORITHM

5a. CONTRACT NUMBER

5b. GRANT NUMBER

5c. PROGRAM ELEMENT NUMBER

6. AUTHOR(S)
Millman, Daniel R., Major, USAF

5d. PROJECT NUMBER

5e. TASK NUMBER

5f. WORK UNIT NUMBER

7. PERFORMING ORGANIZATION NAME(S) AND ADDRESS(ES)
Air Force Institute of Technology
Graduate School of Engineering and Management (AFIT/EN)
2950 Hobson Way, Building 641
WPAFB, OH 45433-7765

8. PERFORMING ORGANIZATION REPORT NUMBER
AFIT/DS/ENY/04-03

9. SPONSORING/MONITORING AGENCY NAME(S) AND ADDRESS(ES)
AFRL/VASD
ATTN: Philip S. Beran
Building 146, 2210 Eigth Street
WPAFB, OH 45433-7531
DSN: 785-2521
email: Philip.Beran@wpafb.af.mil

10. SPONSOR/MONITOR'S ACRONYM(S)

11. SPONSOR/MONITOR'S REPORT NUMBER(S)

12. DISTRIBUTION/AVAILABILITY STATEMENT
APPROVED FOR PUBLIC RELEASE, DISTRIBUTION UNLIMITED

13. SUPPLEMENTARY NOTES

14. ABSTRACT

There is a growing interest in understanding how uncertainties in flight conditions and structural parameters affect the character of a limit cylce oscillation (LCO) response, leading to failure of an aeroelastic system. Uncertainty quantification of a stochastic system (parametric uncertainty) with stochastic inputs (initial condition uncertainty) has traditionally been analyzed with Monte Carlo simulations (MCS). Probability density functions (PDF) of the LCO response are obtained from the MCS to estimate the probability of failure. A candidate approach to efficiently estimate the PDF of an LCO response is the stochastic projection method.The objective of this research is to extend the stochastic projection method to include the construction of B-spline surfaces in the stochastic domain. The multivariate B-spline problem is solved to estimate the LCO response surface. An MCS is performed on this response surface to estimate the PDF of the LCO response. The probability of failure is then computed from the PDF. This method is applied to the problem of estimating the PDF of a subcritical LCO response of a nonlinear airfoil in inviscid transonic flow. The stochastic algorithm provides a conservative estimate of the probability of failure of this aeroelastic system two orders of magnitude more efficiently than performing an MCS on the governing equations.

15. SUBJECT TERMS
Stochastic projection method, limit cycle oscillation, Monte Carlo simulation, aeroelastic system, probability density function, probability of failure

16. SECURITY CLASSIFICATION OF:			17. LIMITATION OF ABSTRACT	18. NUMBER OF PAGES	19a. NAME OF RESPONSIBLE PERSON
a. REPORT	b. ABSTRACT	c. THIS PAGE			King, Paul I., CIV (ENY)
U	U	U	UU	114	19b. TELEPHONE NUMBER *(Include area code)* (937)255-3636 ext 4628, email Paul.King@afit.edu